

**NASA TECHNICAL NOTE**



**NASA TN D-8503**

**NASA TN D-8503**

**INVESTIGATION OF EFFECT OF PROPULSION  
SYSTEM INSTALLATION AND OPERATION  
ON AERODYNAMICS OF AN AIRBREATHING  
HYPERSONIC AIRPLANE AT MACH 0.3 TO 1.2**

*James M. Cubbage and Charles E. Mercer*

*Langley Research Center*

*Hampton, Va. 23665*

**NATIONAL AERONAUTICS AND SPACE ADMINISTRATION • WASHINGTON, D. C. • JULY 1977**

1. Report No. NASA TN D-8503		2. Government Accession No.		3. Recipient's Catalog No.	
4. Title and Subtitle INVESTIGATION OF EFFECT OF PROPULSION SYSTEM INSTALLATION AND OPERATION ON AERODYNAMICS OF AN AIRBREATHING HYPERSONIC AIRPLANE AT MACH 0.3 TO 1.2				5. Report Date July 1977	
				6. Performing Organization Code	
7. Author(s)  James M. Cabbage and Charles E. Mercer				8. Performing Organization Report No. L-11468	
9. Performing Organization Name and Address  NASA Langley Research Center Hampton, Va. 23665				10. Work Unit No. 505-11-31-02	
				11. Contract or Grant No.	
12. Sponsoring Agency Name and Address  National Aeronautics and Space Administration Washington, D.C. 20546				13. Type of Report and Period Covered Technical Note	
				14. Sponsoring Agency Code	
15. Supplementary Notes					
16. Abstract  Results from an investigation of the effects of the operation of a combined turbojet/scramjet propulsion system on the longitudinal aerodynamic characteristics of a 1/60-scale hypersonic airbreathing launch vehicle configuration are presented. Tests were conducted in the Langley 16-foot transonic tunnel at Mach numbers of 0.3 to 1.2 and a corresponding Reynolds number range of $9 \times 10^6$ to $18 \times 10^6$ . Decomposition products of hydrogen peroxide were used for simulation of the propulsion system exhaust.					
17. Key Words (Suggested by Author(s))  Launch vehicle Jet effects Propulsion integration			18. Distribution Statement  Unclassified - Unlimited   Subject Category 02		
19. Security Classif. (of this report) Unclassified	20. Security Classif. (of this page) Unclassified	21. No. of Pages 92	22. Price* \$5.00		



# INVESTIGATION OF EFFECT OF PROPULSION SYSTEM INSTALLATION

## AND OPERATION ON AERODYNAMICS OF AN AIRBREATHING

### HYPERSONIC AIRPLANE AT MACH 0.3 TO 1.2

James M. Cabbage and Charles E. Mercer  
Langley Research Center

#### SUMMARY

An experimental investigation of the effects of the operation of a combined turbojet/scramjet propulsion installation on the longitudinal aerodynamic characteristics of a hypersonic airbreathing launch vehicle (ABLV) configuration was conducted in the Langley 16-foot transonic tunnel at Mach numbers of 0.3 to 1.2. The corresponding Reynolds number range on the 1.443 meter long, 1/60-scale model was  $9 \times 10^6$  to  $18 \times 10^6$ . The angle-of-attack range was from  $0^\circ$  to  $6^\circ$ . Turbojet exhaust flow was simulated by the decomposition products of hydrogen peroxide ( $H_2O_2$ ) and the scramjet exhaust flow was simulated by a flowthrough nacelle (nonburning) and by a  $H_2O_2$  nacelle for the burning case.

Turbojet operation in conjunction with the simulated nonburning or burning scramjet flow had an adverse effect on longitudinal aerodynamic characteristics. Addition of flow fences for the scramjet exhaust also had an adverse effect on aerodynamic performance. A large transonic drag rise combined with the adverse turbojet effects reduced the subsonic lift-drag ratio by about 50 percent at Mach 1.0 and 1.2 at an angle of attack of  $2^\circ$ . Longitudinal aerodynamic characteristics were relatively insensitive to the angle between the downstream surface of the cutouts provided in the lower afterbody for the turbojet exhaust and the lower afterbody surface.

#### INTRODUCTION

A number of studies have shown that airbreathing hypersonic airplanes using hydrogen as a fuel have unique and desirable characteristics as future flight systems. (See refs. 1 to 3, for example.) Basic to these studies has been the theoretical performance of the supersonic combustion ramjet, or "scramjet," engine. The scramjet is the only promising airbreathing engine for hypersonic flight above about Mach 8 because of severe aerothermodynamic problems with the subsonic combustion ramjet at these speeds. However, the scramjet, like the ramjet, cannot produce static thrust, and at subsonic and low supersonic speeds its operation is very inefficient relative to the turbojet. Therefore, an operational hypersonic airplane will need a composite propulsion system or at least two different propulsion systems - one for each end of the speed range with some overlap between. Regardless of the propulsion system used, integration of the system with the airframe to achieve optimum performance over the desired speed range is a difficult task. Those design features needed for maximum efficiency at hypersonic speeds (scramjet location,

fuel volume, body shape, etc.) all tend to drive the configuration toward one which may have poor aerodynamic performance in the Mach 0.6 to 1.3 speed range. Yet, it is in this speed range where aerodynamic parameters have a major impact on the overall size and weight of the airplane. That is, the thrust margin required to accelerate at a satisfactory rate to scramjet take-over speed will determine the size of the low-speed propulsion system and therefore, to a large degree, airplane weight and size.

Poor aerodynamic characteristics at transonic speeds may be further degraded by a forward location of the low-speed propulsion system (necessary for efficient expansion of the scramjet flow) which allows the exhaust from the low-speed propulsion system to combine with the scramjet nozzle to wash a large area of the airplane rear undersurface. Because of the trade-offs required to obtain good efficiency overall and the influence of transonic performance on airplane size and weight, the primary objective of this study was to provide data on propulsion system installation and engine exhaust flow effects on the transonic aerodynamic characteristics of a hypersonic airplane. Such data were not available and are required in preliminary design efforts for a hypersonic airplane.

The configuration selected for this investigation as being representative of airbreathing hypersonic airplanes was developed during a study of a reusable launch vehicle (ref. 4). In this study, a horizontal take-off and landing, air-breathing, hypersonic airplane was designed to carry a rocket-propelled second stage to a launch velocity of Mach 10 over any desired point on the Earth within range of the airplane. After launch of the reusable second stage (which would then accelerate to orbital velocity), the launch vehicle would decelerate and return to base at a subsonic cruising speed. The propulsion system for this concept consisted of six turbojet engines for take-off and acceleration to about Mach 3.5 (where the turbojets are shut down) and six scramjets to continue acceleration to Mach 10. The turbojets and scramjets share a common, variable-geometry inlet with some inlet flow directed through the scramjets while the turbojets are operating. Burning commences in the scramjet (subsonic combustion mode) at about Mach 1. The model tested in this study was 1/60 the size of the configuration of reference 4 and differed from that concept only in the elimination of the cavity for the semiburied second stage.

Tests were conducted in the Langley 16-foot transonic tunnel at Mach numbers of 0.3 to 1.2 and a corresponding Reynolds number range of  $9 \times 10^6$  to  $18 \times 10^6$  based on a model length of 1.443 meters. Three-component aerodynamic force data were obtained for a range of turbojet and scramjet pressure ratios over a small angle-of-attack range. Decomposition products of hydrogen peroxide were used to simulate both turbojet and scramjet exhaust flows, but for most tests a flowthrough inlet was used for simulation of the flow through the scramjets. Model geometry changes other than the flowthrough inlet included removal of the scramjet flow fences (designed to restrict lateral expansion of the scramjet exhaust at hypersonic flight speeds), and variation of the angle between the downstream surface of the cutouts provided in the lower afterbody for the turbojet exhaust and the lower afterbody surface.

# SYMBOLS

All data presented were measured and reduced in U.S. Customary Units and then converted to SI Units for publication.

$A_{ref}$	model reference area, planform area including horizontal tails, 0.3676 m <sup>2</sup>
$A_x$	model cross-sectional area at distance $x$ , m <sup>2</sup>
$C_A$	axial-force coefficient, $\frac{F_A}{q_\infty A_{ref}}$
$C_D$	drag coefficient, $C_A \cos \alpha + C_N \sin \alpha$
$C_L$	lift coefficient, $C_N \cos \alpha - C_A \sin \alpha$
$C_m$	pitching-moment coefficient, $\frac{M_Y}{q_\infty A_{ref} l_{ref}}$
$C_N$	normal-force coefficient, $\frac{F_N}{q_\infty A_{ref}}$
$C_p$	pressure coefficient, $\frac{p_{ramp} - p_\infty}{q_\infty}$
$F_A$	axial force along X-axis, positive direction $-x$ , N
$F_N$	normal force along Z-axis, positive direction $-z$ , N
$L/D$	lift-drag ratio, $C_L/C_D$
$l_{ref}$	model reference length (length of sharp-nosed body), 1.443 m
$M_Y$	moment about Y-axis, positive nose up, kg-m
$M_\infty$	free-stream Mach number
$p_{ramp}$	static pressure on afterbody ramp, Pa
$p_t$	total pressure, Pa
$p_\infty$	free-stream static pressure, Pa
$q_\infty$	free-stream dynamic pressure, Pa
$x$	distance along model reference line from beginning of sharp-nosed body, m

$y, z$	horizontal and vertical distances from reference line, m
$\Delta C_D$	drag coefficient with turbojet flow minus drag coefficient without turbojet flow
$\Delta C_L$	lift coefficient with turbojet flow minus lift coefficient without turbojet flow
$\Delta C_m$	pitching-moment coefficient with turbojet flow minus pitching-moment coefficient without turbojet flow
$\alpha$	angle of attack, deg
$\epsilon$	ramp angle (see fig. 5), deg

Subscripts:

B	body alone
BN	body with flowthrough nacelle
BT	body with tails
FF	flow fences
NF	no flow fence
SJ	scramjet or resulting from thrust of scramjets
TJ	turbojet or resulting from thrust of turbojets

Abbreviations:

SJ	scramjet
TJ	turbojet

A bar over a symbol indicates an arithmetic average.

## WIND TUNNEL AND MODEL

### Wind Tunnel

This investigation was conducted in the Langley 16-foot transonic tunnel, which is a single-return, continuous-flow tunnel with an octagonal slotted test section measuring 4.73 meters across the flats. The tunnel stagnation pressure is approximately equal to atmospheric pressure and the maximum tunnel Mach number is 1.3. Reference 5 contains tunnel calibration data and a detailed description of the tunnel and its operation.

## Model

Photographs of the 1/60-scale airbreathing launch vehicle (ABLV) model are presented in figure 1. The photograph in figure 1(a) is a bottom view of the model that shows some details of the propulsion system installation and the scramjet flow fences. Turbojet exhaust flow was simulated entirely by the decomposition products of hydrogen peroxide ( $H_2O_2$ ). Scramjet exhaust flow was simulated by tunnel flow passing through a flowthrough nacelle for the non-burning case and by decomposition products of  $H_2O_2$  ( $H_2O_2$  nacelle) for the burning case. Figures 1(b) and 1(c) show the model as it was installed in the tunnel on the sting-strut assembly. The  $H_2O_2$  nacelle is installed on the model in figure 1(b) whereas the flowthrough nacelle is installed on the model in figure 1(c). A three-view drawing of the model with pertinent dimensions is presented in figure 2 and table I lists other dimensional data for the model. A simplified sectional view of the model illustrating balance and engine arrangement and installation is presented as figure 3. The model was constructed entirely of 300 series stainless steel except for the aluminum alloy nose section. Cross-sectional area distributions of the model are presented in figure 4.

The turbojet and scramjet decomposition chambers (six each) were designed according to information from references 6 and 7. Good performance was obtained from all decomposition chambers throughout the test program. The use of  $H_2O_2$  was dictated by mass flow requirements and model volume restraints rather than by the desire to simulate exhaust flow properties as closely as possible.

Two six-component force balances were initially installed to measure forces acting on the model. (See fig. 3.) The entire model was cantilevered from the support strut by the main balance. The rear balance supported the afterbody or that part of the model (including tail surfaces) downstream of station 103.15. A malfunction of the main balance at the beginning of the tests necessitated the use of a three-component substitute balance of less pitching-moment capacity. This substitution restricted the angle-of-attack range for all configurations and the Mach number range for some configurations. A second problem concerned the rear or afterbody balance. Unexpected leakage of the hot turbojet exhaust gases past the seal between the forebody and afterbody imposed a 755 K environment on the rear balance and large zero shifts invalidated the data from this balance. A dummy balance was used in place of the live balance for the tests reported herein. Further discussion of the seal leakage problem can be found in appendix A.

Configuration changes made to the model during the test program are shown in figure 5. The removable section of the afterbody, or ramp, contained cut-outs for the turbojet nozzles and for the exhaust flow from these nozzles. The ramp without cutouts was used in conjunction with the cover plate for tests of the model without the propulsion system. The flowthrough nacelle had the same external geometry as the faired-closed  $H_2O_2$  nacelle containing the scramjet  $H_2O_2$  decomposition chambers. The flow fences extended the full length of the ramps and had a thickness of 0.16 cm. The fences were welded to the ramps because of strength requirements so that configurations with the flow fences were tested first and the fences were then removed by machining. A 1-cm-wide boundary-layer trip of silicon carbide particles was located about 2.5 cm behind

the nose tip of the model. Further details of the model, test procedures, instrumentation, etc., are discussed in appendix A.

## RESULTS AND DISCUSSION

The aerodynamic coefficients obtained from this investigation reflect an unknown level of interference from the strut supporting the model. This interference is not believed to be a significant factor for incremental values between configurations. Data were not recorded between  $M_\infty = 1.0$  and  $M_\infty = 1.2$  because of possible shock reflections from the tunnel walls striking the model and because of the presence of the strut. Consequently, curve fairings between  $M_\infty = 1.0$  and  $M_\infty = 1.2$  have been omitted on all figures although the fairing in some cases appears obvious. The primary objective of this study was to obtain data on propulsion system installation and engine-exhaust flow effects on the transonic aerodynamic characteristics of a hypersonic airplane.

### Model Without Turbojet Engines

Drag, lift, and pitching-moment coefficients obtained for the several configurations without turbojet exhaust simulation are shown in figure 6 as a function of Mach number for several angles of attack. The pitching-moment capacity of the balance limited the angle-of-attack range for those configurations with tails to a maximum of  $4^\circ$ . Included in the figures are data at  $M_\infty = 0.3$  and  $\alpha = 0^\circ$  which were operational checkpoints for the model. Of particular note for all configurations is the substantial drag rise beginning at about  $M_\infty = 0.8$  which is attributed to a large extent to the poor cross-sectional area distribution of the configurations. Prior to the tunnel tests, an exploratory effort to calculate the drag rise was made by using a computer program for axisymmetric bodies called RAXBOD (refs. 8 and 9). Prediction of experimental results was partially successful even though the ABLV model was not within the scope of configurations for which the program was intended. Further details of this effort are contained in appendix B.

Effect of tails on aerodynamic coefficients.— Incremental lift, drag, and pitching-moment coefficients resulting from addition of the tails with and without the nacelle present (fig. 7) follow trends that would be generally expected, increases in drag and lift and a nose-down increment in pitching-moment coefficient. The horizontal tails provide about as much lift as the body alone whereas the drag increment for the tails is about 50 percent or less of the body alone drag at speeds below  $M_\infty = 0.8$ . The large change in pitching-moment increment between  $M_\infty = 0.9$  and  $M_\infty = 1.2$  results from the increasing negative pitching-moment coefficient for the body alone and the increasing positive pitching-moment coefficient for the body with tails in this speed range. (See figs. 6(a) and 6(b).) Except at  $\alpha = 4^\circ$ , the presence of the flowthrough nacelle had a relatively small effect on incremental forces and moments due to the tails.

Effect of flowthrough nacelle on aerodynamic coefficients.— The effect of the flowthrough nacelle on model drag is substantial as seen in figure 8(a). The increment in drag from the nacelle is about equal to the body alone drag between  $M_\infty = 0.8$  and  $M_\infty = 0.9$ , and the increment increases a small amount

with angle of attack. This drag increase is composed of friction losses of the nacelle, drag of the sharp leading edges of the nacelle, and a decrease in pressures acting on the lower afterbody. The latter is evidenced by a relatively large positive increment in pitching-moment coefficient and an almost insignificant change in lift coefficient. Apparently, lift generated by the nacelle is nearly canceled by the loss in lift on the afterbody but the large moment arm of the afterbody forces generates moments that overshadow those generated by nacelle forces. Between  $M_\infty = 0.9$  and  $M_\infty = 1.0$ , the pitching moment becomes negative and then reverts to a positive value at  $M_\infty = 1.2$ . This trend is exhibited to some degree by the moment coefficient for the body alone (fig. 6(a)).

Effect of flow fences on aerodynamic coefficients.- Because the scramjet exhaust flow at hypersonic speeds will be underexpanded at the end of the cowl or nacelle, flow fences have been proposed to restrict lateral expansion of the exhaust flow and thereby produce a possible thrust increase and a reduction in the strength of shocks generated by interference between the external flow and the exhaust flow. Disadvantages of using flow fences are the increase in surface area washed by the hot exhaust flow and the structure required to handle the forces to which they are subjected. The effect of flow fences on aerodynamic performance in the low-speed range is of importance since it will influence the decision for or against the use of fences for the high-speed range.

As shown in figure 9, the increments in drag, lift, and pitching-moment coefficients resulting from the flow fences are small and oscillate between positive and negative values depending on  $\alpha$  and  $M_\infty$ . Since these increments are within the repeatability of the data, it is concluded that the effect of flow fences on forces and moments without turbojet flow was negligible over the Mach number and angle-of-attack range of these tests. As will be shown later, this was not the situation with turbojet flow.

Untrimmed lift-drag ratio.- Lift-drag ratios calculated from the data of figure 6 are presented in figure 10. The effect of the nacelle and the effect of the transonic drag rise on aerodynamic efficiency are readily apparent in this figure. The  $L/D$  at high subsonic speeds<sup>1</sup> for the body with tails is reduced by about 50 percent by addition of the nacelle. The  $L/D$  of the complete configuration (body, tails, and nacelle) is further reduced by about 50 percent or more by the drag rise at transonic speeds. For the body with tails only, the  $L/D$  reduction is approximately 70 percent at transonic speeds. As mentioned previously, the high drag evidenced around  $M_\infty = 1.0$  can be attributed to the cross-sectional area distribution of the airplane configuration. To improve performance and reduce turbojet engine size required to overcome transonic drag, it is apparent that the design of this airplane would have to be altered to reduce the slopes of the area distribution curve and to alter the sharp break at the maximum area point. Changes in this direction would have to be weighed against possible negative effects at hypersonic speeds and it is

---

<sup>1</sup>Unpublished data obtained by John P. Decker in the Langley low turbulence pressure tunnel at  $M_\infty = 0.25$  and a Reynolds number of  $9.9 \times 10^6$  on a model similar to the ABLV model without flowthrough nacelle showed an  $L/D$  of 6 at  $\alpha = 4^\circ$  and a maximum  $L/D$  of 6.5 at  $\alpha = 5^\circ$ .

possible that some compromise in drag at transonic speeds would have to be accepted and the turbojets sized accordingly.

#### Model With Turbojet Flow and Flowthrough Nacelle

This section of the report discusses data obtained for the several configurations with the turbojets operating in conjunction with the flowthrough nacelle. The data are in the form of incremental drag, lift, and pitching-moment coefficients resulting from turbojet operation and total drag, lift, and pitching-moment coefficients for an angle of attack of  $2^\circ$  and an assumed turbojet pressure ratio schedule. The coefficients with turbojet flow were derived from the basic axial- and normal-force and pitching-moment data presented and discussed in appendix C. These basic data were corrected for components of the turbojet thrust (defined as acting along the nozzle center line at the nozzle exit plane) before conversion to drag, lift, and pitching-moment coefficients. Therefore, these coefficients do not include the drag, lift, and pitching moment contributed by the thrust from the turbojet nozzles, but do include the drag, lift, and pitching-moment effects resulting from the exhaust flow from these nozzles. The drag, lift, and pitching-moment coefficients thus obtained were then referenced to the appropriate no-turbojet-flow data from figure 6 to obtain increments resulting from turbojet operation.

Effect of ramp angle  $\epsilon$ .— Figure 11 shows increments in drag, lift, and pitching moment resulting from turbojet operation with ramp angles of  $5^\circ$ ,  $10^\circ$ , and  $20^\circ$  for configurations with flowthrough nacelle and flow fences. The increment in  $C_D$ ,  $C_L$ , and  $C_m$  for each ramp angle was obtained by subtracting the coefficient values for no-turbojet operation (fig. 6(e)) from the corresponding coefficient values obtained with turbojet operation. Therefore, the individual curves for the three ramp angles reflect the effect of turbojet operation on drag, lift, and pitching moment and the differences between the curves show the effect of ramp angle. In general, the difference noted between increments is relatively small and one ramp angle is not clearly superior to the other angles. In figure 12, where total coefficients are presented for the three configurations as a function of Mach number for  $\alpha = 2^\circ$  and an assumed jet pressure ratio schedule (fig. 13), the  $10^\circ$  configuration is seen to have more lift than the  $5^\circ$  and  $20^\circ$  configurations. The drag of the  $10^\circ$  configuration is slightly less at  $M_\infty = 0.6$  and a little greater at  $M_\infty = 0.85$  than that for the  $5^\circ$  and  $20^\circ$  configurations so that the performance of the  $10^\circ$  model although superior at  $M_\infty = 0.6$  is approximately the same as that of the other configurations at  $M_\infty = 0.85$ . The lack of data above  $M_\infty = 0.85$  for the  $\epsilon = 5^\circ$  and  $20^\circ$  configurations and the lack of data at higher values of  $\alpha$  for all configurations are a handicap in firmly establishing the effect of  $\epsilon$ , but from the data in hand it appears that  $\epsilon$  is not a dominant factor and can be altered to suit other design criteria without impacting transonic aerodynamic characteristics significantly. One such criteria may be that the turbojet exhaust openings in the rear undersurface, such as those in this design, must be closed off when the airplane is flying on scramjet propulsion only. At hypersonic speeds, the net propulsive thrust is generated primarily by the external portion of the scramjet nozzle (the rear undersurface), and any losses from shocks and expansion waves generated by open cavities for the turbojet exhaust may cause thrust losses and hot spots from interference heating.



The data presented in figures 11 and 12 are for configurations having flow fences installed and the question arises as to the influence of flow fences on the effect of  $\epsilon$ . Study of pressure data from the eight taps located on the ramp leads to the belief that the effect of  $\epsilon$  without fences would be essentially the same as that obtained with fences although the level of the coefficients may differ from those obtained with fences. (See appendix C.)

Effect of flow fences.— Data presented earlier (fig. 9) showed that the effect of flow fences on aerodynamic performance without turbojet flow was negligible. As seen in figure 14, this is not the case with the turbojets operating. (The incremental coefficients in this figure were obtained in the same manner as those in fig. 11, the turbojets-on data for the configuration without fences being referenced to the no-turbojet flow data of fig. 6(d).) The major influence of flow fences on performance with turbojet flow is a loss of lift and, of course, a corresponding change in pitching moment. Airplane drag is generally increased a small amount relative to the loss in lift. At  $\alpha = 4^\circ$  and  $M_\infty = 0.6$ , there is no increase in drag from the fences but a substantial loss in lift. These results are believed to occur primarily because of the pressure difference between the outside and inside of the fences. The expanding turbojet flow lowers pressures on the inside of the fences relative to the pressure external to the fences as the exhaust flows down the afterbody, and this effect in combination with the canted installation of the fences results in a significant negative normal force. This loss in lift does not show up as a drag increase primarily because the axial projected area of the fences is very small.

In figure 15, total coefficients are shown for  $\alpha = 2^\circ$  and the assumed jet pressure ratio schedule (fig. 13) over the Mach range tested for the  $\epsilon = 20^\circ$  configuration with and without flow fences. In this figure the subsonic drag coefficient is increased by the fences and the overall results here and in figure 14 indicate that flow fences are a detriment to airplane performance in the speed range of these tests. These results combined with other negative factors mentioned previously for flow fences will require that fences exert a strong positive influence on scramjet thrust at hypersonic speeds to justify their use if the airplane geometry requires that the fences slant outward from a vertical position.

Drag, lift, and pitching-moment coefficients with and without turbojet flow.— Force and moment data corrected for the turbojet thrust have been used to calculate aerodynamic coefficients for two configurations ( $\epsilon = 10^\circ$  with flow fences and  $\epsilon = 20^\circ$  without flow fences) over the Mach number range of these tests for  $\alpha = 2^\circ$  and the assumed jet pressure ratio schedule of figure 13. These coefficients are compared with those obtained without turbojet operation (figs. 6(d) and 6(e)) in figure 16. If the small difference noted previously between the  $\epsilon = 10^\circ$  and  $\epsilon = 20^\circ$  configurations is ignored, then this figure also illustrates the effect of flow fences over the full Mach range of these tests. Of the three coefficients in figure 16 (and in figs. 12 and 15), the drag coefficient is the one that would be affected the most by inaccuracies inherent in the corrections for the turbojet thrust (by using the difference between two numbers of about the same value, by using an assumed thrust direction, etc.). A more negative value of  $C_{A,TJ}$  than that calculated would increase  $C_D$  and  $C_L$  with turbojet operation and make  $C_m$  more negative.

However, the differences found between configurations having turbojet flow are not affected by the thrust corrections since the corrections are the same for all configurations at the same test conditions.

Lift-drag ratio.-- Since the angle-of-attack range for these tests was limited to a small value because of balance capacity, the L/D ratios calculated from the data are not indicative of those possible with this type of configuration. However, three configurations were selected to illustrate the variation of L/D at  $\alpha = 2^\circ$  as a function of Mach number and to illustrate the effect of flow fences on L/D (fig. 17). To show the effect of flow fences on L/D over the full Mach number range, it was necessary to use data for two configurations having different ramp angles. The L/D curve for the no-turbojet engine configuration applies for the case with or without flow fences since the difference between the two is very small (fig. 9). For the flow-through inlet configuration, turbojet operation reduced untrimmed lift-drag ratios an average of about 6 percent over the Mach number range. Flow fences produced a further reduction in L/D of about 18 percent at Mach 0.6 and about 7 percent at Mach 1.0. The large decrease in going from subsonic to transonic speeds definitely indicates the need for design changes to improve the aerodynamic efficiency of configurations of the type tested, and emphasizes the point that transonic drag will determine turbojet size which in turn affects the overall airplane size and weight.

#### Model With Turbojet Flow and $H_2O_2$ Scramjet Nacelle

This section of the report discusses data obtained on two configurations having the  $H_2O_2$  scramjet nacelle operating in conjunction with the turbojets ( $\epsilon = 20^\circ$  with and without flow fences). The basic force and pitching-moment data for these two configurations along with corrections for turbojet and scramjet thrust are discussed in appendix C. The range of data showing the effect of flow fences on aerodynamics with burning in the scramjets is limited ( $M_\infty = 0.6$  to  $0.85$  at  $\alpha = 0^\circ$  only). However, figure 18 shows available increments in drag, lift, and pitching-moment coefficient resulting from the flow fences. The increments in lift and pitching moment in figure 18 agree with the trend shown earlier in figure 14 for the flowthrough nacelle configuration but the drag increment does not. The drag increment is negative at Mach 0.6 and 0.8 and goes positive by a small amount at Mach 0.85. The reason the drag decreases with the addition of flow fences at the two lower Mach numbers instead of increasing as before is not known. If the drag increment due to the fences becomes negligible at angle of attack, as happened for the flowthrough nacelle configuration, then the predominant effect of fences is on the lift and pitching moment. In this case, the adverse effects resulting from the addition of flow fences would not be altered significantly with or without burning in the scramjets.

#### SUMMARY OF RESULTS

An investigation of the effects of the operation of a combined turbojet/scramjet propulsion system installation on the longitudinal aerodynamic

characteristics of a hypersonic airbreathing launch vehicle (ABLV) at Mach 0.3 to 1.2 yielded the following results:

#### Operation Without Turbojet

1. The untrimmed lift-drag ratio of the body with tails was about 70 percent less at transonic speeds than at subsonic speeds because of the large transonic drag rise of the configuration.
2. The lift-drag ratio of the body with tails is reduced approximately 50 percent by addition of the flowthrough nacelle, and the lift-drag ratio of the complete configuration (body, tails, and nacelle) is further reduced by about 50 percent or more by the drag rise at transonic speeds.
3. The presence of flow fences did not significantly affect longitudinal aerodynamic characteristics.

#### Operation With Turbojet

1. Flow fences had a significant adverse effect on longitudinal aerodynamic characteristics of both the flowthrough nacelle configuration and the hydrogen peroxide scramjet nacelle configuration.
2. The angle between the downstream surface of the cutouts provided in the lower afterbody for the turbojet exhaust and the lower afterbody surface had only a moderate influence on aerodynamic forces. An angle of  $10^\circ$  appeared to give better aerodynamic performance for an assumed turbojet pressure ratio schedule than angles of  $5^\circ$  and  $20^\circ$ .
3. For the flowthrough inlet configuration, turbojet operation reduced untrimmed lift-drag ratios an average of about 6 percent over the Mach number range. Flow fences produced a further reduction in lift-drag ratio of about 18 percent at Mach 0.6 and about 7 percent at Mach 1.0.

Langley Research Center  
National Aeronautics and Space Administration  
Hampton, VA 23665  
May 11, 1977

## APPENDIX A

### APPARATUS AND METHODS

Details of the model, instrumentation, and data reduction not discussed in the main body of the report are contained in this appendix.

#### Model

Turbojet and scramjet engines.- As mentioned in the main text, engine mass flow requirements and model volume restraints required the use of  $H_2O_2$  for turbojet and scramjet engine exhaust flow simulation. Otherwise, air would have been used as a simulant to avoid complications associated with a  $H_2O_2$  model. Hydrogen peroxide was supplied to the model by two lines in the support strut that were connected to separate control valves at the supply end. All equipment upstream of the control valves, the control valves, and lines to the model are part of the tunnel  $H_2O_2$  system. The supply lines terminated in a two-compartment manifold that was attached to the main balance support. (See fig. 3.) From this manifold, separate supply lines crossed the main balance to separate manifolds for the turbojet and scramjet decomposition chambers. The lines crossing the balance were coiled or arranged so that a spring action was obtained from the lines with movement of the model.

Force balance.- A two-balance approach was selected in the design stage of the model for this investigation so that forces acting on the model could be separated and incremental forces measured more accurately than possible with a single balance. The entire model was cantilevered from the support strut by the main balance and a rear balance supported that part of the model downstream of station 103.15 (maximum cross-sectional area station). A 0.254-millimeter-thick brass strip was used for a seal between the forebody and afterbody at this station. The afterbody was free to move relative to the turbojet nozzles that protruded downstream of station 103.15. A water-cooled balance was selected for the afterbody, or rear, balance because the balance would be in contact with parts of the model washed by the hot exhaust from the turbojet nozzles. Calculations made during the design of the model indicated that the amount of heat (by conduction) reaching the balance could be handled by the cooling water jacket. By allowing the model to cool down between engine operation periods, the heat input to the jacket would be held to a minimum. However, during initial runs with the turbojet engines operating, high temperatures (755 K) were measured on the balance nut and somewhat lower temperatures were measured on the outside of the cooling water jacket. This high temperature environment around the balance resulted in large zero shifts that invalidated the data and eventually led to damage of the strain-gage lead wires from the balance beams. The thermocouple on the balance nut showed an almost immediate rise in temperature upon initiation of turbojet engine flow and this fact was taken as an indication of the leakage of hot (approximately 1000 K) exhaust gases past the seal between the forebody and afterbody. The suspected leakage path is shown in figure 19.

## APPENDIX A

Any leakage that may be inherent with this type of seal is believed to have been increased by deflection of the afterbody relative to the forebody and by the compound curvature of the seal strip (0.254-mm-thick brass). The curved shape of the seal slot caused stiffening of the seal strip and prevented the strip from acting as an effective seal in the region of the turbojet nozzles. There was no evidence of leakage from within the model to the outside past the seal elsewhere on the model. Because of the manner in which the model was constructed, there were no escape passageways from the balance cavity for leakage flow. Therefore, it was assumed that any leakage flow merely pressurized the balance cavity.

Test procedures were modified and quartz-type insulation was packed around the balance but these measures did not reduce the effects of the basic design fault significantly. Consequently, all data obtained from the rear balance before it was replaced by a dummy balance were considered to be invalid and are not included in this report.

### Instrumentation

Model instrumentation included sensors for turbojet and scramjet total pressures and temperatures, static pressures on the ramps and in the seal area, model internal pressures and temperatures and turbine-type flowmeters for scramjet and turbojet mass flow rates. The flowthrough inlet had two total-pressure rakes in one of the four passageways for obtaining an approximate mass flow rate for the inlet. Total pressure and temperature probes were located in every other turbojet and scramjet engine. It was assumed that the average of these three measurements would be indicative of the average value for six engines. Calculations of an average total pressure from the measured mass flow rates showed that the assumption was true within approximately 1 percent. Static pressure tap locations on the afterbody ramps are shown in figure 5. All pressures were measured by strain-gage transducers; the outputs from these transducers, the thermocouples, and the balance were recorded on magnetic tape and later processed by computer.

### Data Reduction

Force data.— Balance axial and normal forces and pitching moments were reduced to coefficient form after corrections for balance restraints and tare forces were made. Lift, drag, and pitching-moment coefficients referenced to the stability axis were then determined. The main balance was calibrated after each configuration change that altered the  $H_2O_2$  supply lines across the balance, for example, when the  $H_2O_2$  scramjet nacelle was replaced by the flowthrough nacelle and vice versa.

Pressure data.— Turbojet and scramjet total pressure ratios were obtained from the ratio of the average of the three total-pressure measurements to the tunnel static pressure. Static pressures measured on the ramp were reduced to coefficient form by using a calculated free-stream dynamic pressure and the tunnel static pressure.

## APPENDIX A

### Procedure for calculation of $C_{A,TJ}$ , $C_{N,TJ}$ , and $C_{m,TJ}$ .- Turbojet thrust

was originally planned to be determined from the two balance readings and to be cross-checked with the thrust obtained from static tests. The loss of the rear balance and other factors required reliance on static tests of a single turbojet engine for thrust values of the complete turbojet propulsion system. These static test data are presented in figure 20 (after being multiplied by six) along with three data points obtained for the complete model mounted in the tunnel. The line faired through the data was used in determining the thrust for a given  $p_{t,TJ}$  value for all values of  $C_{A,TJ}$ ,  $C_{N,TJ}$ , and  $C_{m,TJ}$  in this report. Normal and axial components of the thrust used in calculating these coefficients were determined by using the geometry shown in figure 21. As mentioned in the main text, the thrust was assumed to act perpendicular to, and at, the nozzle exit plane.

A correction was applied to the thrust to account for the difference between the external pressure for the static tests and the tunnel static pressure at a given Mach number, that is,

$$T_{TJ} = T'_{TJ} + A_{TJ}(p_s - p_\infty)$$

where

$T_{TJ}$  total turbojet thrust

$T'_{TJ}$  thrust from figure 20 for a given  $p_{t,TJ}$

$A_{TJ}$  total exit area of turbojet nozzles, 0.0427 m<sup>2</sup>

$p_s$  external static pressure for static conditions

$p_\infty$  tunnel static pressure

Then, from figure 21, the equations for  $C_{A,TJ}$ ,  $C_{N,TJ}$ , and  $C_{m,TJ}$  were determined and are as follows:

$$C_{A,TJ} = \frac{6T \cos \delta}{q_\infty A_{ref}} = \frac{T_{TJ} \cos \delta}{q_\infty A_{ref}}$$

$$C_{N,TJ} = \frac{2T \sin \delta (\cos \theta_1 + \cos \theta_2 + \cos \theta_3)}{q_\infty A_{ref}}$$

$$= \frac{2T_{TJ} \sin \delta \cos \theta_1 + \cos \theta_2 + \cos \theta_3}{6 q_\infty A_{ref}}$$

# APPENDIX A

$$C_{m,TJ} = \left[ \frac{C_{A,TJ}}{3} (\ell_{A,1} + \ell_{A,2} + \ell_{A,3}) + C_{N,TJ} \ell_N \right] \frac{1}{\ell_{ref}}$$

where  $\delta$ ,  $\theta$ ,  $\ell_A$ , and  $\ell_N$  are defined in figure 21 and all other symbols are defined in the section "Symbols."

## APPENDIX B

### CALCULATION OF MODEL DRAG RISE USING RAXBOD

A program for the analysis of steady, inviscid, irrotational, transonic flow over axisymmetrical bodies in free air called RAXBOD (refs. 8 and 9) was investigated as a possible means of determining analytically the drag rise of the ABLV model. RAXBOD solves the exact equation for the disturbance velocity potential and uses the exact surface boundary condition of axisymmetric shapes. To input the ABLV model into this program, a modified equivalent body of revolution based on the area distribution curves of figure 4 was required. The modification to the equivalent body of revolution consisted of replacing the pointed nose with a hemisphere-cylinder nose (fig. 22). This modification was necessary to adapt the concave forebody to the coordinate system used in the program. (A body-normal coordinate system is used up to the first horizontal tangent and a sheared cylindrical system thereafter.) The output of interest from this program was the drag coefficient obtained by integration of the calculated pressure coefficient distribution over the body.

The bodies of revolution obtained from the cross-sectional area distributions were altered slightly so that the shape could be described as an arrangement of straight line slopes and segments of circles. The small relatively steep slope beginning at  $x = 87.68$  on the flowthrough nacelle configuration in figure 22 was included in the input data describing the body, but apparently this geometry change occurred over a distance smaller than the final grid size and was ignored by the program.

The results obtained from the program for the two equivalent bodies are compared with experimental data in figure 23. To make these comparisons, the calculated drag coefficients were first converted to coefficients based on the model reference area and then increments in  $C_D$  with Mach number were obtained by using the calculated  $C_D$  for the lowest Mach number as a reference. These increments were then added to the experimental  $C_D$  at the reference Mach number to obtain a calculated  $C_D$  variation with Mach number. The experimental data for the flowthrough nacelle configuration are from figure 6(d) whereas the no jet flow data were used for the  $H_2O_2$  nacelle configuration. Both experimental and RAXBOD results are for  $\alpha = 0^\circ$ .

In figure 23(a) RAXBOD predicts the drag rise very well up to  $M_\infty = 0.98$  but above this speed the results from the program depart radically from the data. There is essentially no agreement between calculated and experimental results in figure 2(b) for the  $H_2O_2$  nacelle configuration. The agreement noted in figure 2(a) below Mach 0.98 may be fortuitous but as noted in reference 8, the coordinate system used in the program is not well suited for bodies with slope discontinuities. Since the program ignored the small "bump" at  $x = 87.68$  for the flowthrough nacelle configuration, this body may appear "smoother" to the program than the  $H_2O_2$  nacelle configuration and may result in greater computation accuracy. The program was exercised prior to the tunnel tests and no attempts subsequent to the tests have been made to adjust the input data or the program to see whether a better match could be made between the calculated and experimental data.



## APPENDIX B

It was observed that program results were not sensitive to moderate (10 percent) changes in the area distribution over the rear of the body. From the exploratory effort seen here, it appears that RAXBOD could be used to some advantage on configurations that are not within the scope of configurations for which the program was intended.

## APPENDIX C

### MODEL FORCE AND MOMENT DATA WITH ENGINES OPERATING

#### Model With Flowthrough Nacelle

Axial-force, normal-force, and pitching-moment coefficients as a function of turbojet pressure ratio are presented in figures 24 to 27 for all configurations investigated with the flowthrough nacelle. In these figures, the symbols indicate data points taken during a jet pressure ratio sweep and these data, therefore, include axial and normal forces and pitching moments contributed by turbojet thrust.

Axial-force, normal-force, or pitching-moment coefficients ( $C_{A,TJ}$ ,  $C_{N,TJ}$ , or  $C_{m,TJ}$ , respectively) attributed to the thrust of the turbojets is presented in each plot. (The procedure for determining these coefficients is discussed in the data reduction section of appendix A.) The curves of  $C_{A,TJ}$ ,  $C_{N,TJ}$ , and  $C_{m,TJ}$  were then used to adjust the experimental data for the effects of turbojet thrust. The adjusted force and moment coefficient curves are identified as "corrected data" in the symbol key in figures 24 to 27. The turbojet thrust was assumed to act along the center line of the nozzle at the nozzle exit plane so that any forces resulting from the exhaust flowing over surfaces external to the nozzle were considered to be aerodynamic forces.

#### Model With H<sub>2</sub>O<sub>2</sub> Scramjet Nacelle

Two configurations were tested with the H<sub>2</sub>O<sub>2</sub> scramjet nacelle operating in conjunction with the turbojets. These configurations were the  $\epsilon = 20^\circ$  model with and without flow fences. Axial-force, normal-force, and pitching-moment coefficient data as a function of turbojet pressure ratio for these configurations are presented in figures 28 and 29 for constant values of scramjet pressure ratio. Scramjet thrust could not be determined with certainty because of limited static test data and because the scramjets were operated below the choke point ( $p_{t,SJ}/p_\infty < 1.82$ ) in several instances. However, estimated values for  $C_{A,SJ}$ ,  $C_{N,SJ}$ , and  $C_{m,SJ}$  are given, it being assumed that the scramjet acted perpendicular to and at the center of the plane of the nozzle throat. The data have been corrected for components of the turbojet thrust as were done previously for the flowthrough inlet configurations.

Force and moment coefficients for model with flow fences.— Axial-force, normal-force, and pitching-moment data for the  $\epsilon = 20^\circ$  configuration with flow fences (fig. 28) follow the same general trend noted earlier for the same model with the flowthrough nacelle (fig. 26). There is an increase in drag, a decrease in lift, and a nose-up pitching-moment increment as turbojet pressure ratio increases. The rate of increase in axial force with increasing turbojet pressure ratio is greater than that obtained for the flowthrough nacelle configuration at the three test Mach numbers. The reason or reasons for this result is not known but it is believed that one of the contributing factors is that the hot scramjet exhaust flow affects the mixing action between the engine and external flows over the lower afterbody. Comparing the no-turbojet engine

## APPENDIX C

flow axial-force coefficient (that is,  $p_{t,TJ}/p_{\infty} = 1.0$ ) obtained for the flow-through nacelle configuration (fig. 26) with that for the  $H_2O_2$  nacelle configuration (solid symbol in fig. 28) shows that there is very little difference in axial force between the two configurations. This was not expected because the  $H_2O_2$  nacelle configuration has a large base area (approximately  $0.009 \text{ m}^2$  or 2.5 percent of the model reference area) and the nacelle "shadows" a substantial portion of the lower afterbody surface. (Note the difference in  $C_N$  with and without scramjet flow at  $p_{t,TJ}/p_{\infty} = 1$  in fig. 28.) The inlet fairing of the  $H_2O_2$  nacelle represents a rather large axial area, and lower than ambient pressures acting over this area could produce a thrust force equivalent to the base drag of the nacelle.

Force and moment coefficients for model without flow fences.— Force and moment coefficients obtained for the  $\epsilon = 20^\circ$  configuration without flow fences are presented in figure 29. The estimated correction for scramjet thrust is presented in the symbol key at the top of the figure to avoid a profusion of curves that would result if the correction was presented as in figure 28. The data have been corrected for components of turbojet thrust as described previously.

The large decrease (more negative) in axial coefficient at Mach 0.6 noted in figure 29(a) between  $\alpha = 0^\circ$  and  $\alpha = 2^\circ$  and between  $\alpha = 2^\circ$  and  $\alpha = 4^\circ$  at Mach 0.8 in figure 29(b) runs counter to results obtained on all configurations with the flowthrough nacelle. Also at Mach 0.9 in figure 23(d), the variation of axial-force coefficient with turbojet pressure ratio is very nonlinear and the axial force for  $\alpha = 2^\circ$  and  $\alpha = 4^\circ$  is more positive than that for  $\alpha = 0^\circ$ . The nonlinear variation at  $\alpha = 2^\circ$  in figure 29(d) may be the result of balance fouling or fouling of the  $H_2O_2$  lines across the balance but it is not clear why this would occur for only one set of data in the middle of a run. Other than these anomalies, the data follow trends noted previously and the corrected axial-force coefficient curve has a greater slope at all Mach numbers than that obtained for the flowthrough nacelle configuration (fig. 27).

The difference between the open and solid symbols at  $p_{t,TJ}/p_{\infty} = 1$  on the axial-force coefficient plots in figure 29 should represent the combination of the base drag of the nacelle, the axial component of scramjet thrust, and an increment in axial force on the lower afterbody surface. This was found to be generally true at or below  $M_{\infty} = 0.9$  by summing  $C_{A,SJ}$  and a calculated base drag increment based on the assumption that the scramjet total pressure reading without scramjet flow was indicative of the base pressure on the nacelle. (For example, at  $M_{\infty} = 0.6$  and  $\alpha = 4^\circ$ , the calculated difference was 0.0107 and the measured difference 0.0104; at  $M_{\infty} = 0.8$  and  $\alpha = 2^\circ$  the calculated difference was 0.0084 and the measured difference 0.0095.) At Mach 1.0 and 1.2 the difference between  $C_A$  with and without scramjet flow at  $p_{t,TJ}/p_{\infty} = 1$  is seen to be small or nonexistent. Apparently, at subsonic speeds scramjet thrust and base drag changes predominate over other flow field effects whereas at speeds above Mach 0.9 the opposite is true. With the turbojets operating, scramjet operation (that is, subsonic combustion in the scramjets) has a relatively small effect on longitudinal aerodynamics at all Mach numbers.

Effect of flow fences on aerodynamic forces.— Because of the lack of data for the configuration with flow fences, data showing the effect of flow fences

## APPENDIX C

on aerodynamic forces are limited to subsonic Mach numbers and  $\alpha = 0^\circ$  (fig. 18). The increments shown in figure 18 were computed from the data of figures 28 and 29 by the following procedure (drag coefficient increment being used as an example):

Because  $\alpha = 0^\circ$

$$C_{D,FF} - C_{D,NF} = (C_A - C_{A,TJ} - C_{A,SJ})_{FF} - (C_A - C_{A,TJ} - C_{A,SJ})_{NF}$$

Since

$$(C_{A,TJ})_{FF} = (C_{A,TJ})_{NF}$$

at the same turbojet pressure ratio, then

$$C_{D,FF} - C_{D,NF} = [C_{A,FF} - C_{A,NF}] - [(C_{A,SJ})_{FF} - (C_{A,SJ})_{NF}]$$

The last bracketed term in this equation corrects for the difference between  $p_{t,SJ}/p_\infty$  for the two configurations at a given value of  $M_\infty$ .

### Afterbody-Ramp Pressure Coefficient Distributions

Static pressures measured along the axis of one of the center cutouts in the afterbody ramp are presented in coefficient form in figure 30 as a function of distance along the cutout for the three ramp angles. At the top of each part of this figure is a section view of the ramp and cutout contour and a portion of the turbojet nozzle. This view is drawn to the same scale as the abscissa of the plots and the static taps in the drawing line up with the tap locations ( $x/l_{ref}$ ) of the center plot. Static taps along the entire length of the ramp were desired, but this was not practical because of limited space within the model and difficulties in making model changes.

Distributions for the  $\epsilon = 5^\circ$  configuration (fig. 30(a)) reflect the compression and expansion waves existing in the turbojet exhaust flow. The last orifice (at  $x/l_{ref} = 0.875$ ) appears to have been inoperative as it shows very little change with jet pressure ratio  $p_{t,TJ}/p_\infty$ . Distributions for the other two ramp angles in figures 30(b) and 30(c) show that the exhaust flow expands to very low pressures at the end of the cutout. Separation of the exhaust flow from the afterbody at or downstream of this point is not clearly evident although several of the distributions may be interpreted as showing a separated flow condition.

Although the low pressures exist over a relatively small distance, this distance represents a significant area. The data in figure 30 were obtained with the flow fences installed on the model so it would be reasonable to expect that the fences contributed to the observed flow condition. However, in figure 31 where distributions are shown for comparable turbojet pressure ratios with and without flow fences, it is seen that the flow fences had very little effect on pressures existing in the cutout. Whether this would be true for the cutouts adjacent to the fences is open to question.

## APPENDIX C

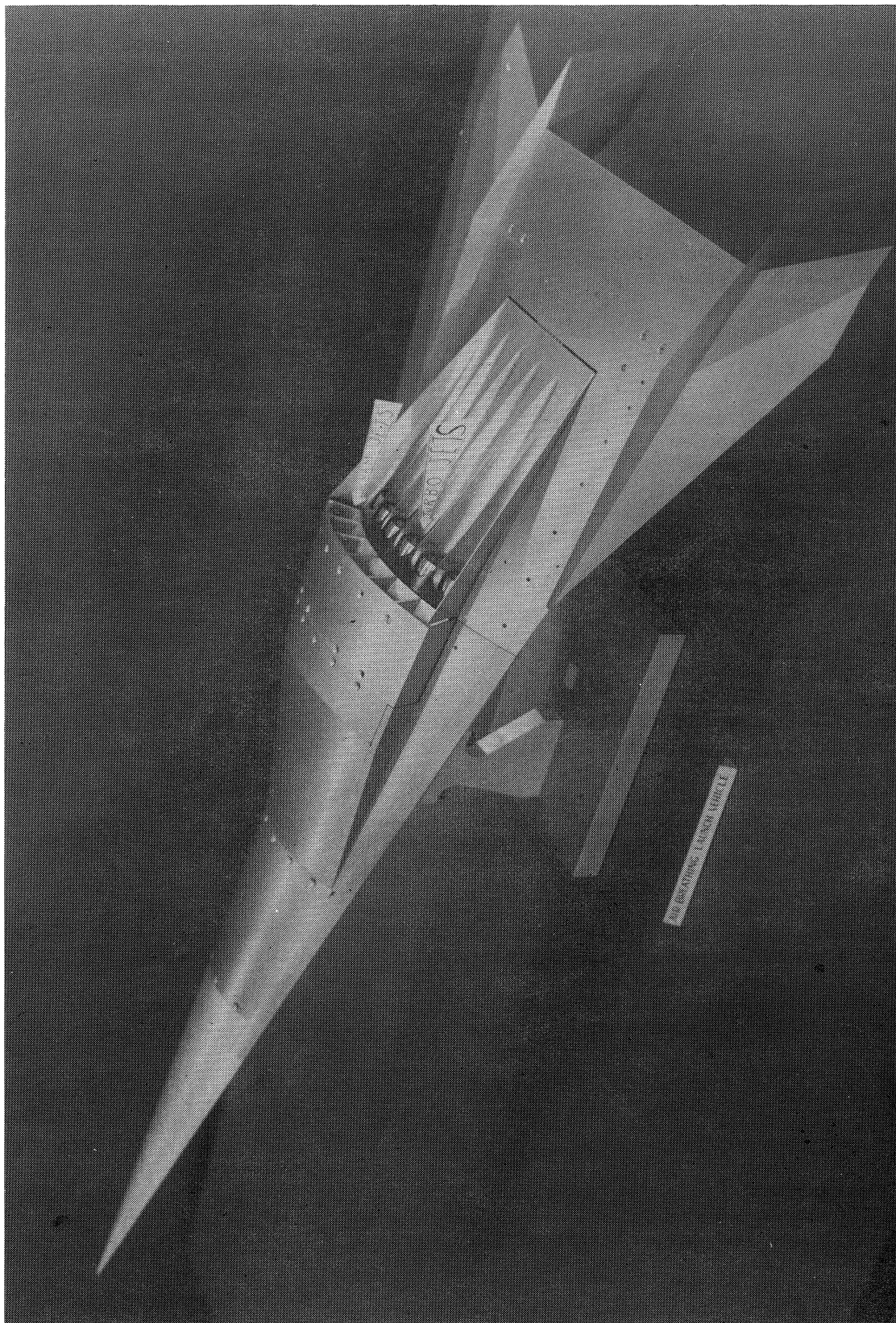
In both figures 30 and 31, the distributions for the no turbojet flow condition generally show very little change in pressure along the cutout and the level of  $C_p$  (greater negatively than -0.02 with few exceptions) is more negative than would be expected. The cross-sectional area distribution of the first part of the model afterbody is nearly equivalent to that of a conical afterbody with an  $8^\circ$  boattail angle. Data from reference 10 show that  $C_p$  on the boattail of an  $8^\circ$  conical afterbody at  $M_\infty = 0.6$  reaches a maximum negative value of about 0.25 at the beginning of the boattail and increases positively along the boattail. The average  $C_p$  value in reference 10 is between about -0.025 for the afterbody with no base and -0.10 for the afterbody with a large base (85 percent of the maximum afterbody diameter). The large increase in drag noted in the body of this report when the flowthrough nacelle was added to the body possibly stems in part from the fact that the inlet lowers afterbody pressures well below the pressures that would normally be expected to exist without the nacelle. Unfortunately, pressures were not measured on the blank afterbody ramp used for the "no engines" configuration; therefore, the effect of the nacelle on the lower afterbody pressures cannot be determined from the data obtained.

## REFERENCES

1. Becker, John V.; and Kirkham, Frank S.: Hypersonic Transports. Vehicle Technology for Civil Aviation - The Seventies and Beyond, NASA SP-292, 1971, pp. 429-445.
2. Nagel, A. L.; and Becker, John V.: Key Technology for Airbreathing Hypersonic Aircraft. AIAA Paper No. 73-58, Jan. 1973.
3. Becker, John V.: New Approaches to Hypersonic Aircraft. Paper presented at the Seventh Congress of the International Council of the Aeronautical Sciences (Rome, Italy), Sept. 1970.
4. Morris, R. E.; and Williams, N. B.: Study of Air Breathing Launch Vehicles With Cruise Capability.  
Volume I - Summary. NASA CR-73194, 1964.  
Volume II - Synthesis, Performance, Cost and Evaluation. NASA CR-73195, 1964.  
Volume III - Aerodynamics, Propulsion and Subsystems. NASA CR-73196, 1964.  
Volume IV - Thermodynamics, Structures, and Weights. NASA CR-73197, 1964.  
Volume V - Economics Model. NASA CR-73198, 1964.  
Volume VI - Technology. NASA CR-73199, 1964.
5. Corson, Blake W., Jr.; Runckel, Jack F.; and Igoe, William B.: Calibration of the Langley 16-Foot Transonic Tunnel With Test Section Air Removal. NASA TR R-423, 1974.
6. Runckel, Jack F.; and Swihart, John M.: A Hydrogen Peroxide Turbojet-Engine Simulation for Wind-Tunnel Powered-Model Investigations. NACA RM L57H15, 1957.
7. Willis, Conrad M.: The Effect of Catalyst-Bed Arrangement on Thrust Buildup and Decay Time for a 90 Percent Hydrogen Peroxide Control Rocket. NASA TN D-516, 1960.
8. South, Jerry C., Jr.; and Jameson, Anthony: Relaxation Solutions for Inviscid Axisymmetric Transonic Flow Over Blunt or Pointed Bodies. AIAA Computational Fluid Dynamics Conference, July 1973, pp. 8-17.
9. Keller, James D.; and South, Jerry C., Jr.: RAXBOD: A Fortran Program for Inviscid Transonic Flow Over Axisymmetric Bodies. NASA TM X-72831, 1976.
10. Silhan, Frank V.; and Cubbage, James M., Jr.: Drag of Conical and Circular-Arc Boattail Afterbodies at Mach Numbers From 0.6 to 1.3. NACA RM L56K22, 1957.

TABLE I.- GEOMETRIC CHARACTERISTICS OF MODEL AND OTHER DATA

Body:	
Length, theoretical, m . . . . .	1.443
Length, actual, m . . . . .	1.426
Maximum width, m . . . . .	0.375
Maximum height (without nacelle), m . . . . .	0.152
Aspect ratios:	
Body alone . . . . .	0.453
Body and horizontal tails . . . . .	1.141
Body with horizontal tails:	
Planform area, m <sup>2</sup> . . . . .	0.368
Span, m . . . . .	0.648
Horizontal tails:	
Area, exposed, each, m <sup>2</sup> . . . . .	0.0286
Span, exposed, each, m . . . . .	0.128
Aspect ratio exposed . . . . .	0.57
Root chord, exposed, m . . . . .	0.352
Sweepback angles:	
Leading edge, deg . . . . .	65
Trailing edge, deg . . . . .	30
Dihedral, deg . . . . .	0
Airfoil (maximum thickness at 70 percent of chord) . . . . .	Diamond
Airfoil thickness ratio . . . . .	0.05
Vertical tails:	
Area, each, m <sup>2</sup> . . . . .	0.0253
Span, m . . . . .	0.129
Aspect ratio . . . . .	0.65
Root chord, at fuselage center line . . . . .	0.422
Sweepback angles:	
Leading edge, deg . . . . .	64
Trailing edge, deg . . . . .	30
Airfoil (maximum thickness at 70 percent chord) . . . . .	Half diamond
Airfoil thickness ratio . . . . .	0.075
Turbojet nozzle:	
Throat diameter, m . . . . .	0.0240
Exit diameter, m . . . . .	0.0301
Exit Mach number (average) . . . . .	1.847
Conical type, half cone angle, deg . . . . .	7.0
Total exit area, 6 nozzles, m <sup>2</sup> . . . . .	0.00427
Scramjet nozzle:	
Throat area, m <sup>2</sup> . . . . .	0.000172
Exit area, m <sup>2</sup> . . . . .	0.00149
Total exit area, m <sup>2</sup> . . . . .	0.00894
H <sub>2</sub> O <sub>2</sub> parameters:	
Concentration, percent . . . . .	90
Total temperature after decomposition (average), K . . . . .	1000
Ratio of specific heats . . . . .	1.28
Gas constant, J/kg-K . . . . .	376.2

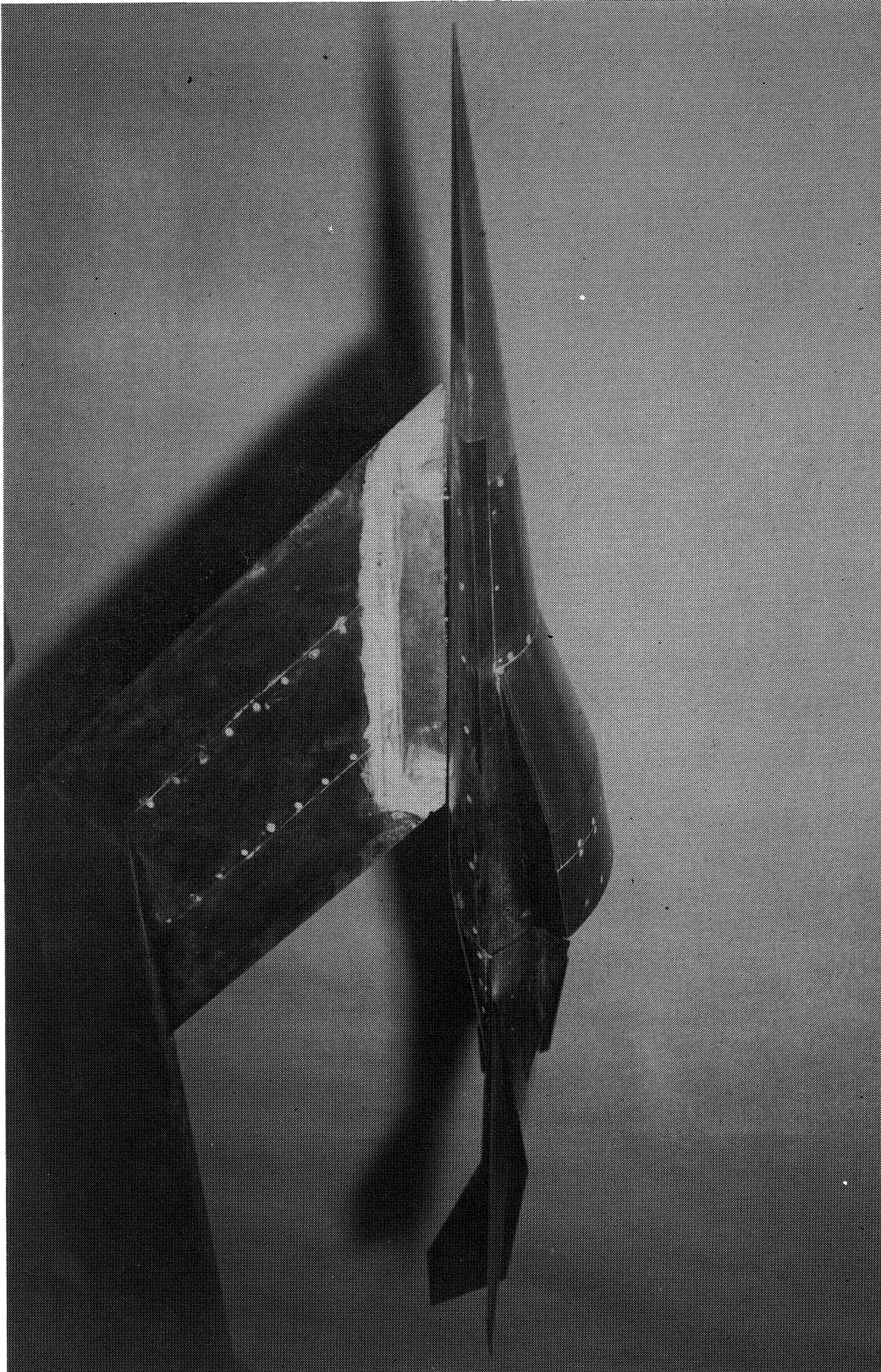


L-73-2744

(a) Bottom view of  $H_2O_2$  scramjet nacelle configuration.

Figure 1.- Photographs of 1/60-scale airbreathing launch vehicle model.

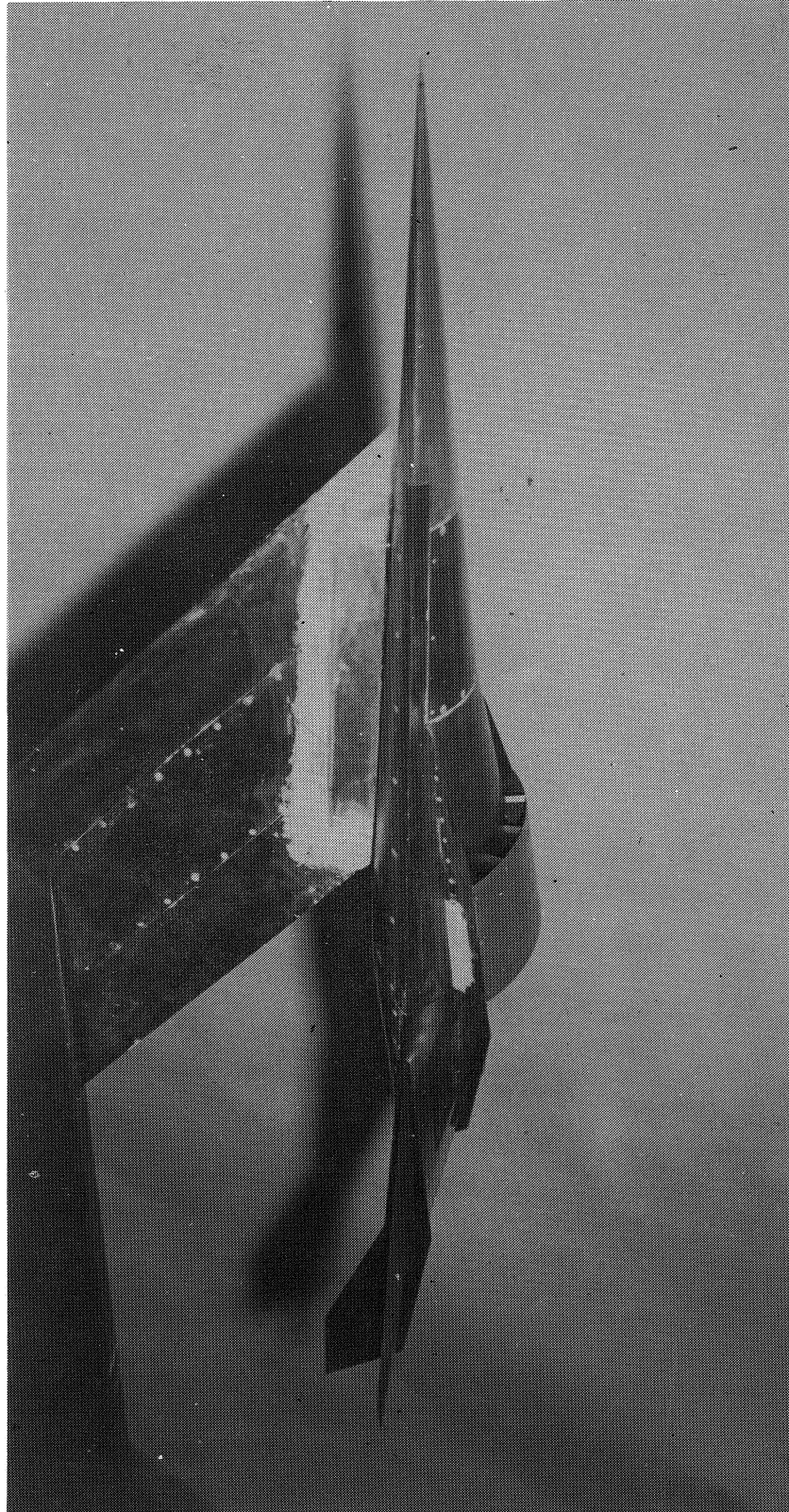




L-74-4676

(b)  $H_2O_2$  scramjet nacelle configuration mounted in tunnel.

Figure 1.- Continued.



L-74-4674

(c) Flowthrough nacelle configuration mounted in tunnel.

Figure 1.- Concluded.

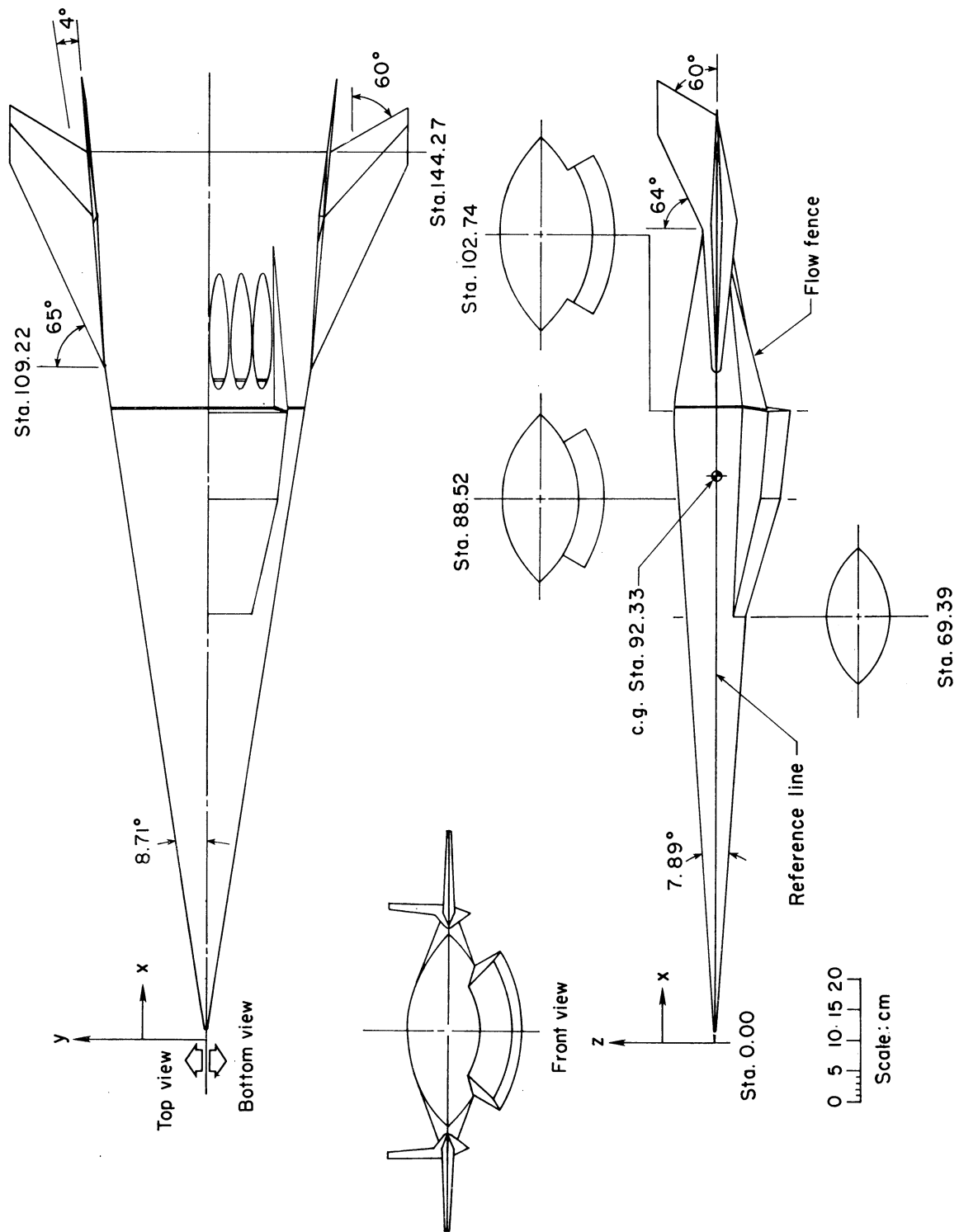


Figure 2.- Three-view drawing of 1/60-scale ABLV model. All dimensions are in centimeters.

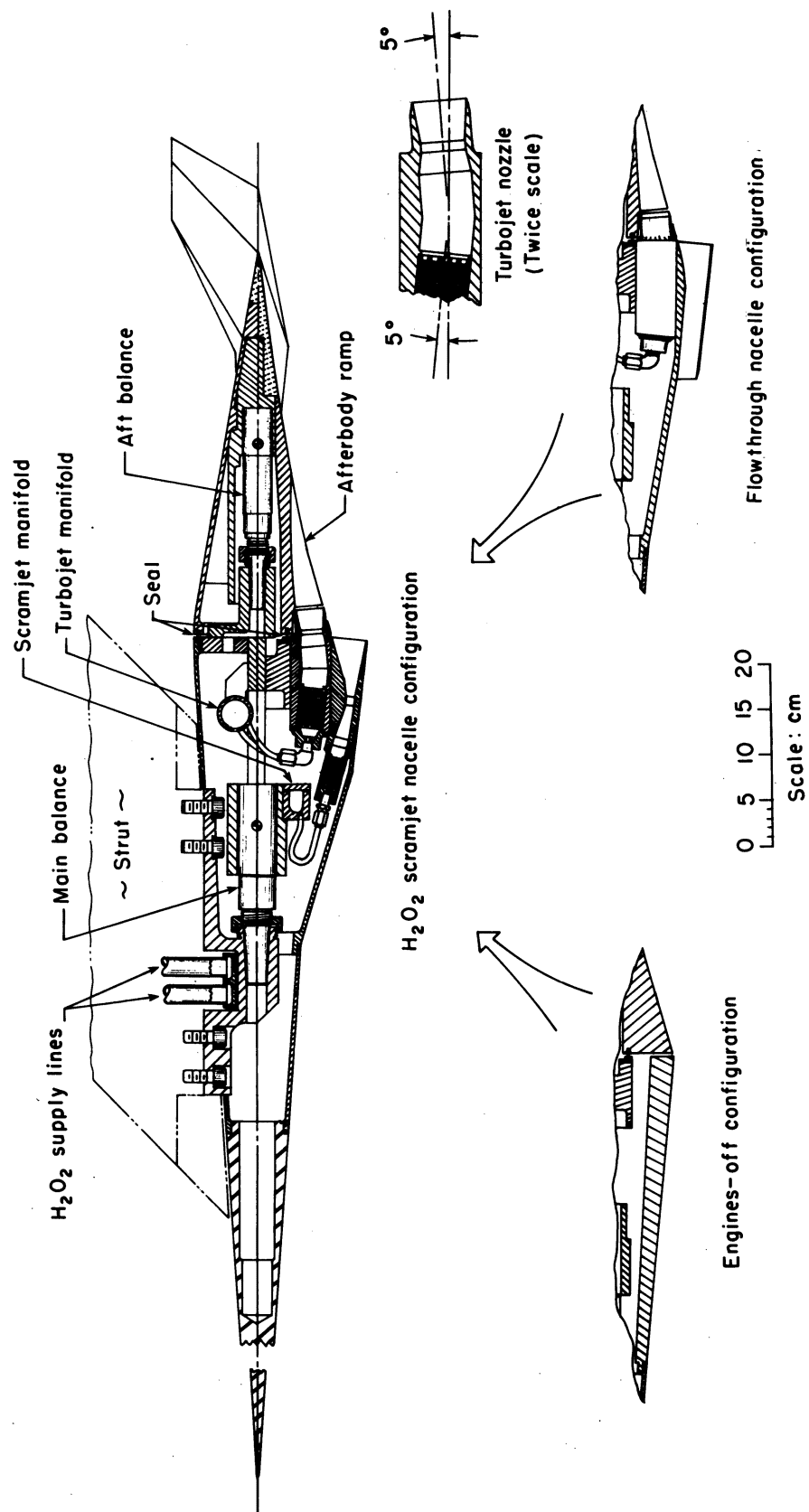


Figure 3.- Inboard section of model.

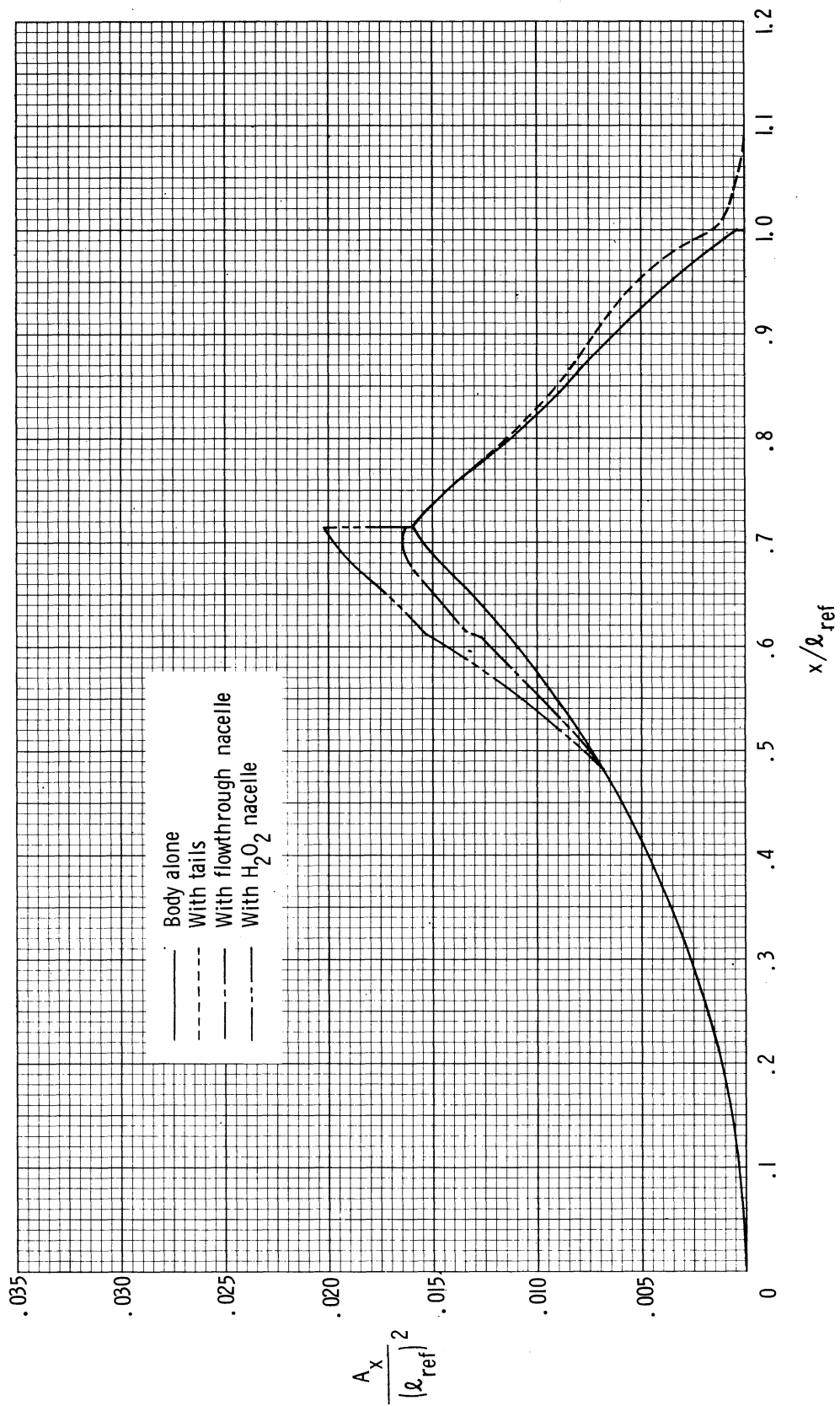


Figure 4.- Model cross-sectional area distributions.

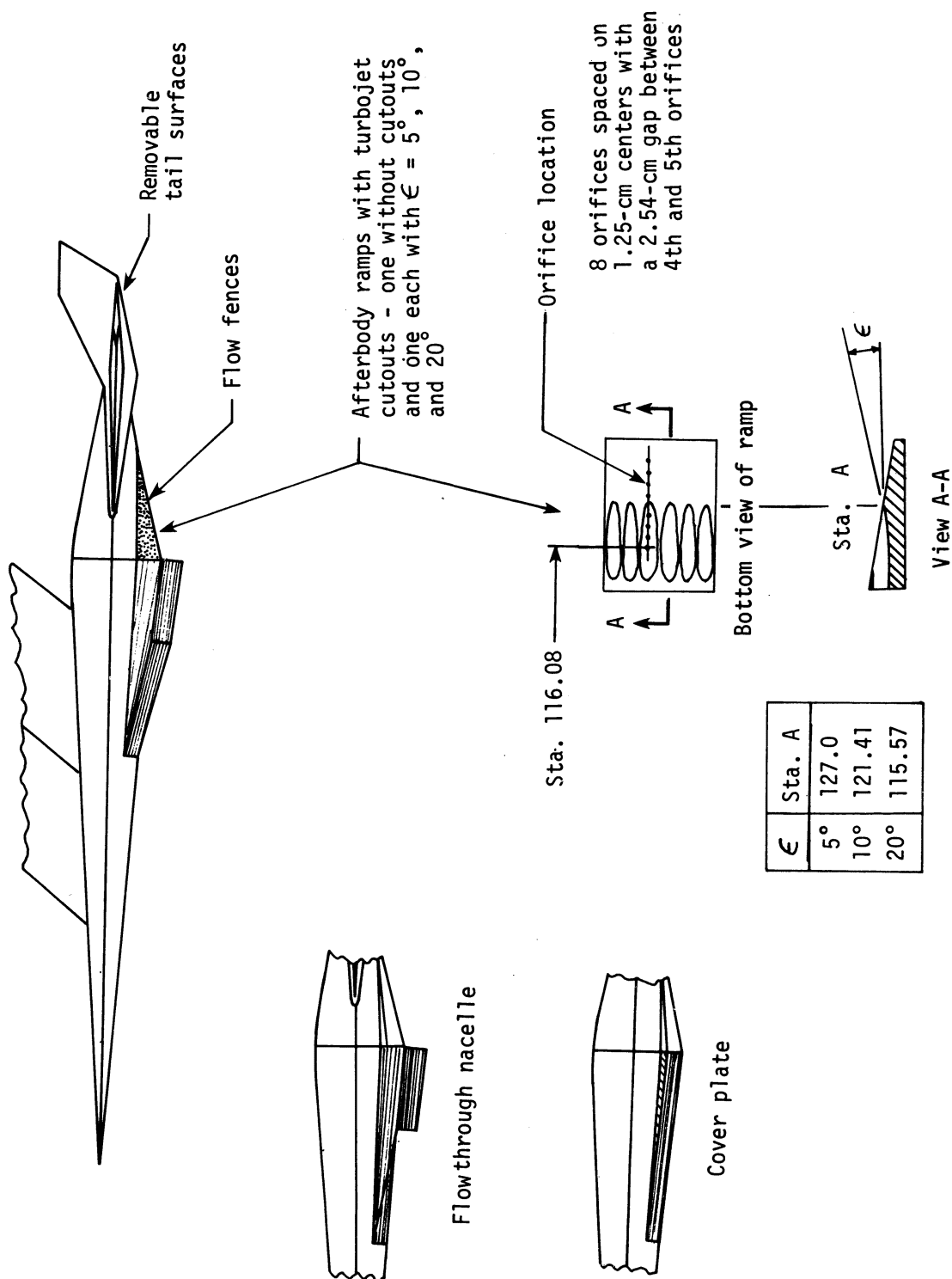
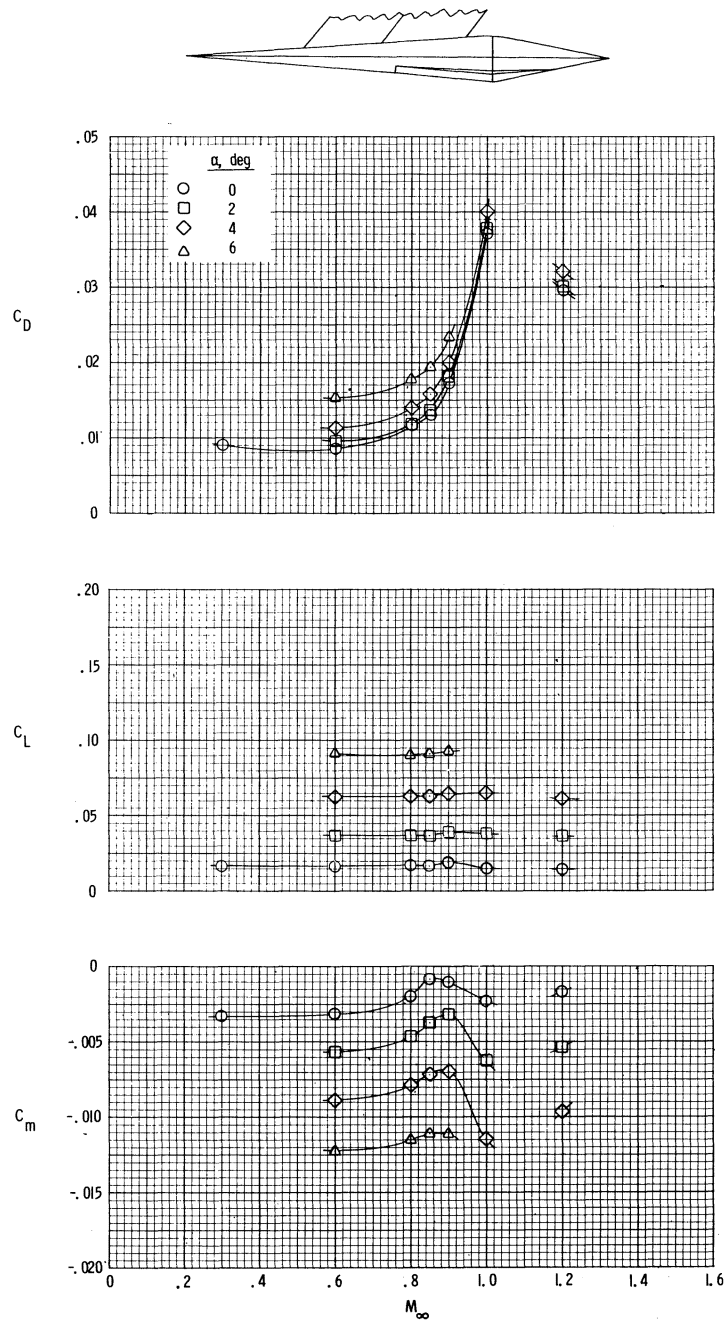


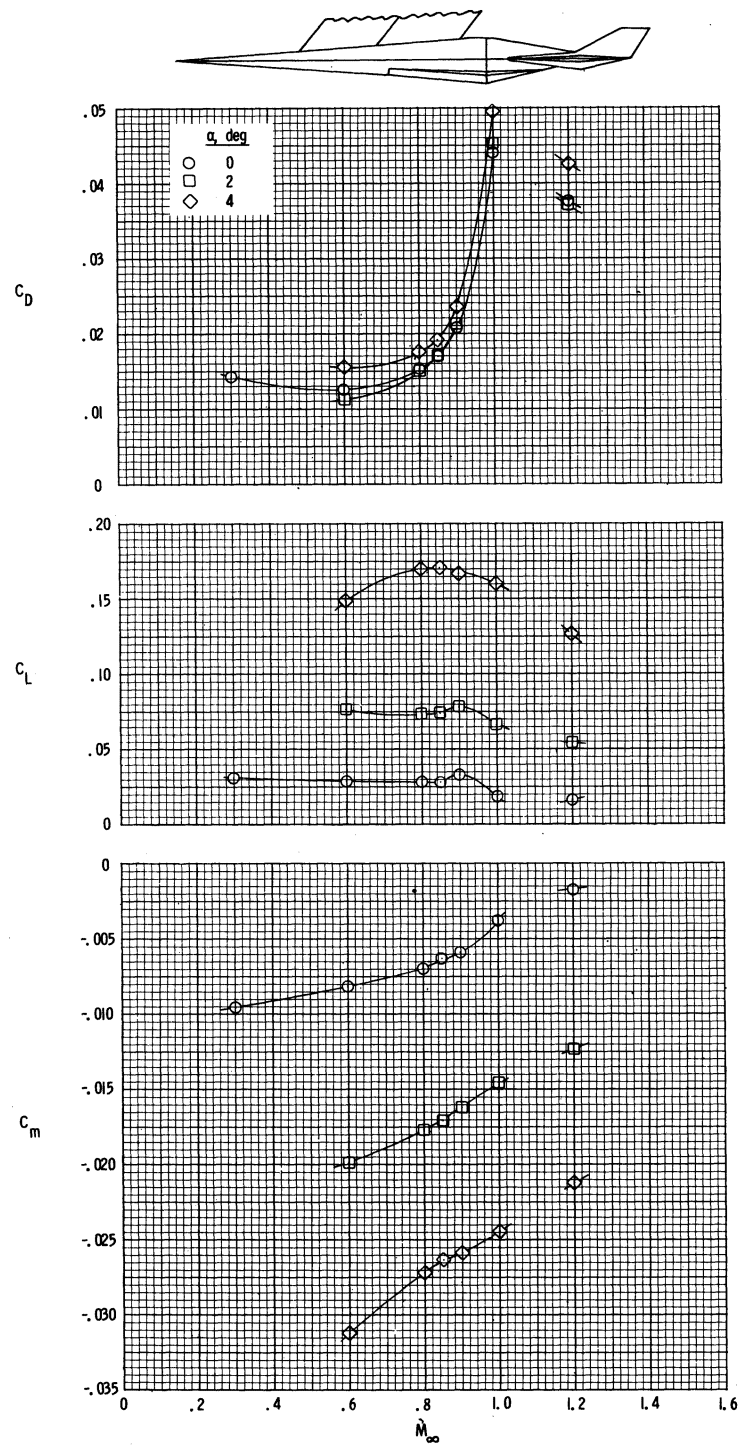
Figure 5.- Model geometry changes.





(a) Body alone.

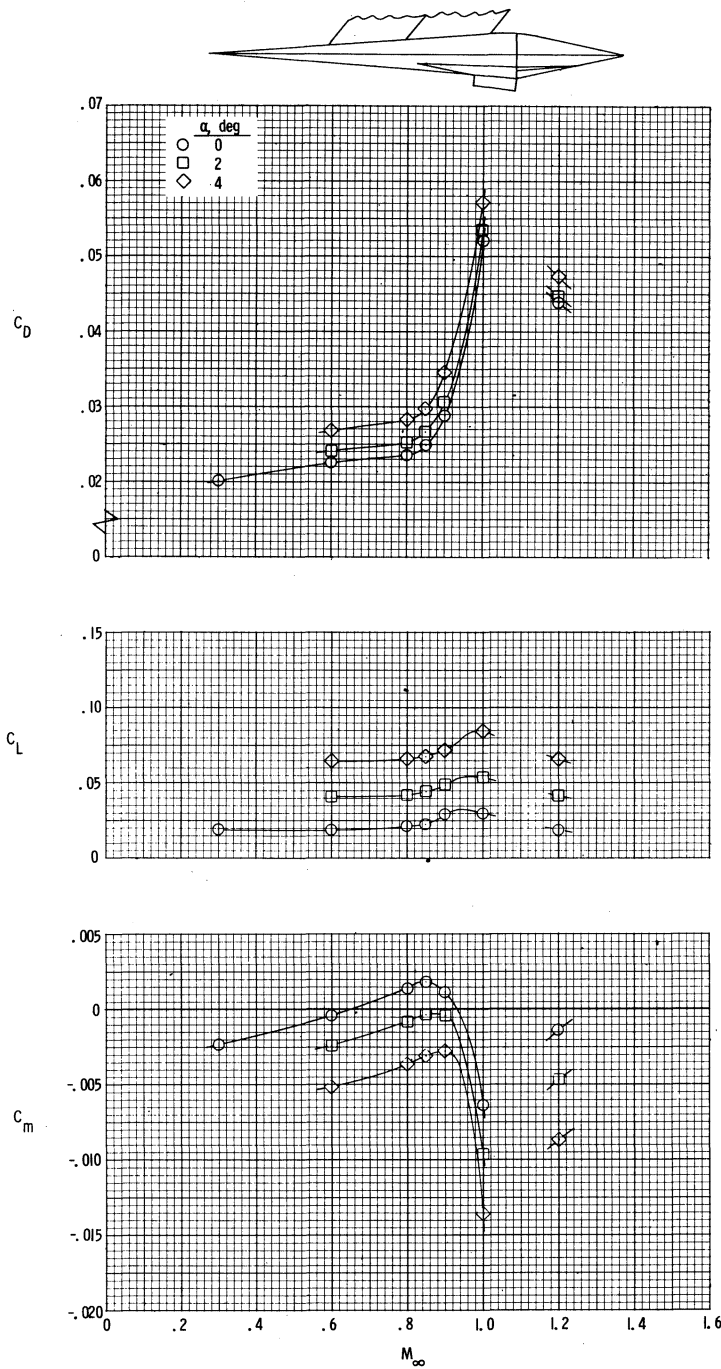
Figure 6.- Drag, lift, and pitching-moment coefficient variation with Mach number. No turbojet engines (afterbody ramp without turbojet cutouts).



(b) Body with tails.

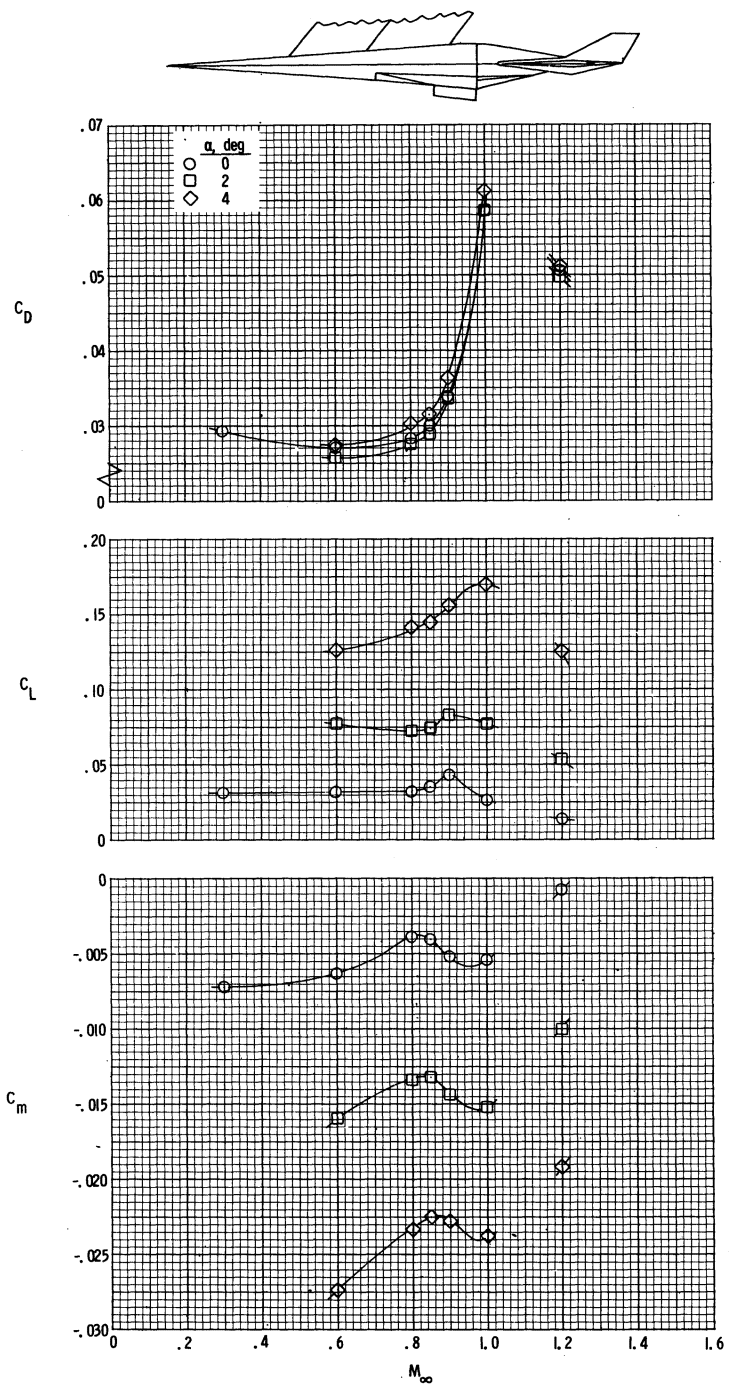
Figure 6.- Continued.





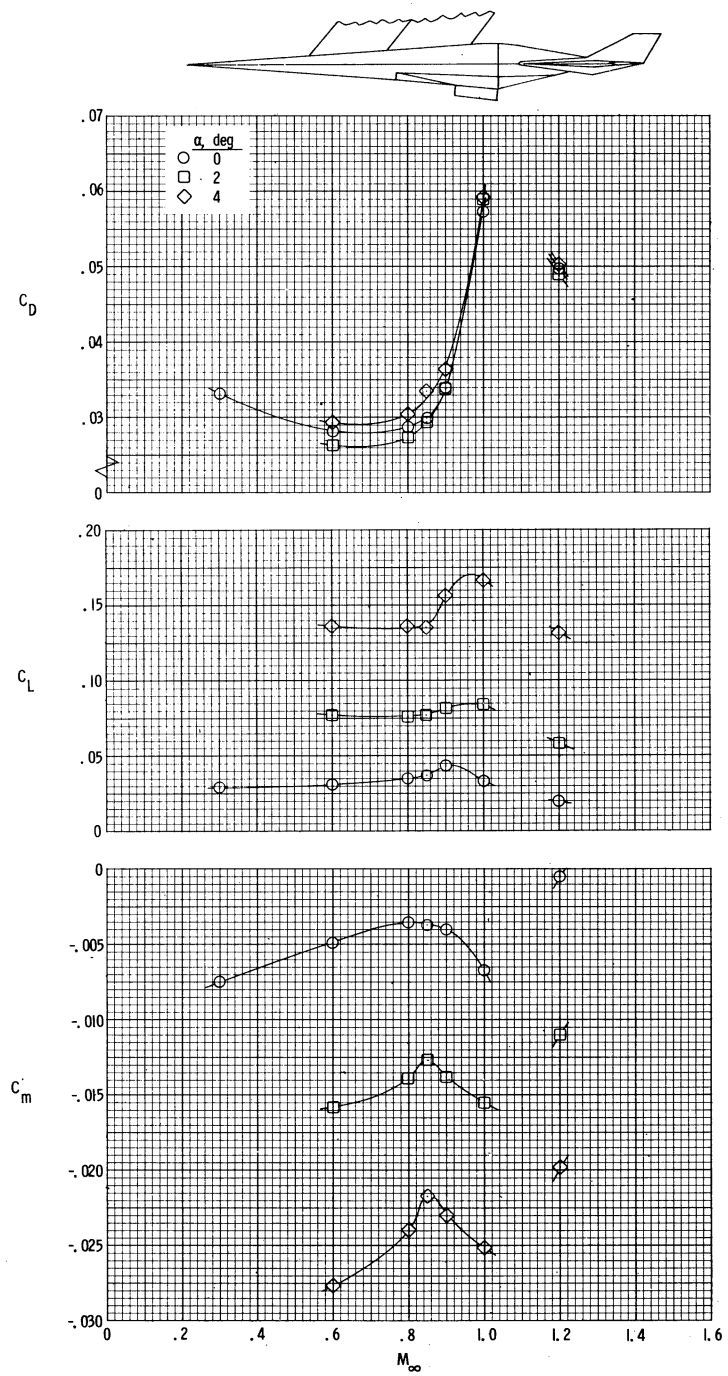
(c) Body with flowthrough nacelle.

Figure 6.- Continued.



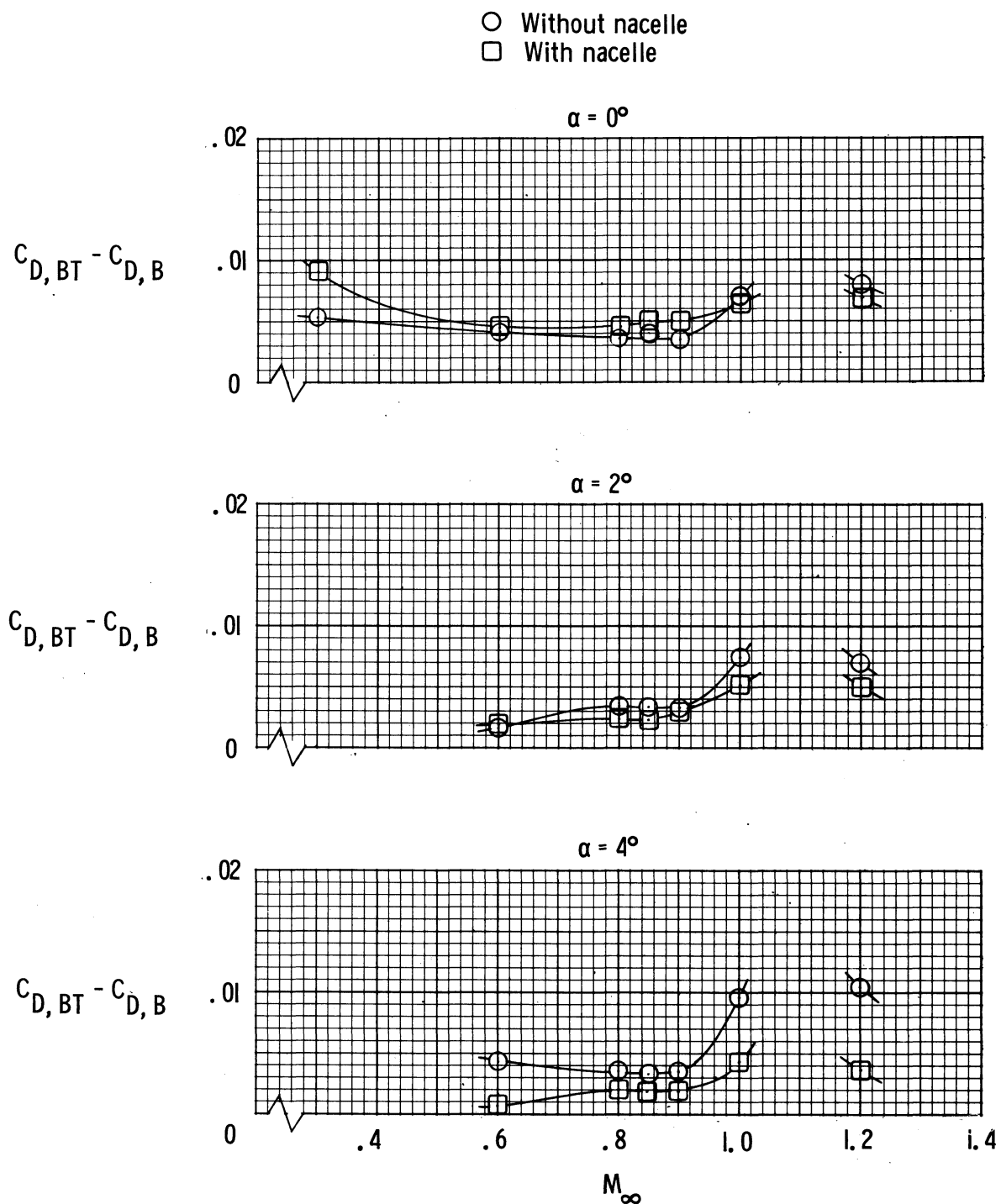
(d) Body with tails and flowthrough nacelle.

Figure 6.- Continued.



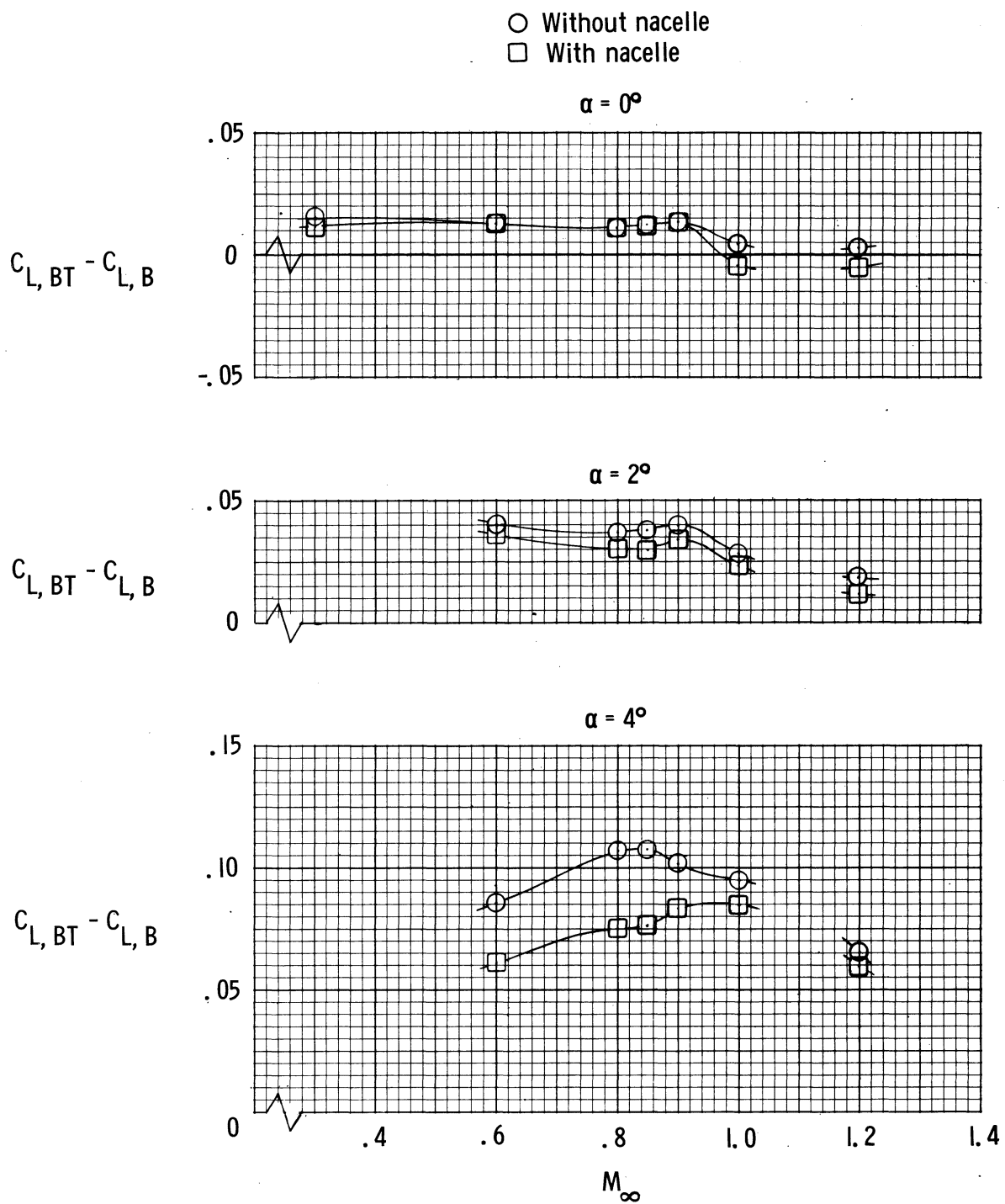
(e) Body with tails, flowthrough nacelle, flow fences.

Figure 6.- Concluded.



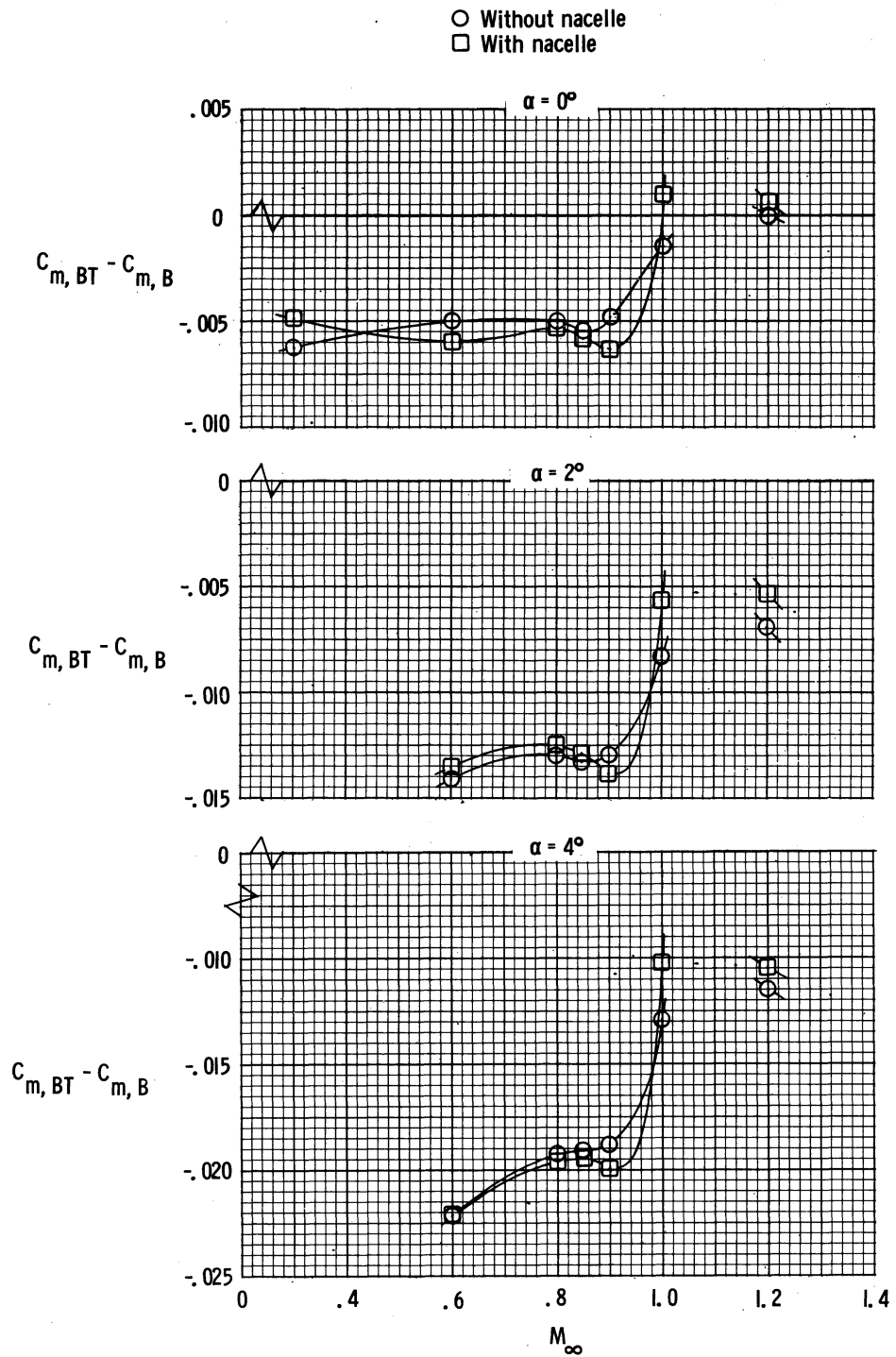
(a) Incremental drag coefficient.

Figure 7.- Incremental drag coefficients resulting from tails with and without flowthrough nacelle. No turbojet engines or flow fences.



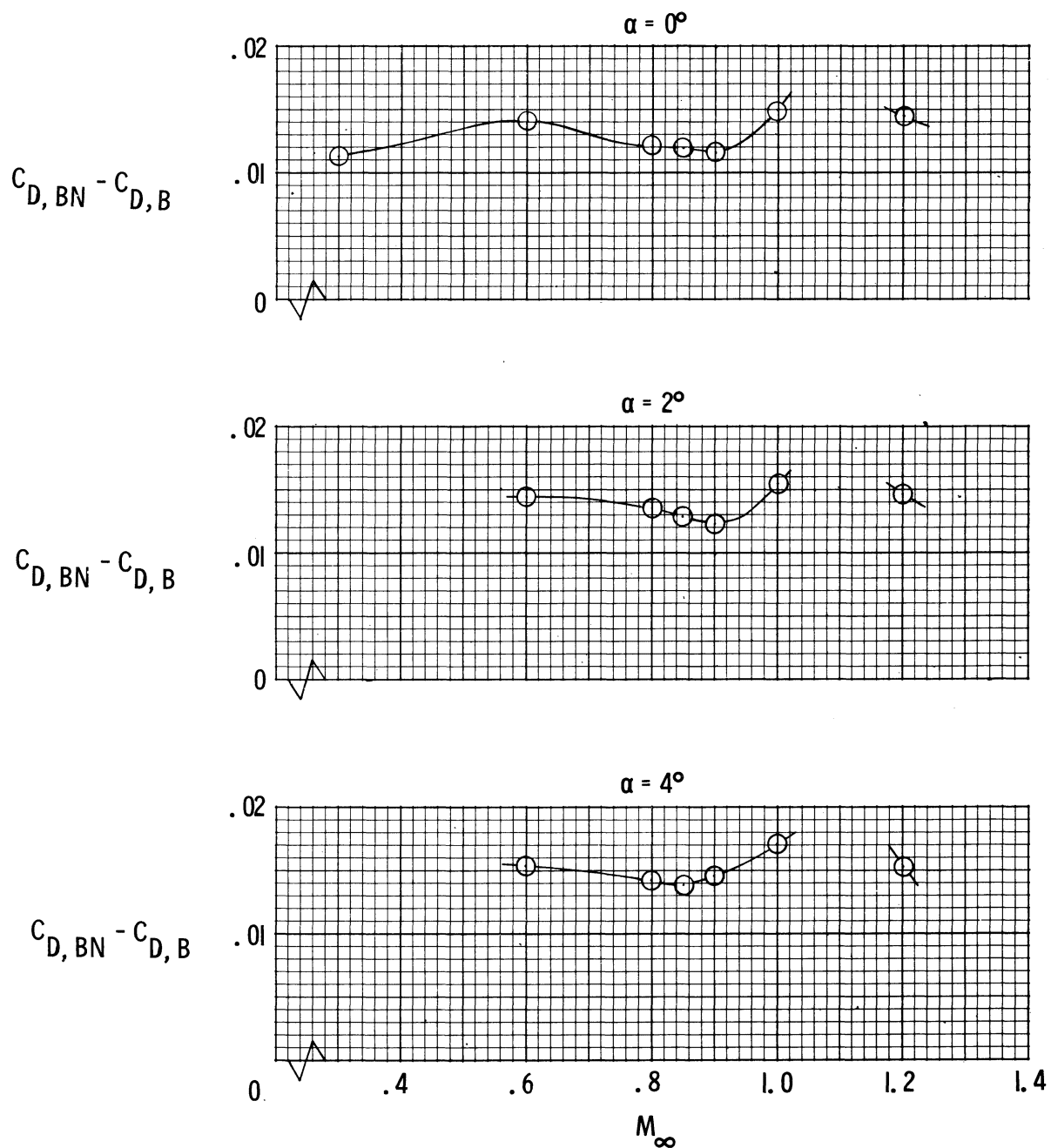
(b) Incremental lift coefficient.

Figure 7.- Continued.



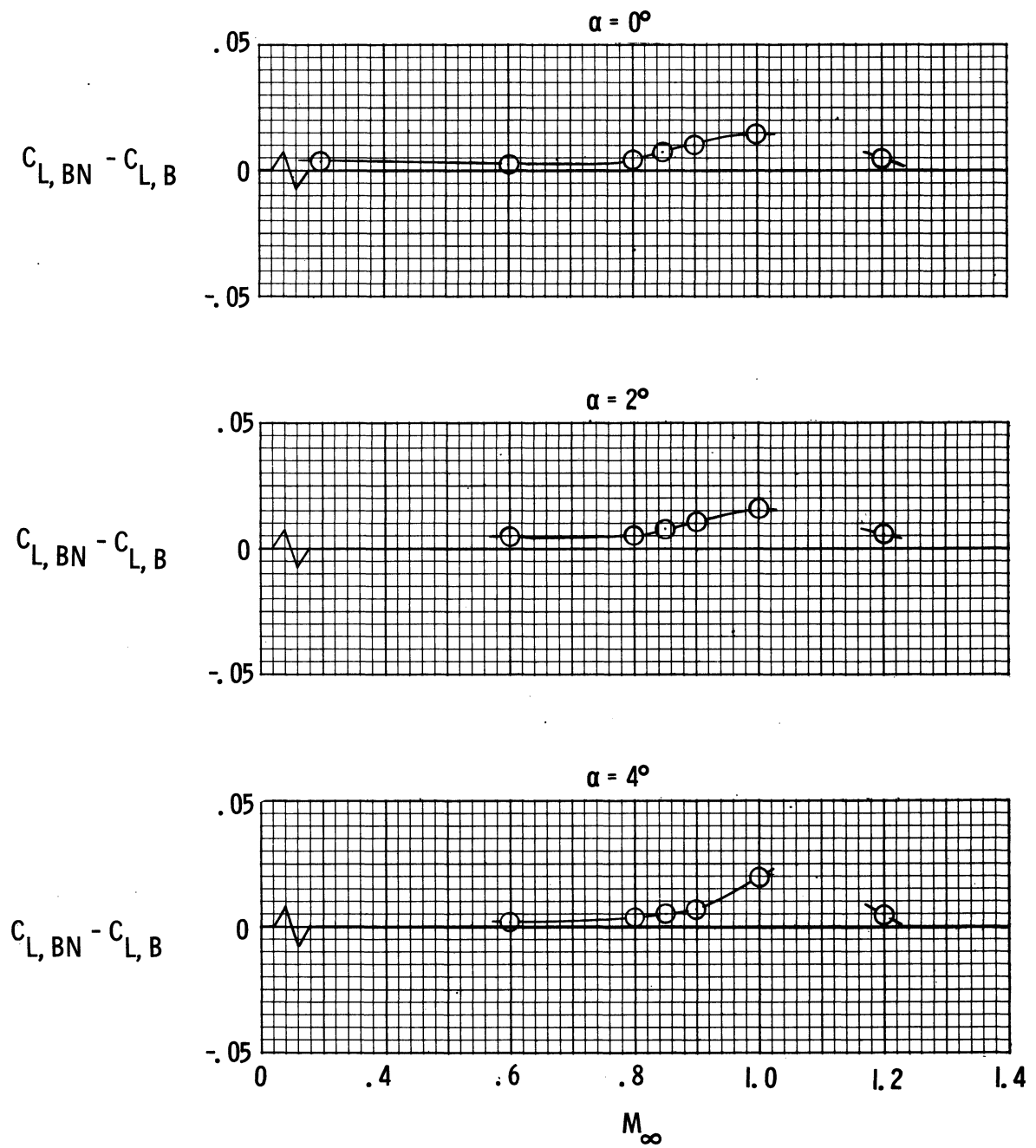
(c) Incremental pitching-moment coefficient.

Figure 7.- Concluded.



(a) Incremental drag coefficient.

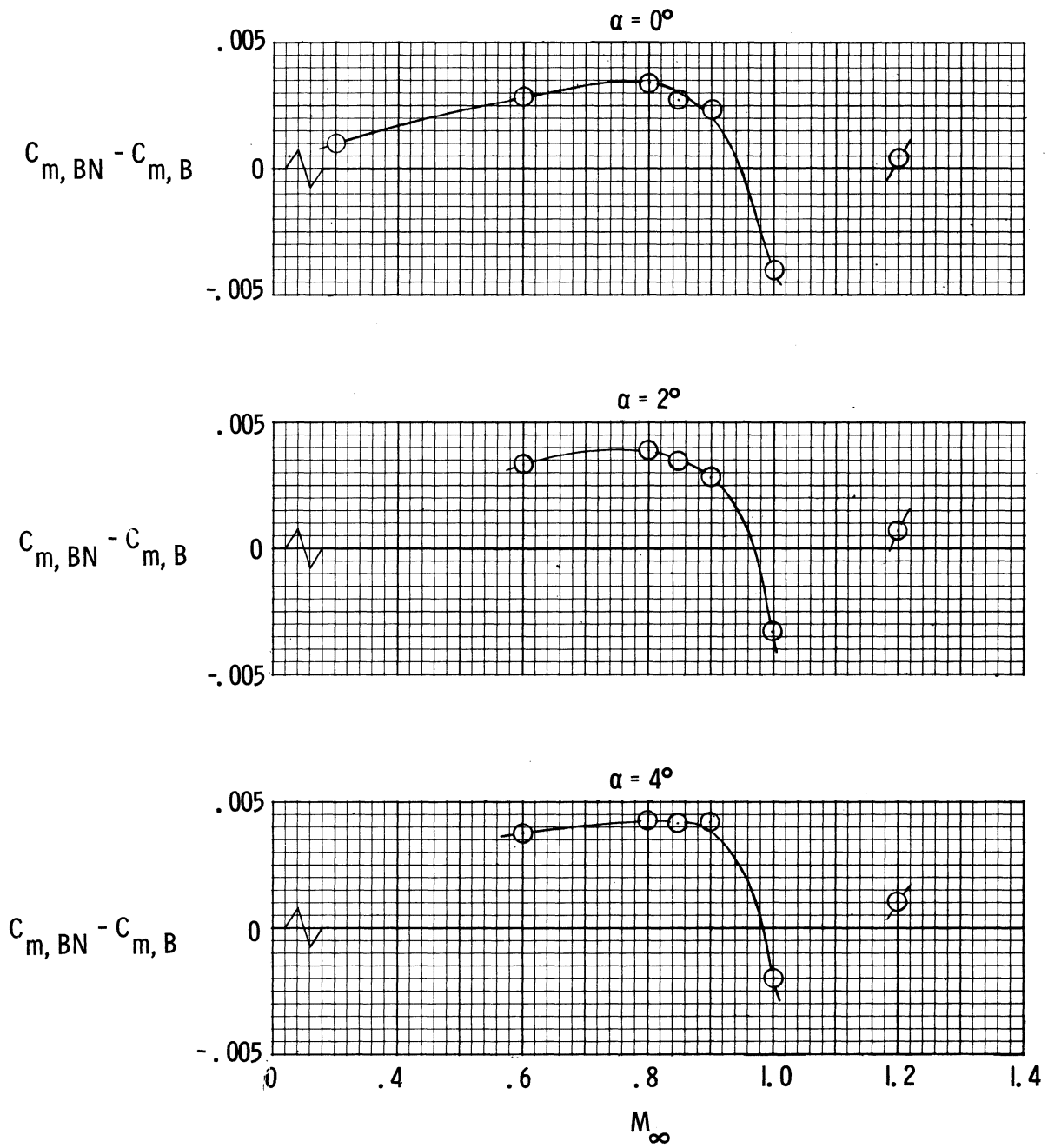
Figure 8.- Incremental aerodynamic coefficients resulting from flowthrough nacelle. No turbojet engines or tails.



(b) Incremental lift coefficient.

Figure 8.- Continued.





(c) Incremental pitching-moment coefficient.

Figure 8.- Concluded.

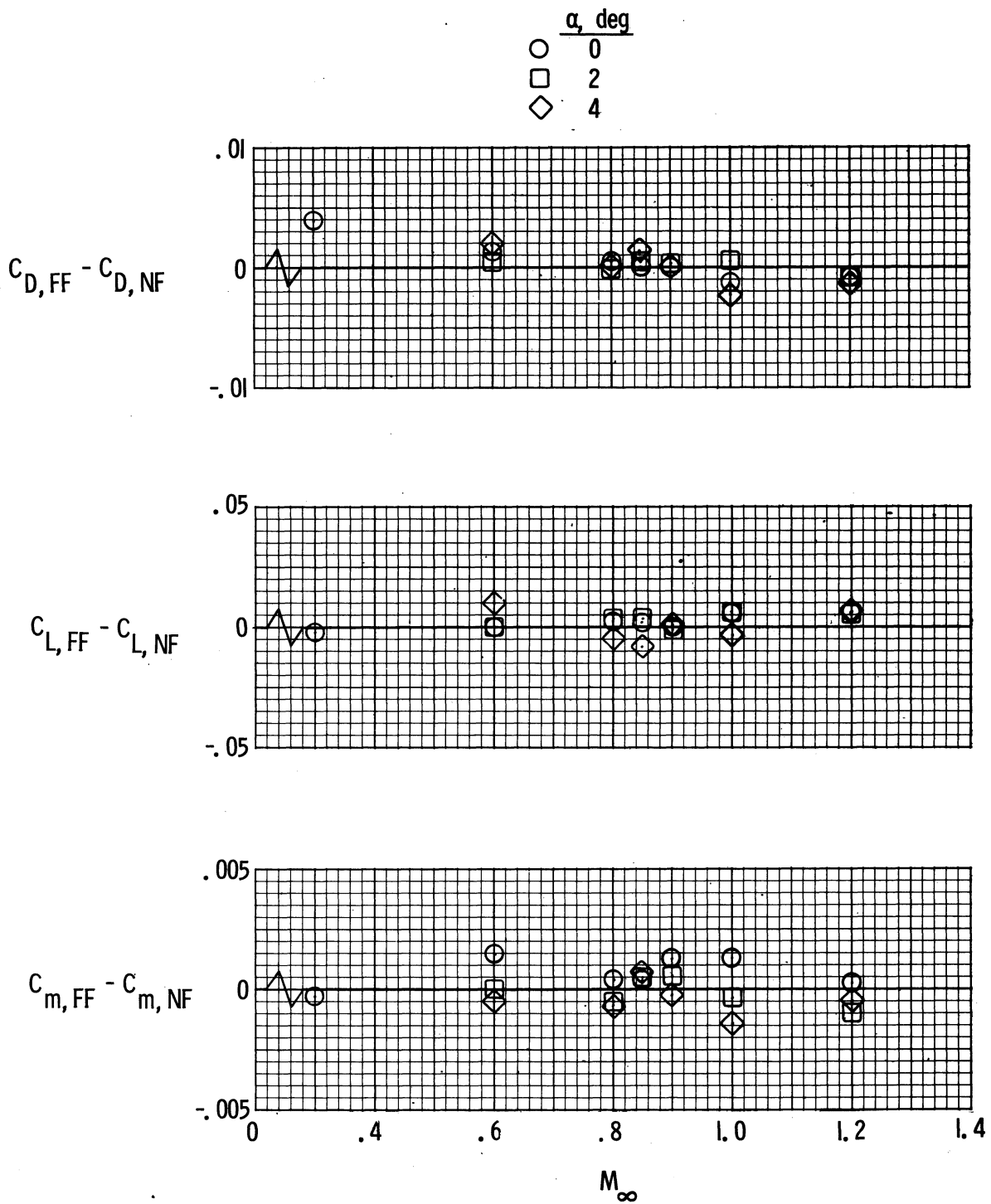


Figure 9.- Incremental aerodynamic coefficients resulting from flow fences. With tails and flowthrough nacelle. No turbojet engines.

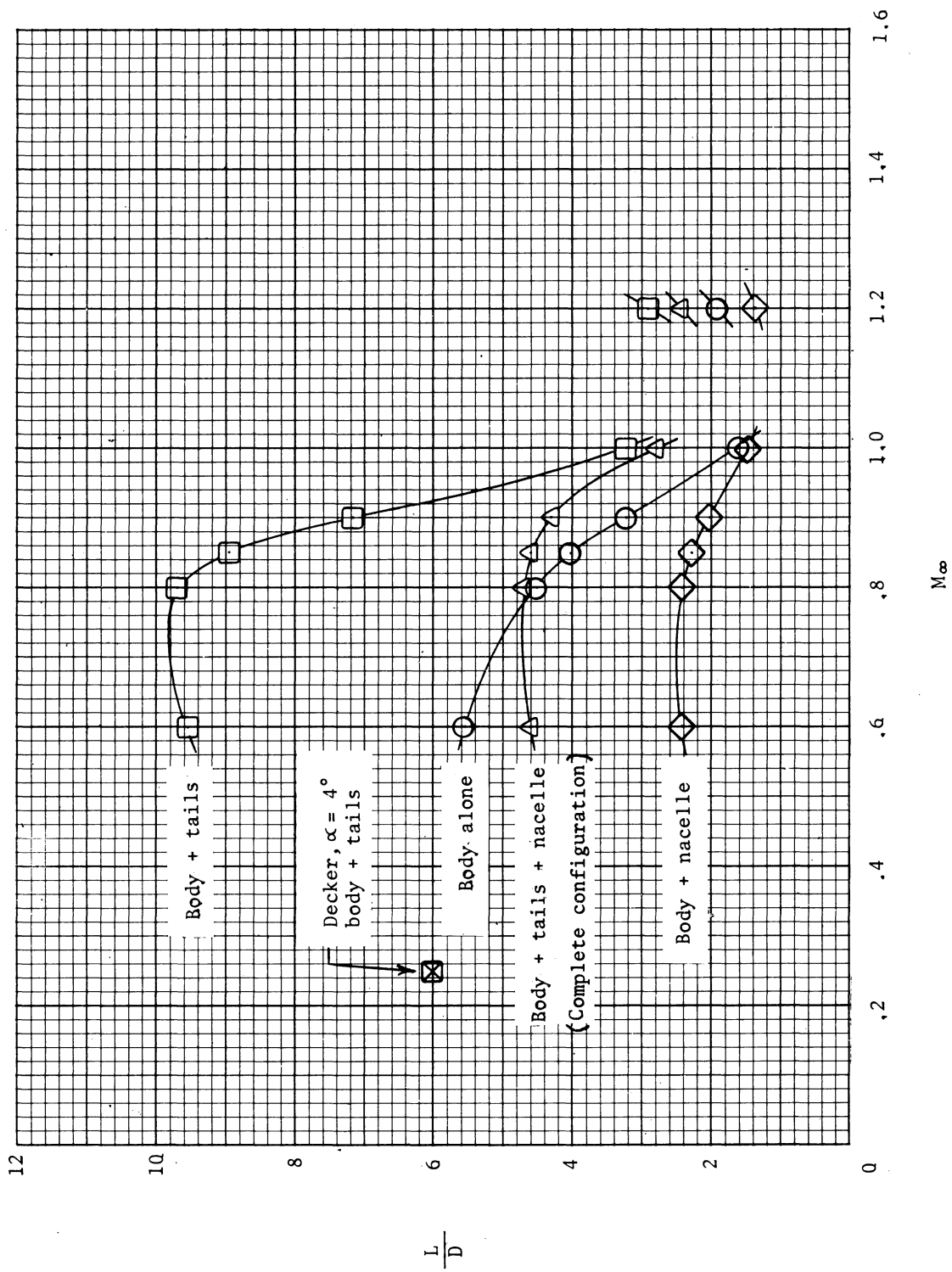
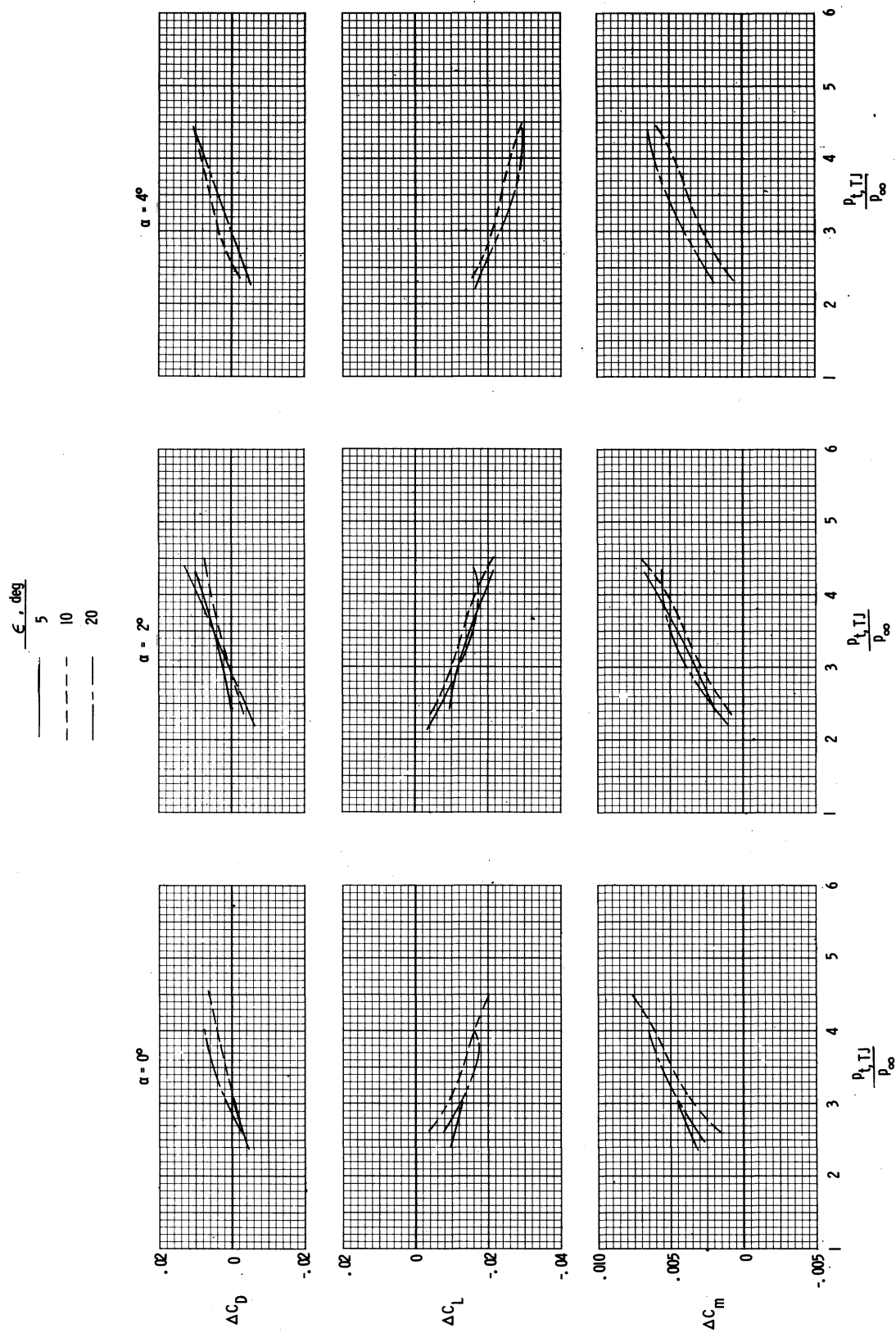
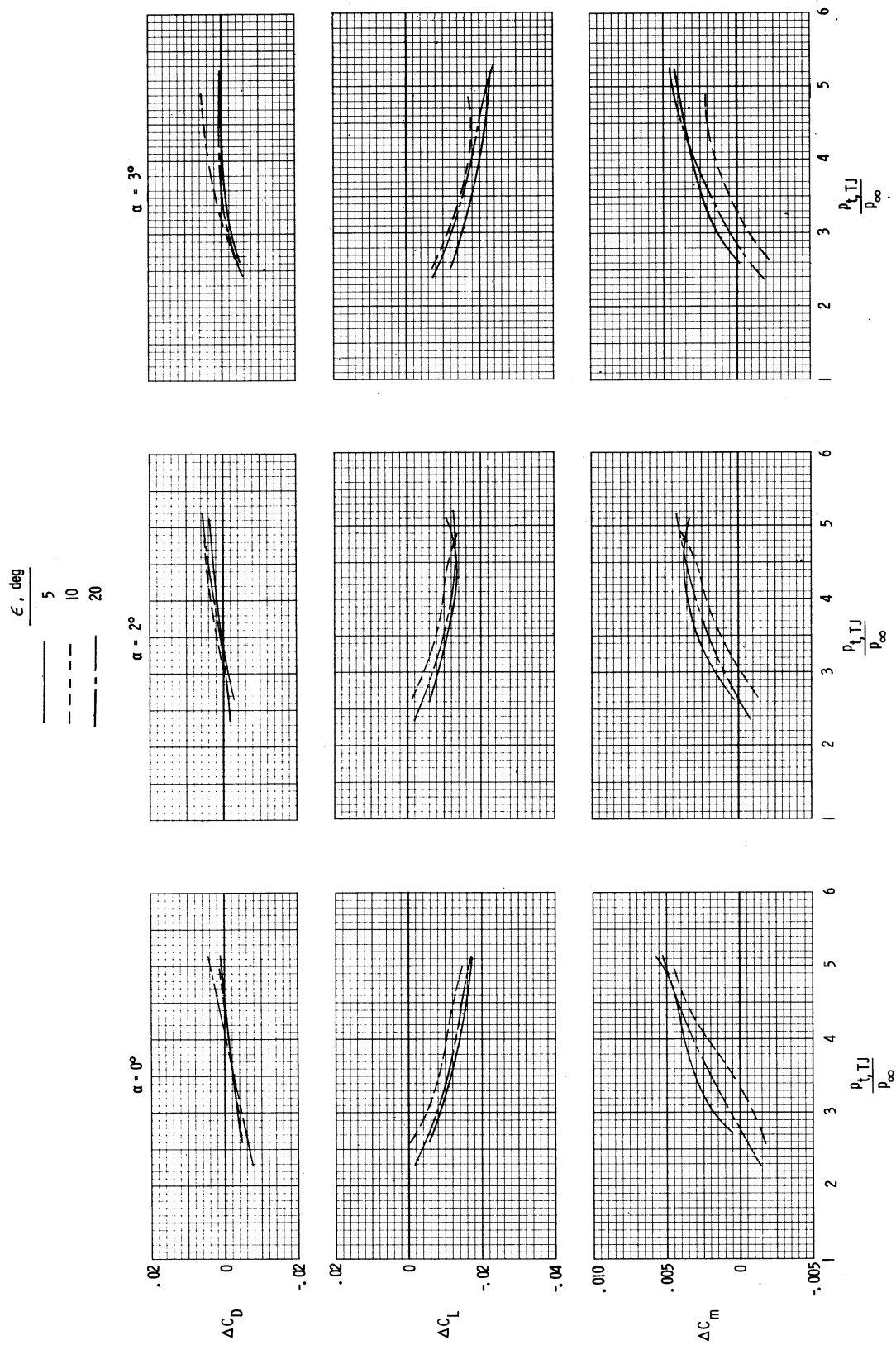


Figure 10.- Lift-drag ratio variation with Mach number at  $\alpha = 4^\circ$ . No turbojet engines.



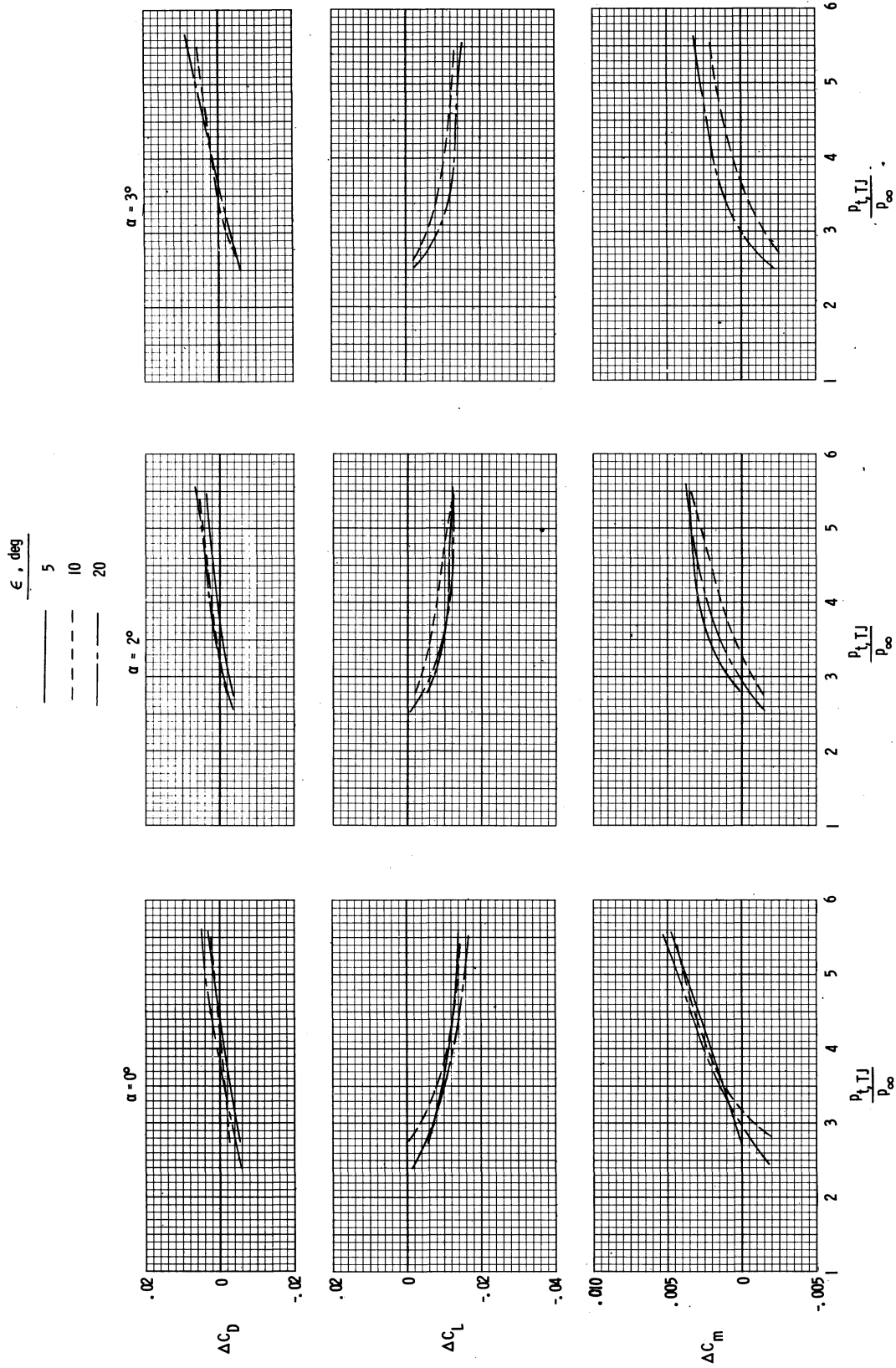
(a)  $M_\infty = 0.60$ .

Figure 11.- Effect of ramp angle on drag, lift, and pitching-moment coefficient increments. Flowthrough nacelle with flow fences.



(b)  $M_\infty = 0.80$ .

Figure 11.- Continued.



(c)  $M_\infty = 0.85$ .

Figure 11.- Concluded.

$\epsilon, \text{deg}$   
 — 5  
 - - 10  
 - - - 20

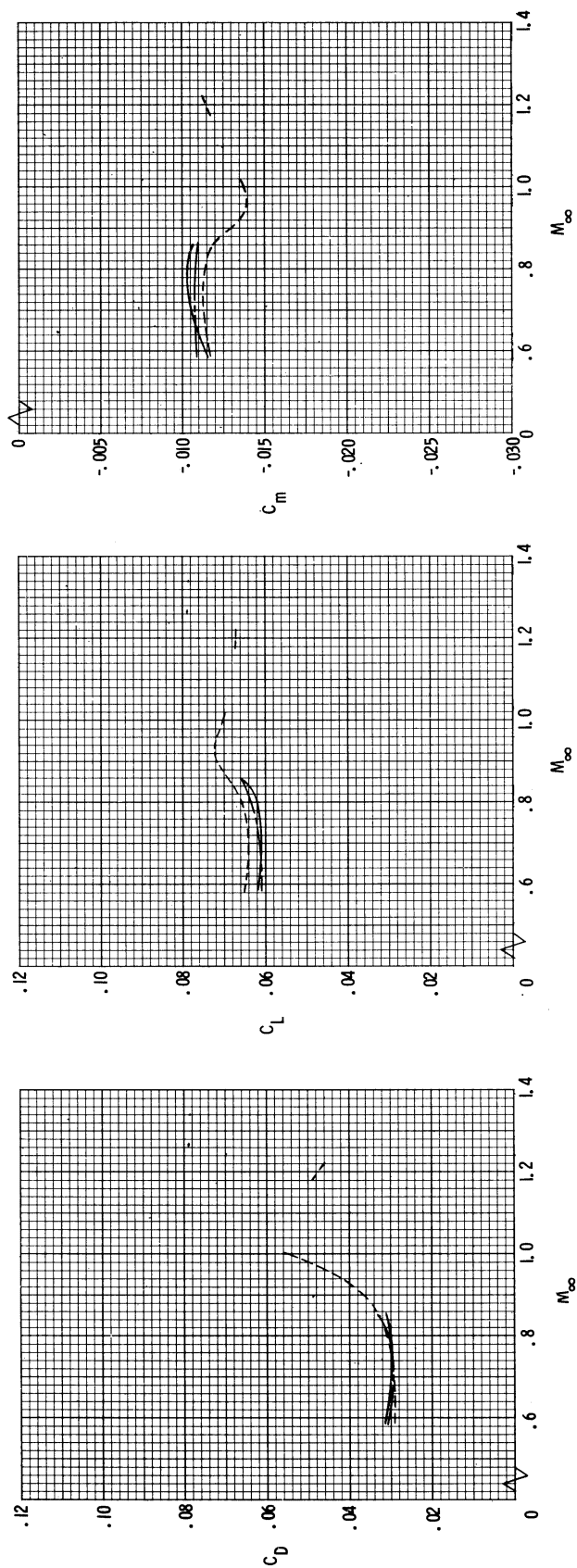


Figure 12.- Effect of ramp angle on aerodynamic coefficients as a function of Mach number for assumed jet pressure ratio schedule.  $\alpha = 20^\circ$ ; with flow fences; and flowthrough nacelle.

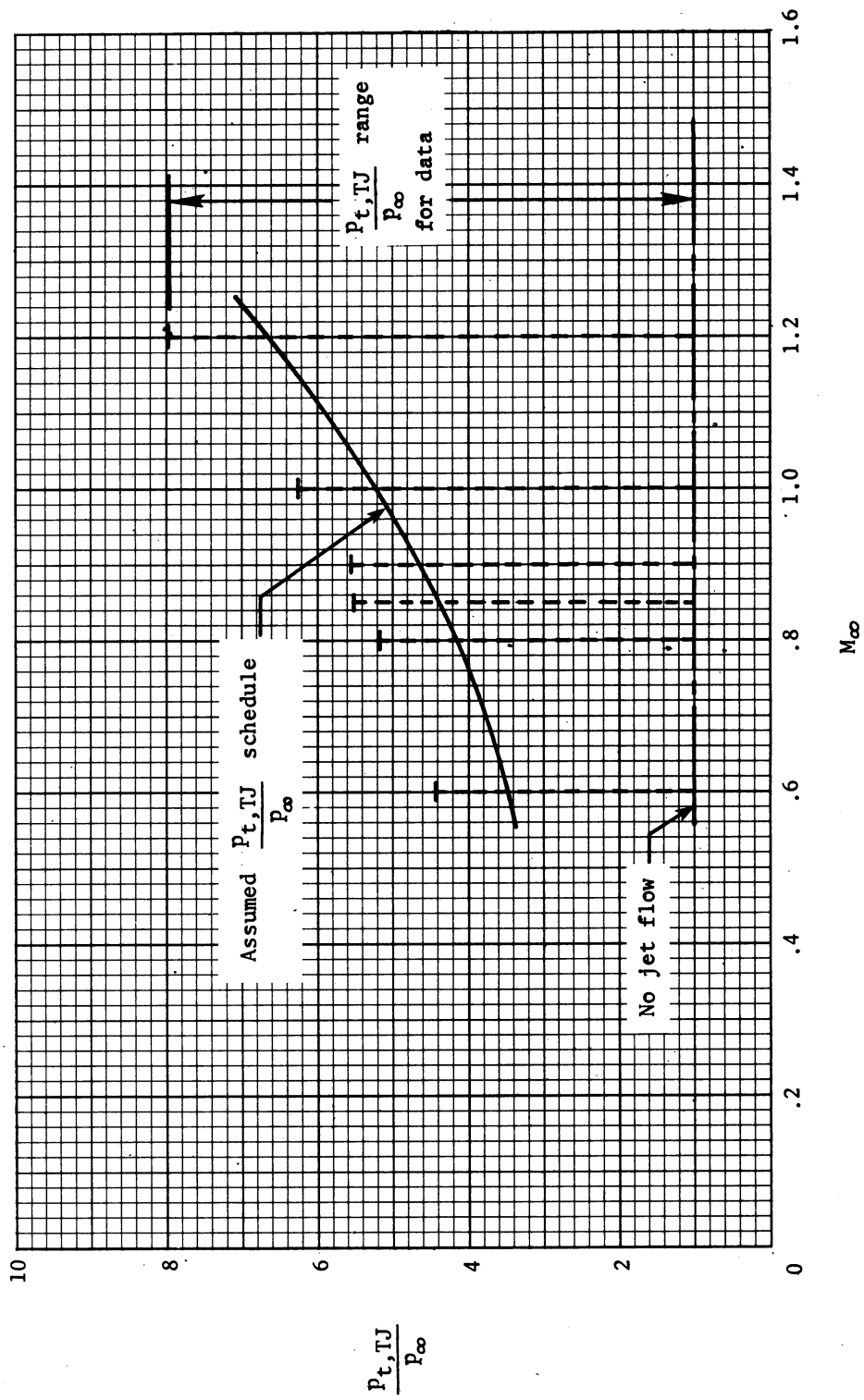
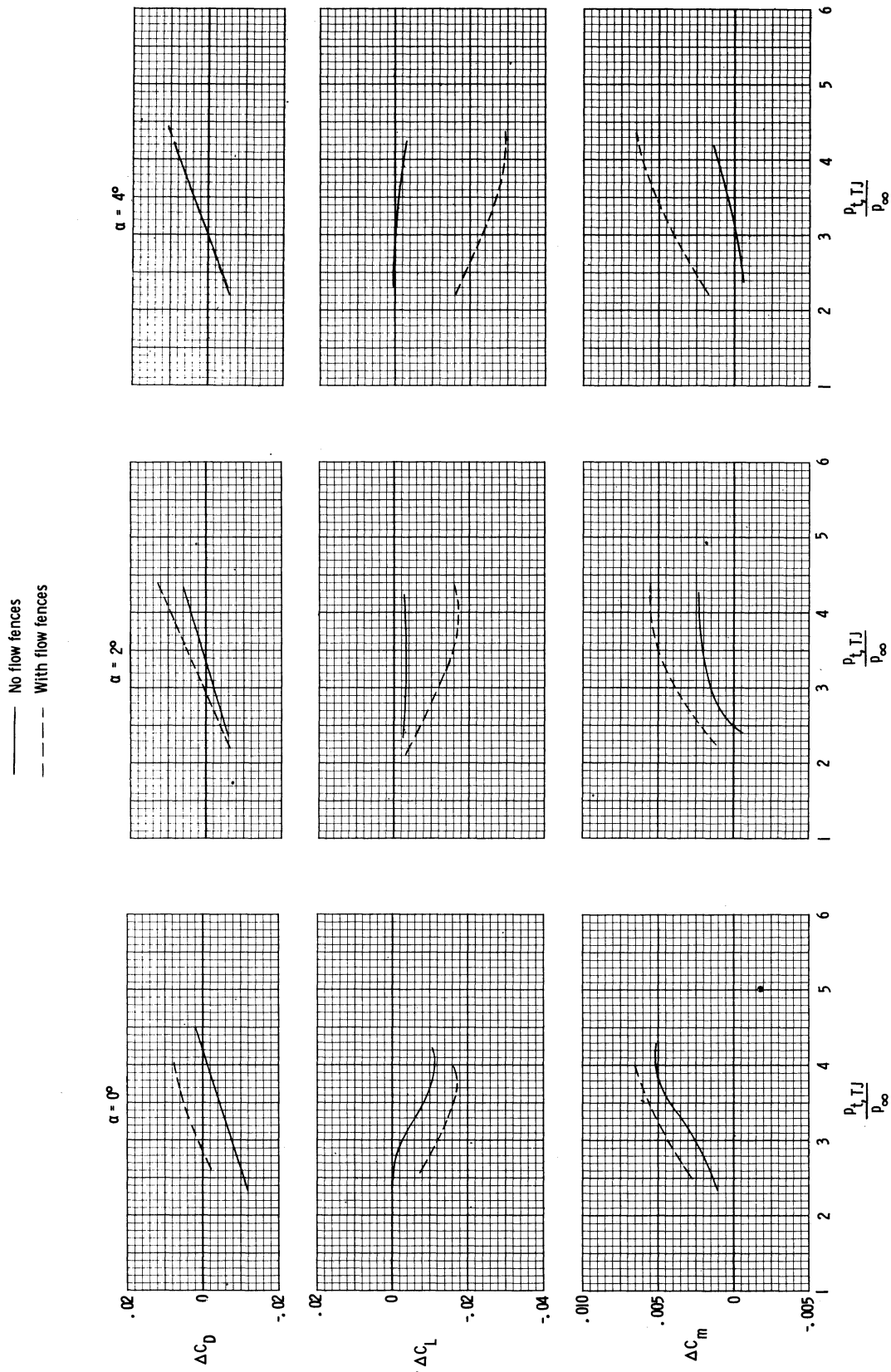


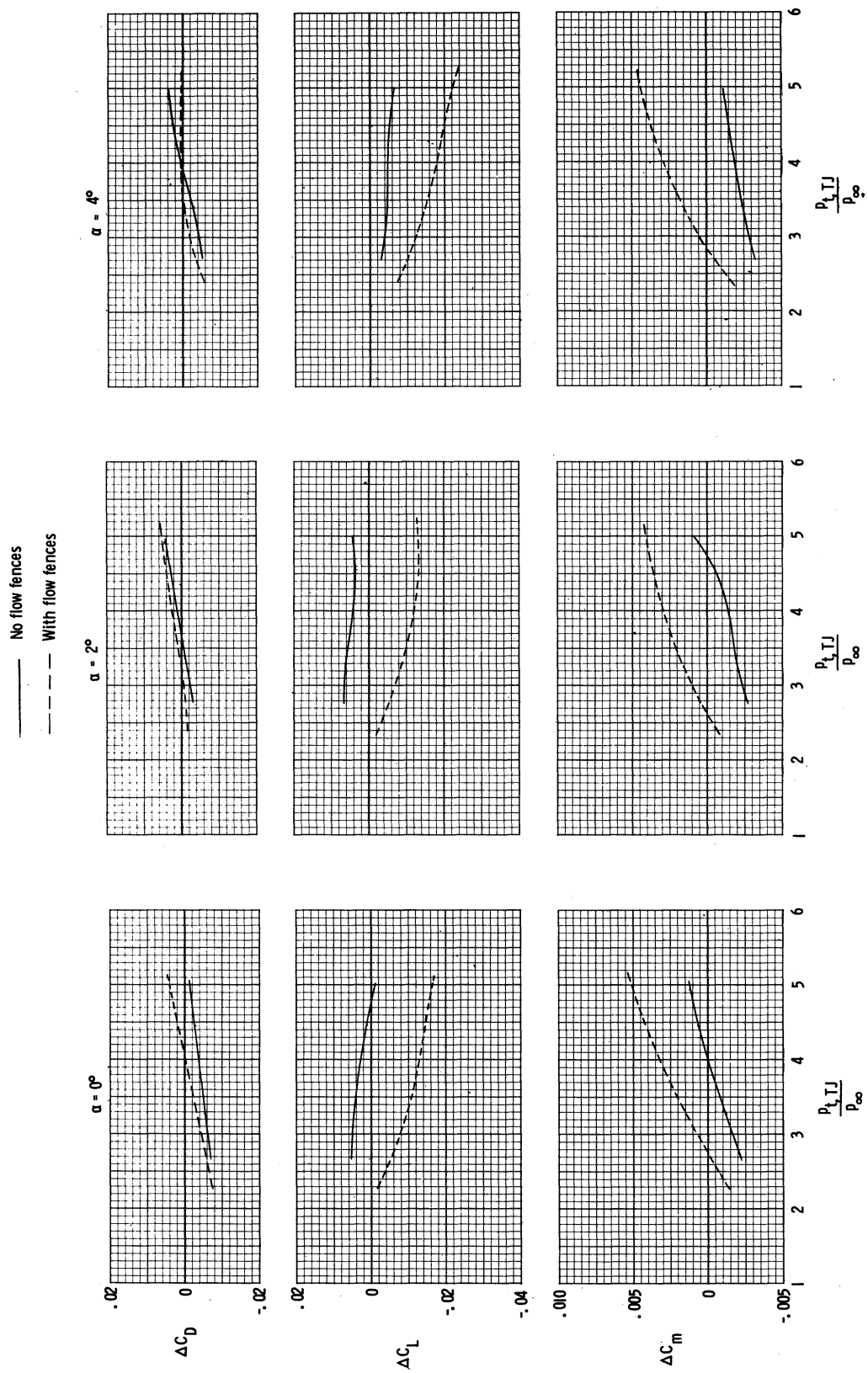
Figure 13.- Assumed turbojet pressure ratio schedule and test ranges.





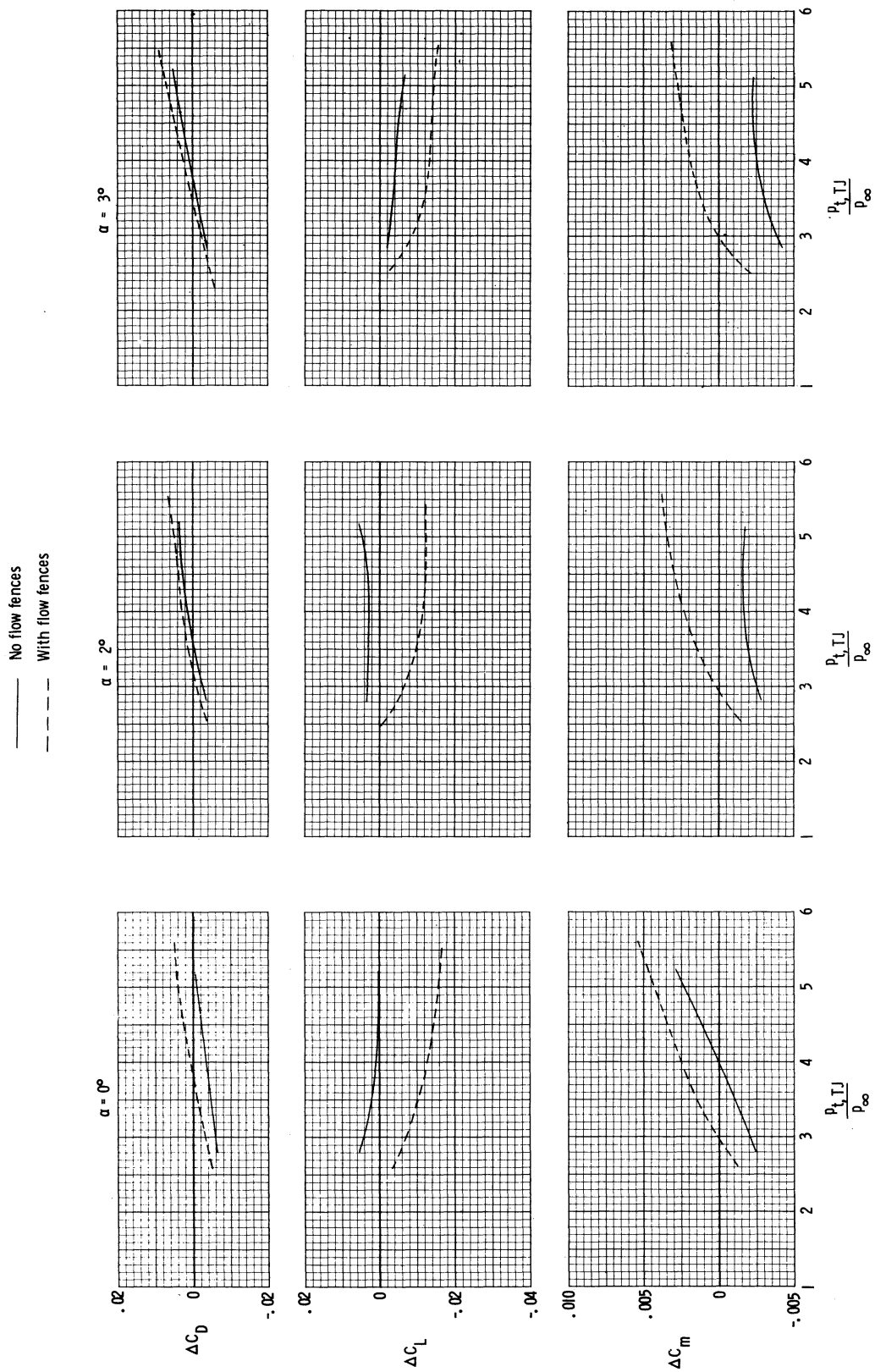
(a)  $M_{\infty} = 0.60$ .

Figure 14.- Effect of flow fences on drag, lift, and pitching-moment coefficient increments with flowthrough nacelle and  $\epsilon = 20^\circ$ . Increments referenced to configurations of figures 6(d) and 6(e).



(b)  $M_\infty = 0.80$ .

Figure 14.- Continued.



(c)  $M_\infty = 0.85$ .

Figure 14.- Concluded.

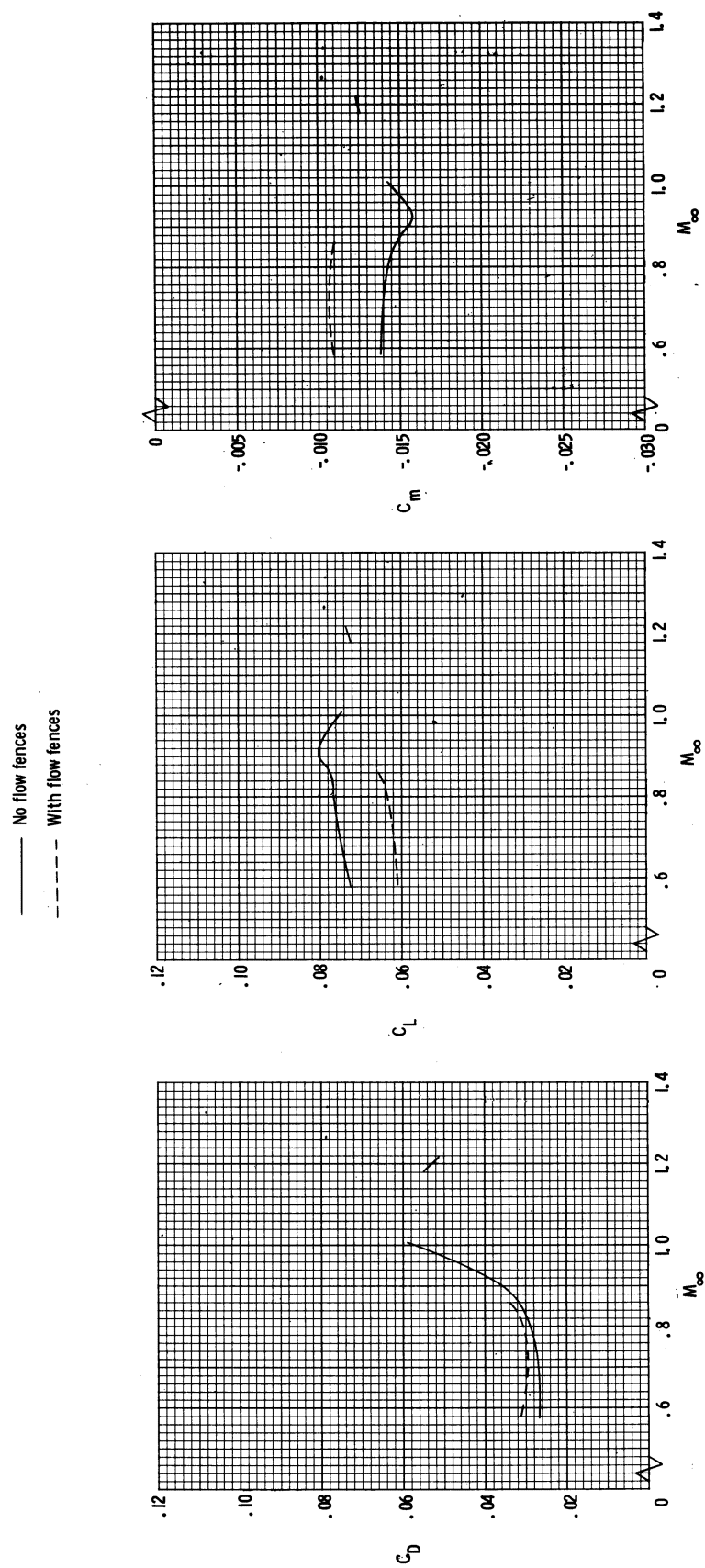
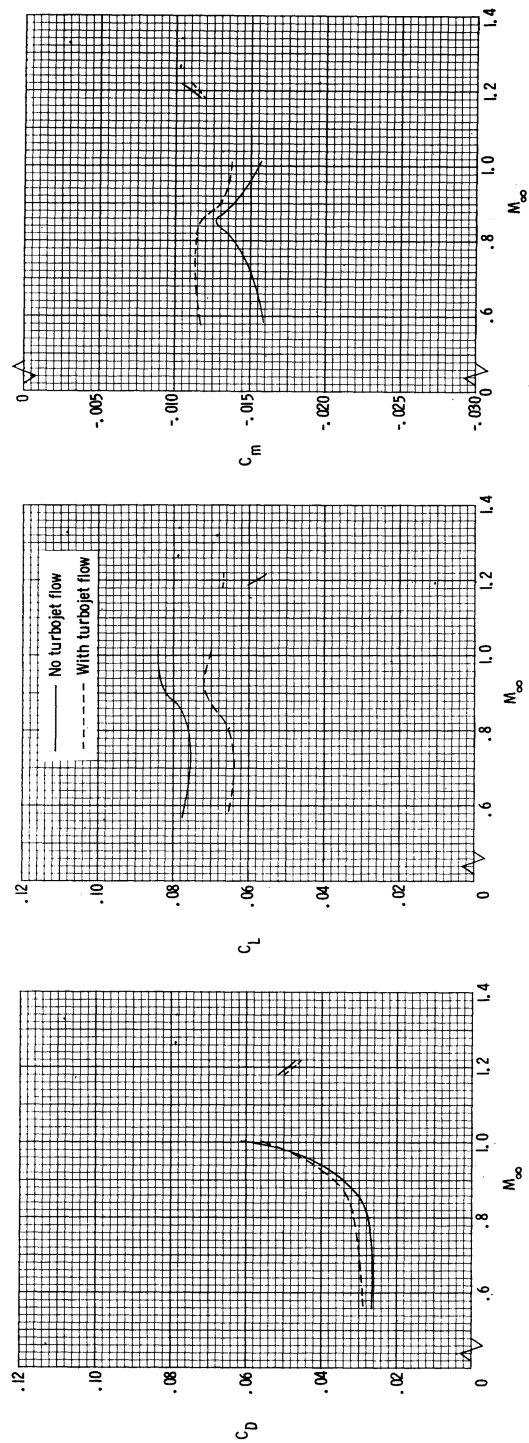
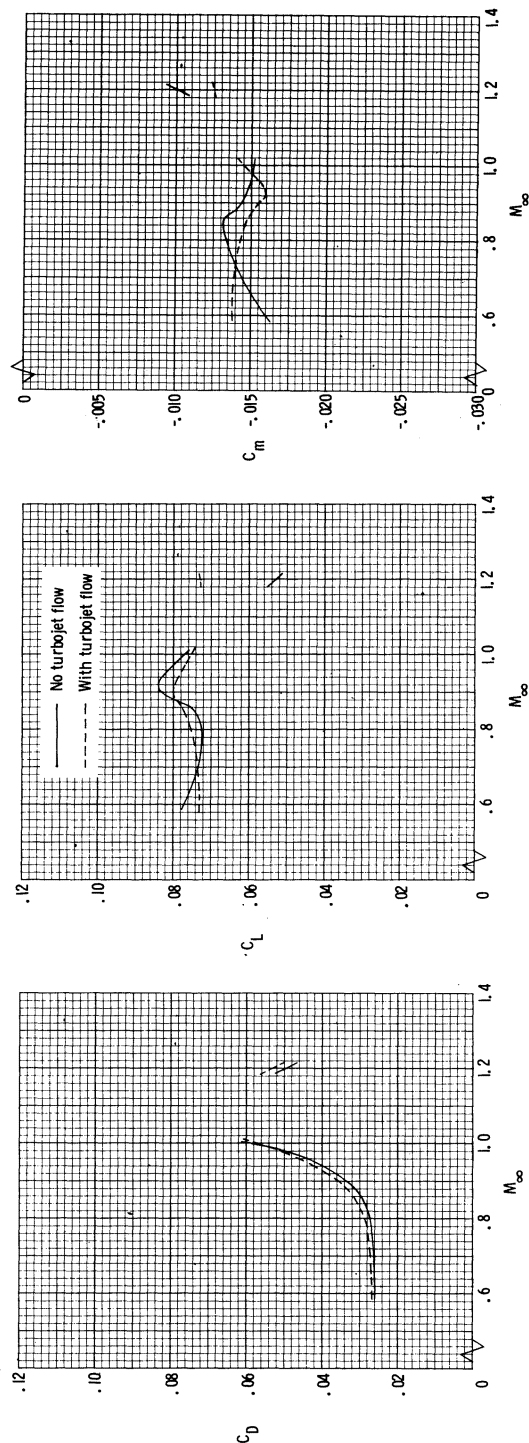


Figure 15.- Effect of flow fences on aerodynamic coefficients for assumed jet pressure ratio schedule.  
 $\alpha = 20^\circ$ ;  $\epsilon = 20^\circ$ ; flowthrough nacelle.



(a)  $\epsilon = 10^\circ$ , with flow fences.



(b)  $\epsilon = 20^\circ$ , no flow fences.

Figure 16.- Effect of turbojet operation on aerodynamic coefficients for assumed jet pressure ratio schedule. Flowthrough nacelle and  $\alpha = 20^\circ$ .

- $\epsilon = 10^\circ$  with fences
- - -  $\epsilon = 20^\circ$  no fences
- · - · - No turbojet engines

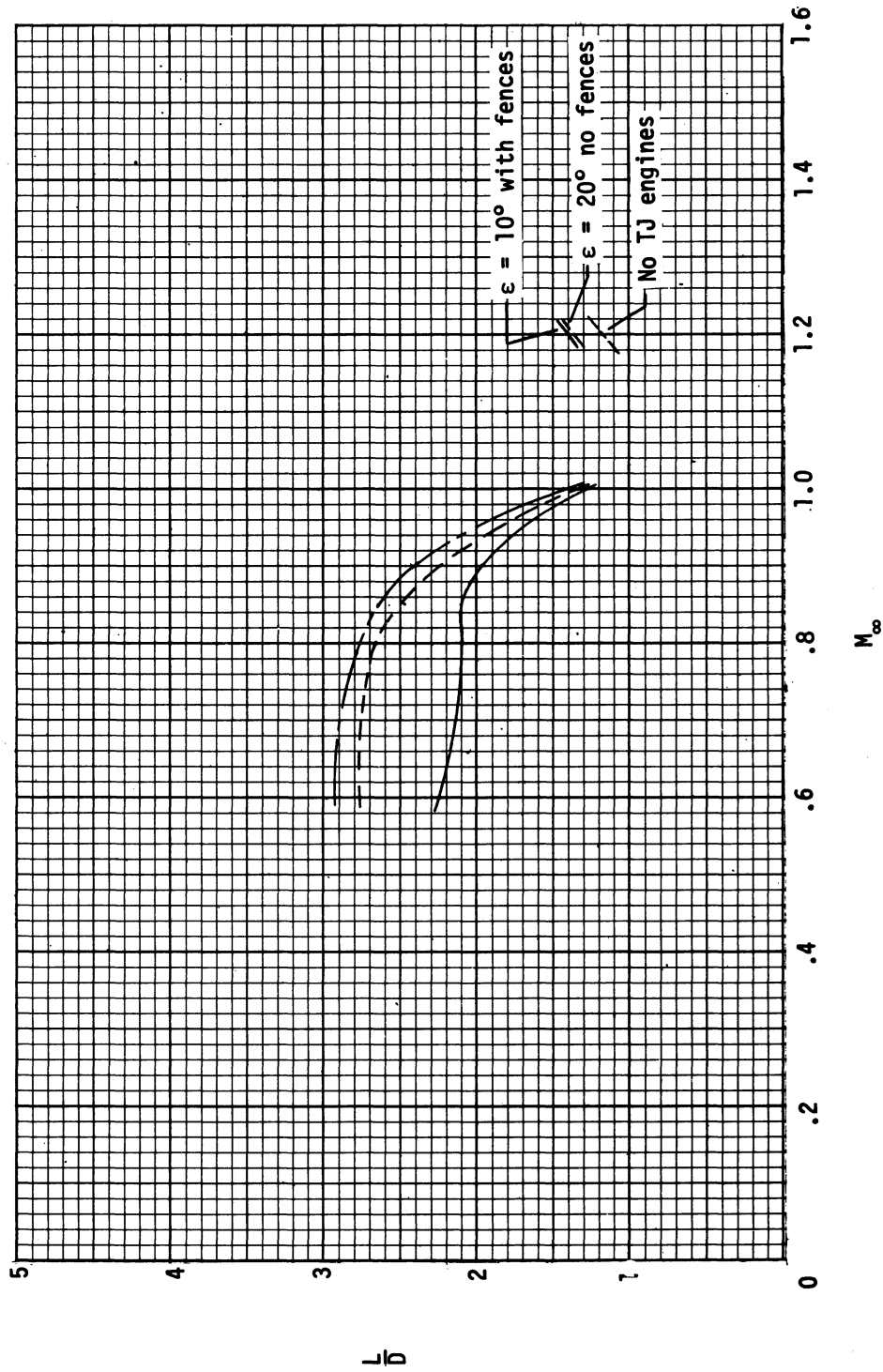


Figure 17.- Variation of  $L/D$  with Mach number for three configurations. Assumed jet pressure ratio schedule;  $\alpha = 2^\circ$ ; flowthrough nacelle.

$M_\infty$	$\frac{\bar{p}_{t,SJ}}{p_\infty}$
.6	1.71
.8	1.85
.85	1.85

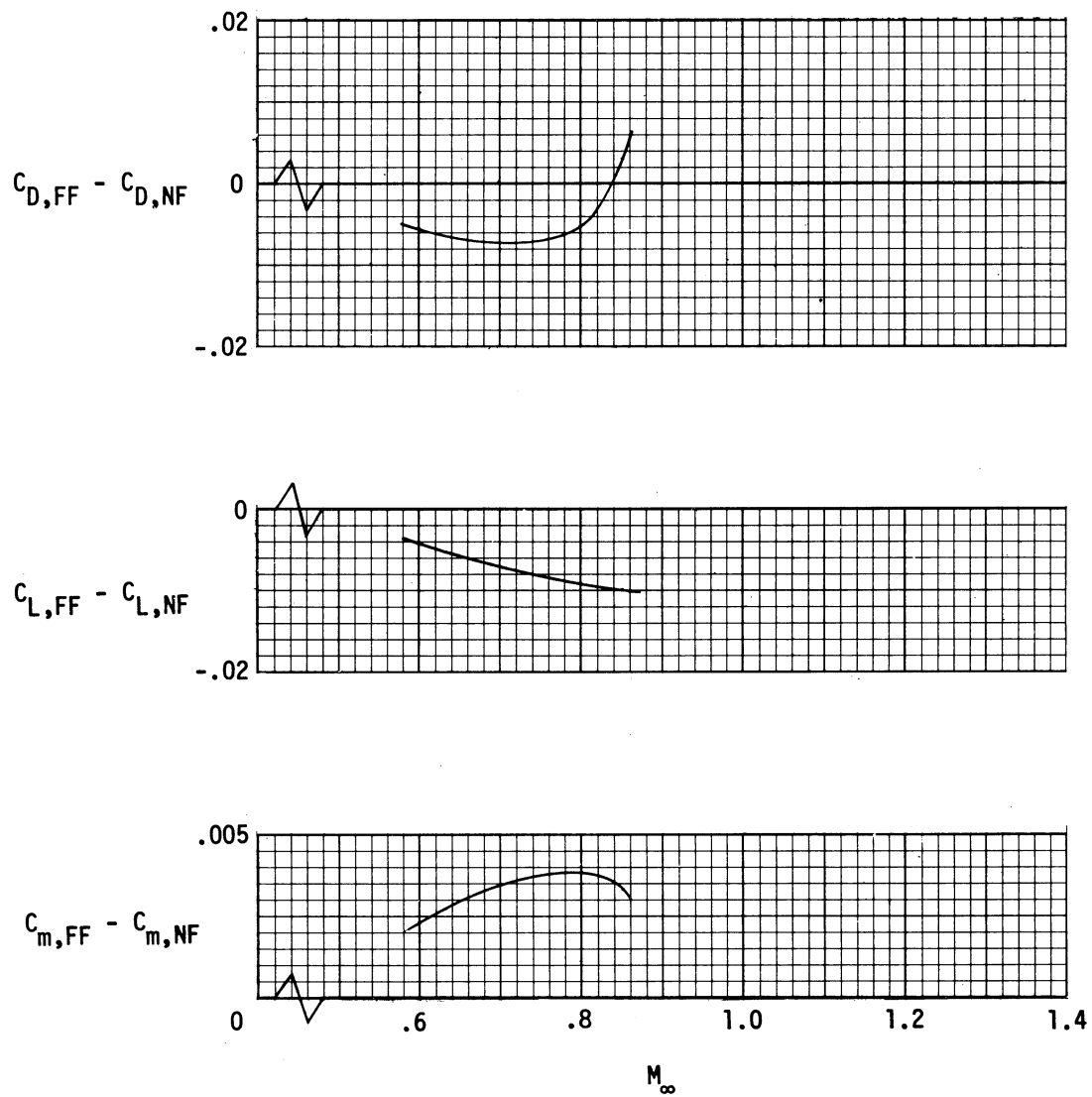


Figure 18.- Incremental drag, lift, and pitching-moment coefficients resulting from flow fences. Assumed turbojet pressure ratio schedule,  $\alpha = 0^\circ$ ,  $H_2O_2$  scramjet nacelle.

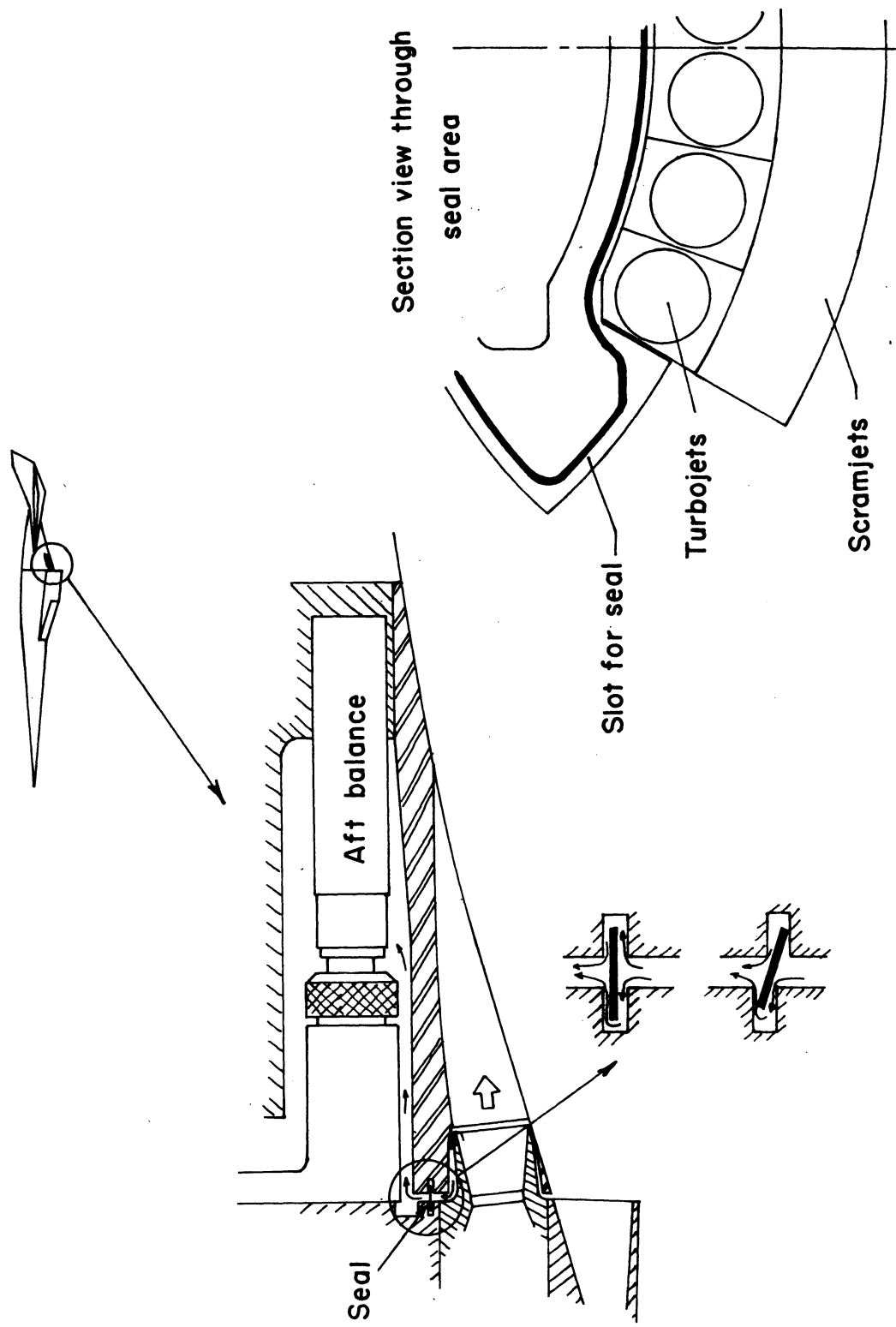


Figure 19.- Drawings illustrating afterbody seal leakage as source for aft balance heating.



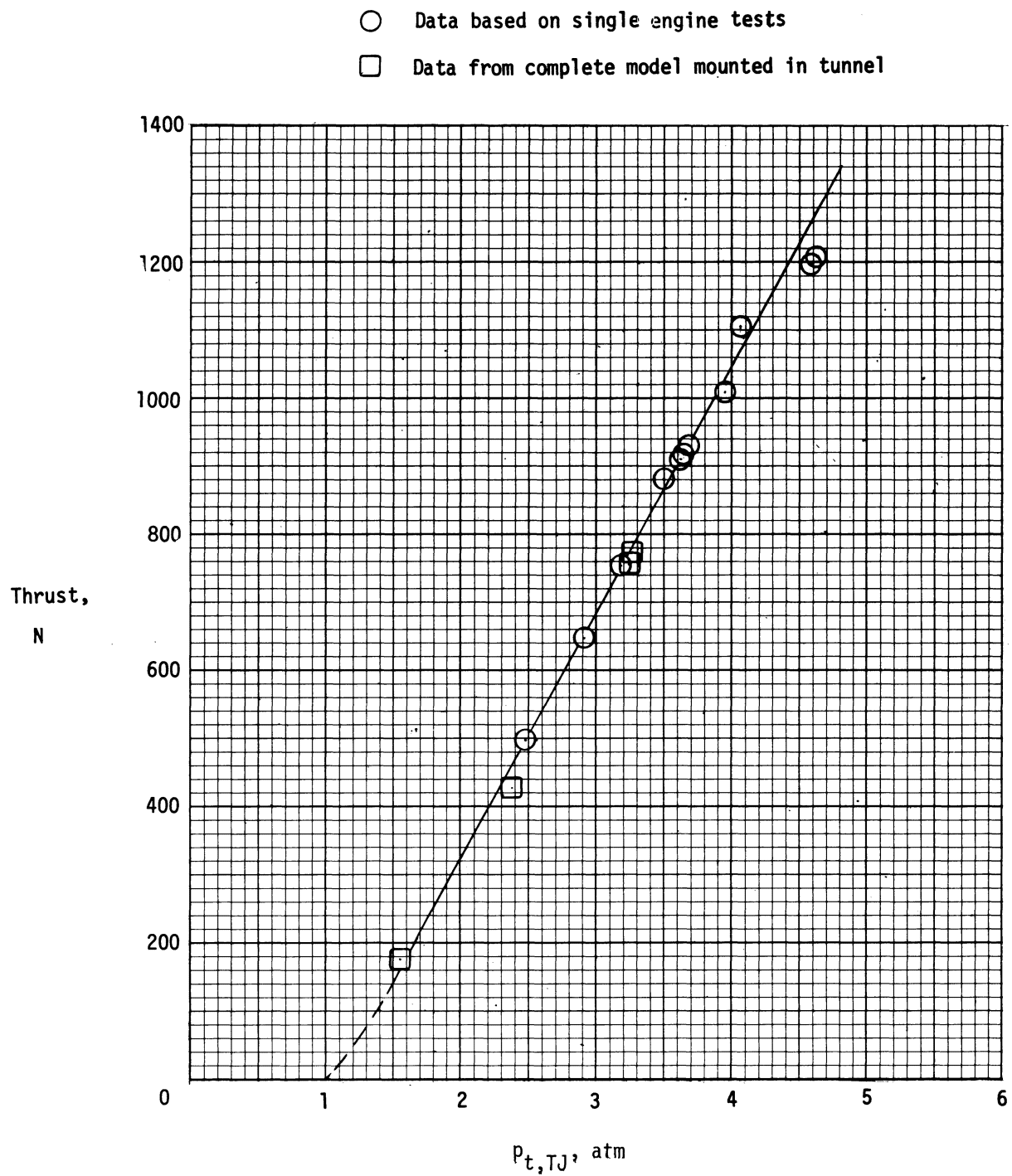
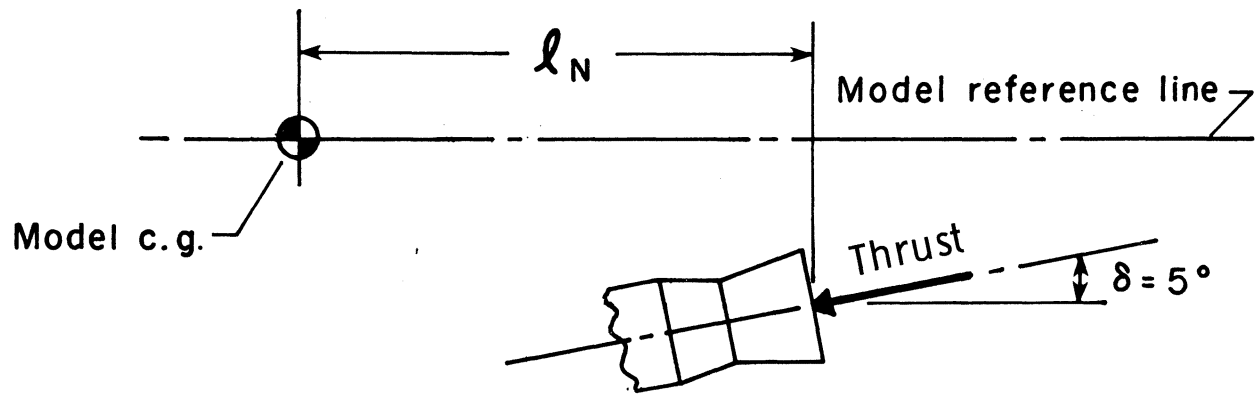
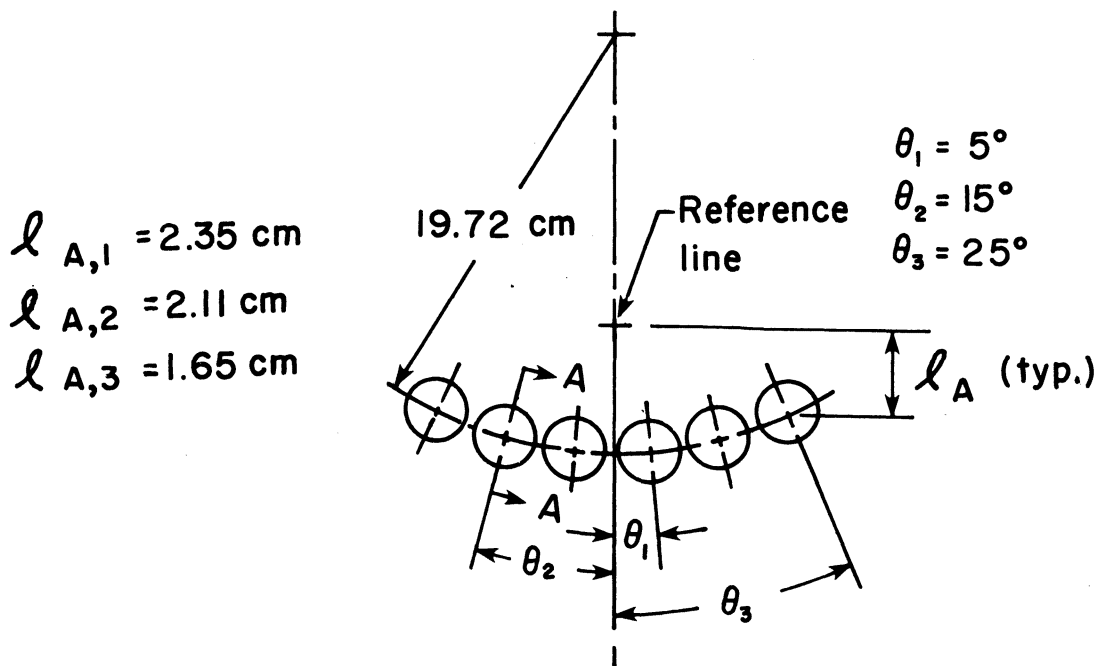


Figure 20.- Total turbojet thrust (six engines) as a function of  $p_{t,TJ}$ . Static conditions.



View A - A (typical)

$$l_N = 13.84 \text{ cm}$$



Rear view

Figure 21.- Geometry for thrust component calculation.

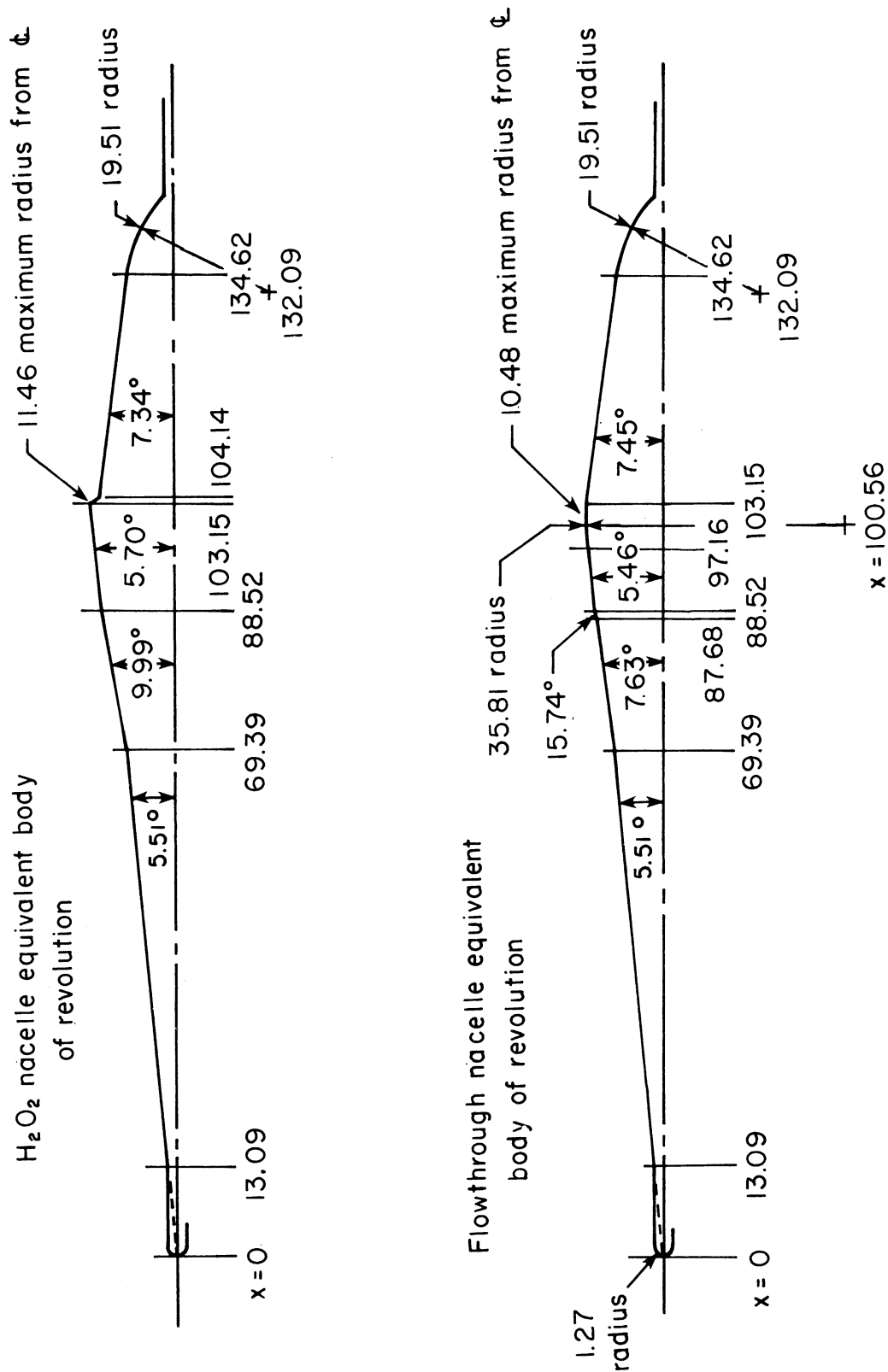
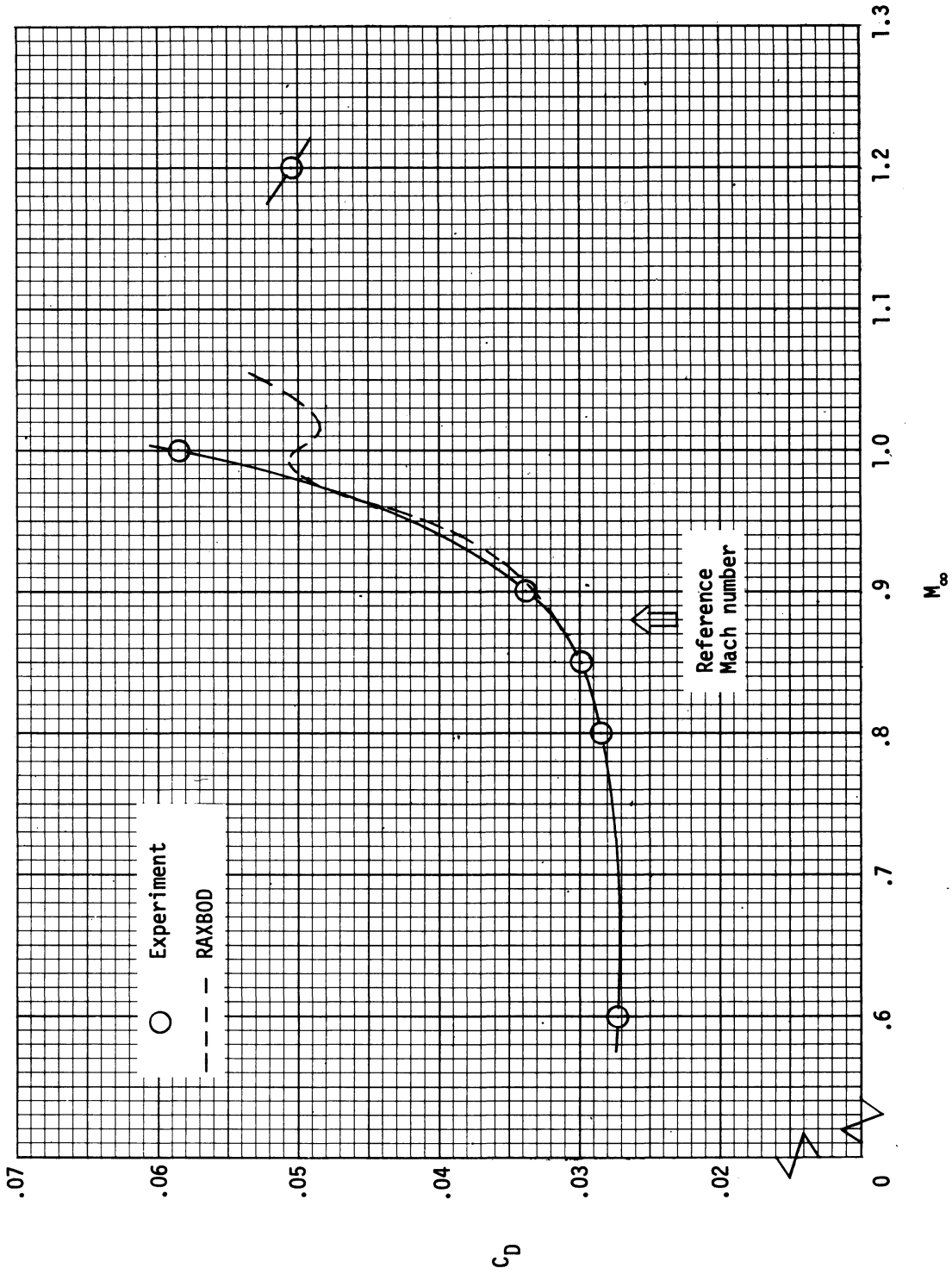
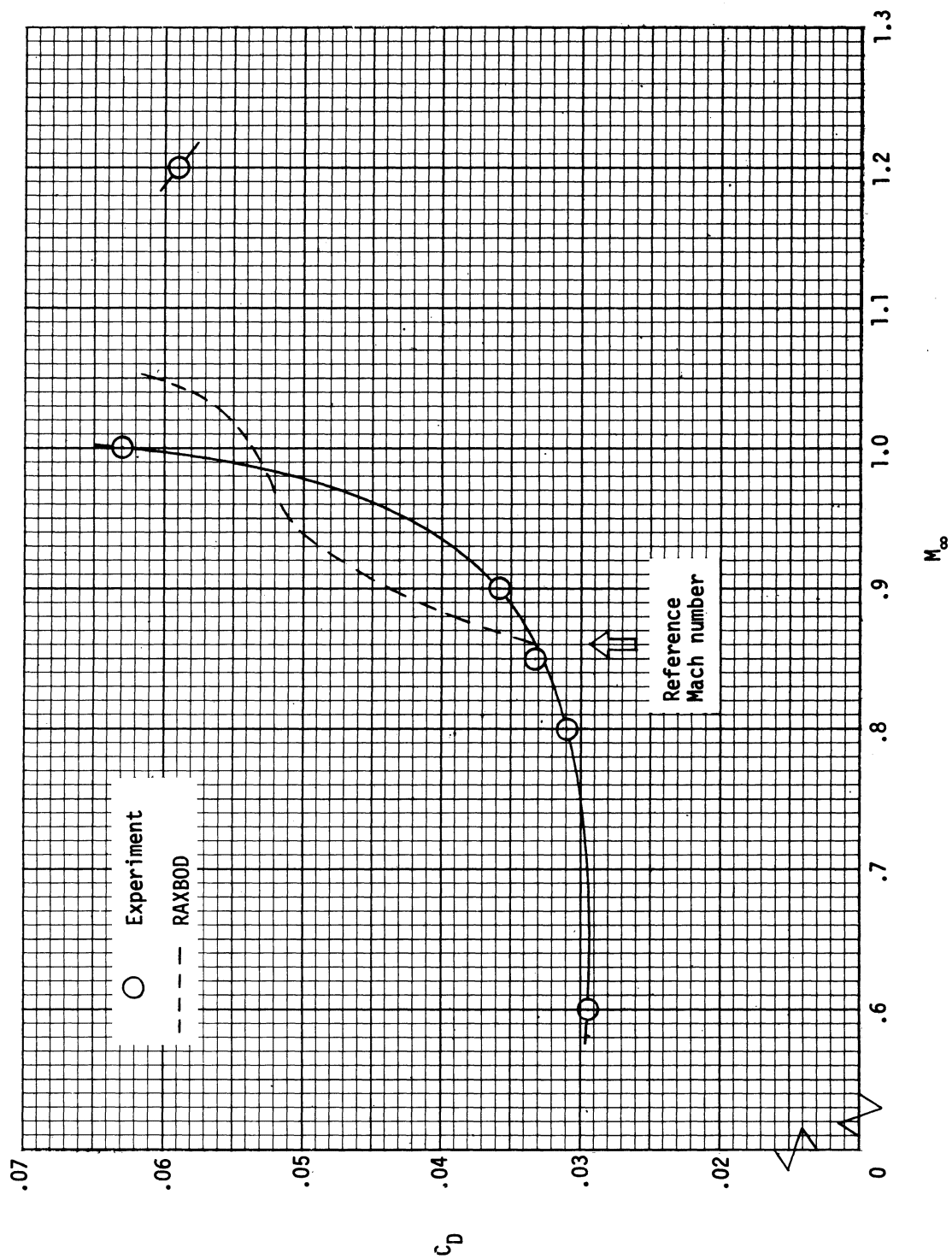


Figure 22.- Equivalent bodies of revolution for two ABLV model configurations without flow fences used for geometry input for RAXBOD code. All dimensions are in centimeters.



(a) Flowthrough nacelle configuration.

Figure 23.- Comparison between experimental and calculated drag coefficients.  
 $\alpha = 0^\circ$ ; no turbojet or scramjet exhaust flow.



(b)  $H_2O_2$  nacelle configuration.

Figure 23.- Concluded.

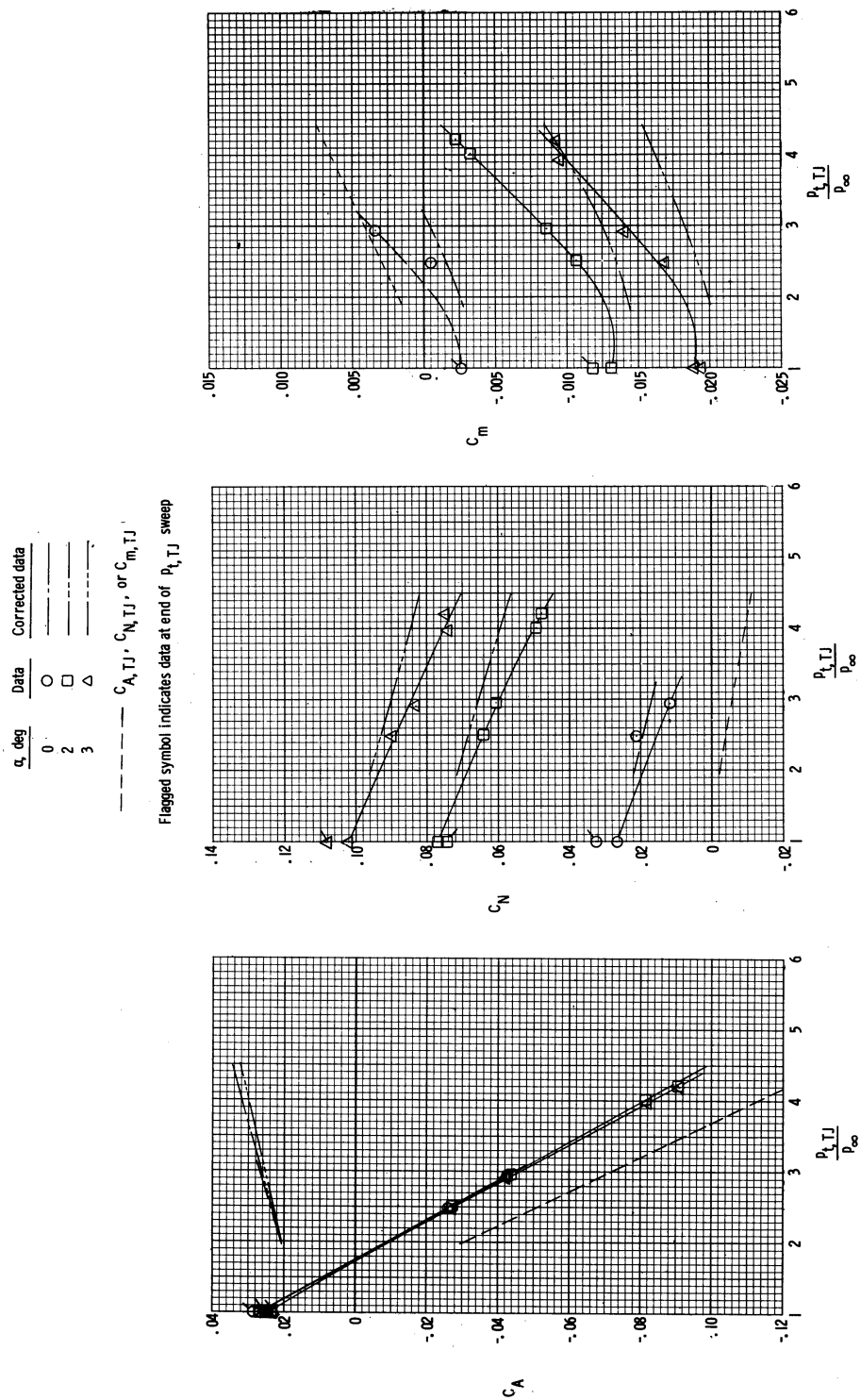
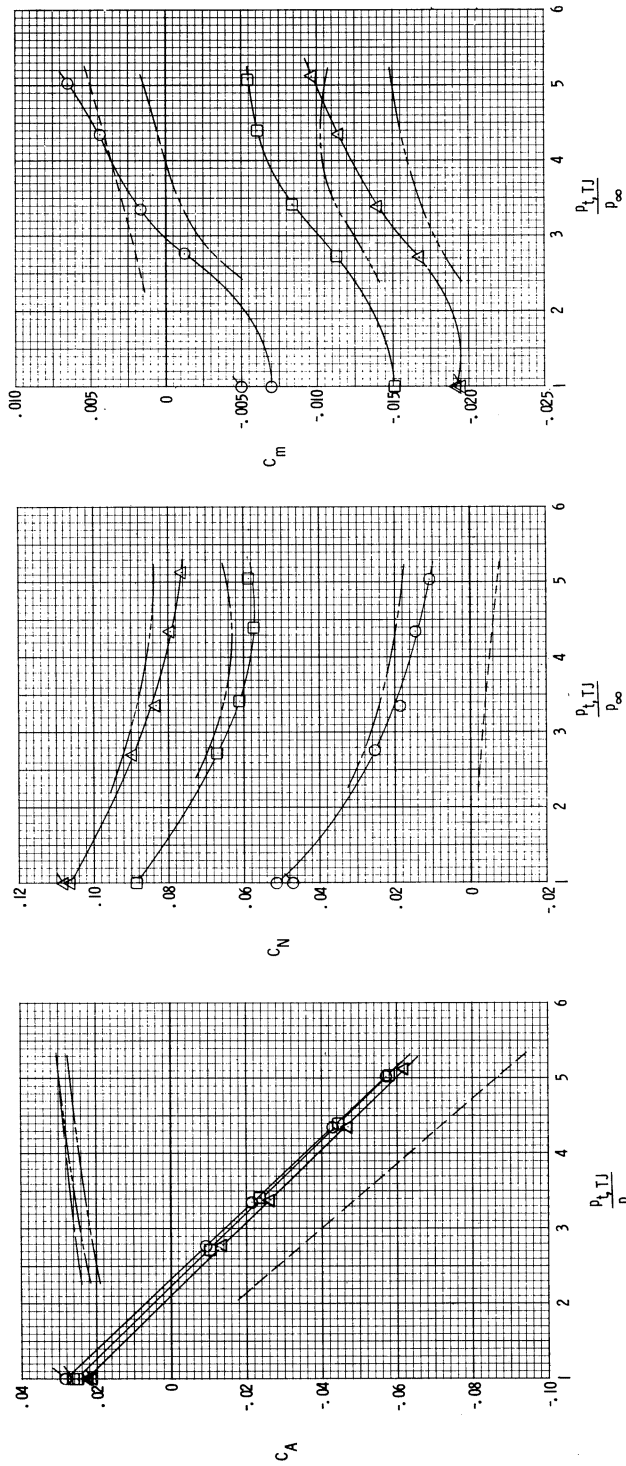


Figure 24.— Force and moment coefficient variation with turbojet pressure ratio.  
 $\epsilon = 50$  with flowthrough nacelle and flow fences.

$\alpha$ , deg	Data	Corrected data
0	○	—
2	□	—
3	△	—

-----  $C_A, T_J, C_N, T_J$ , or  $C_m, T_J$

Flagged symbol indicates data at end of  $p_{t, T_J}$  sweep



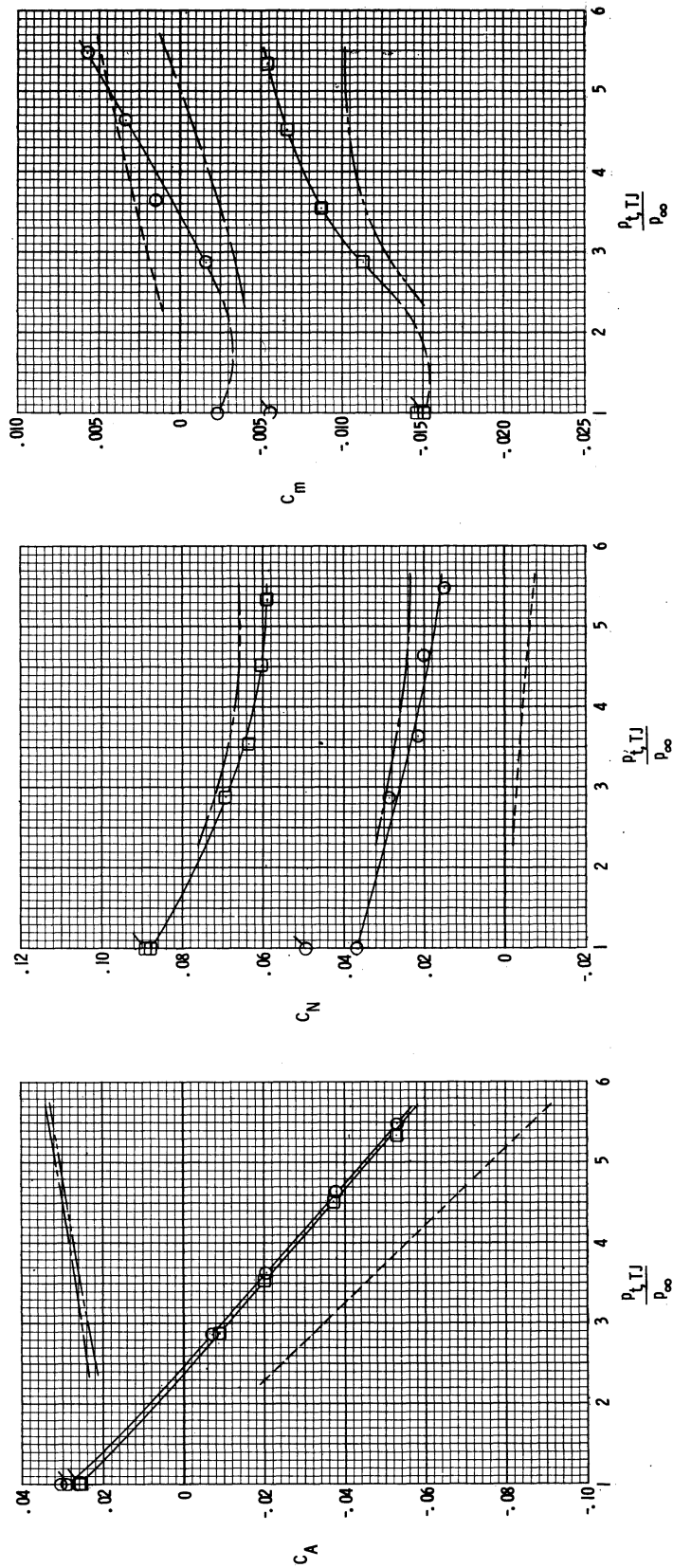
(b)  $M_{\infty} = 0.80$ .

Figure 24.- Continued.

$\alpha$ , deg	Data	Corrected data
0	○	—
2	□	—
3	△	—

-----  $C_{A,TJ}$ ,  $C_{N,TJ}$ , or  $C_{m,TJ}$

Flagged symbol indicates data at end of  $p_{t,TJ}$  sweep



(c)  $M_{\infty} = 0.85$ .

Figure 24.- Concluded.



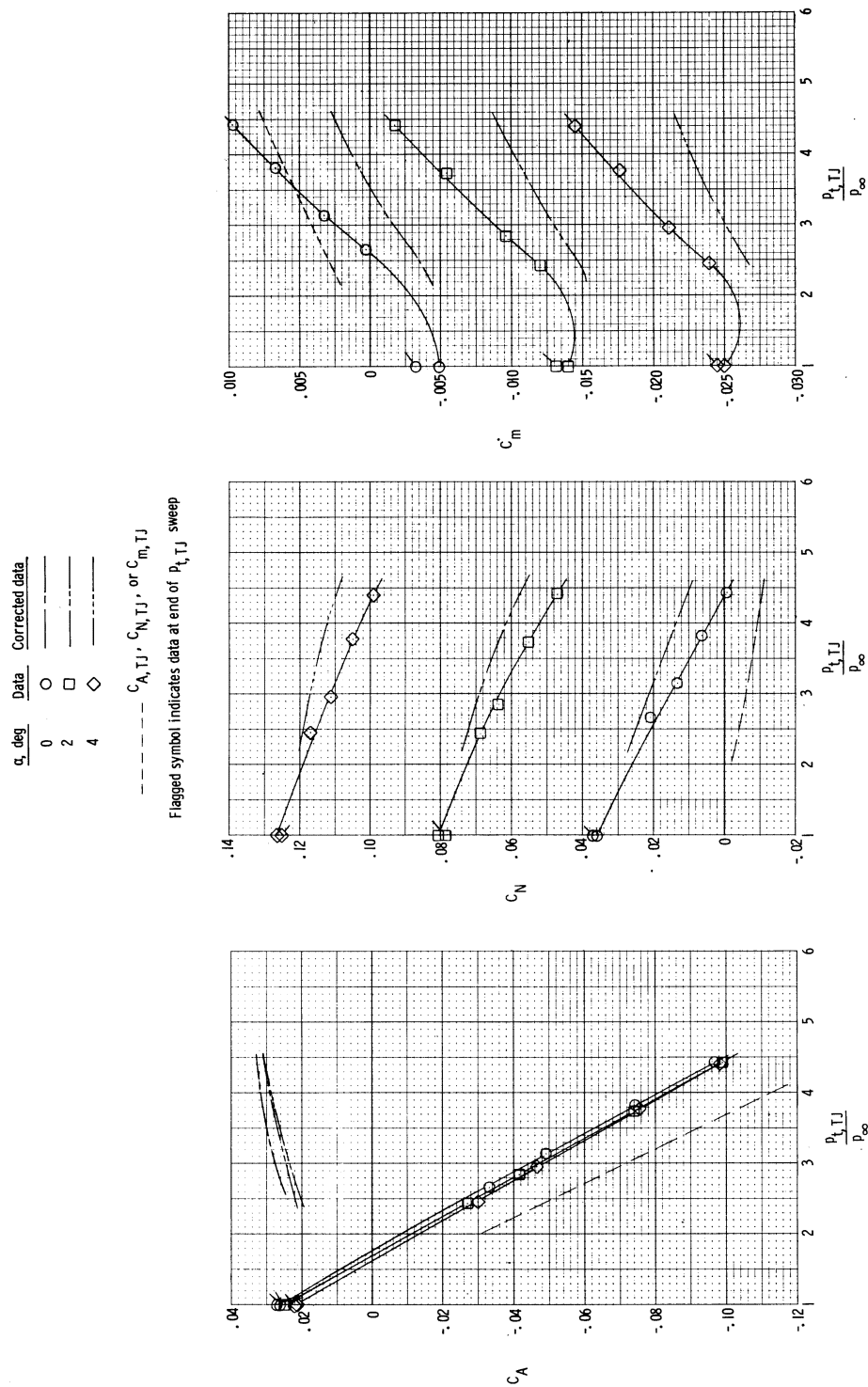
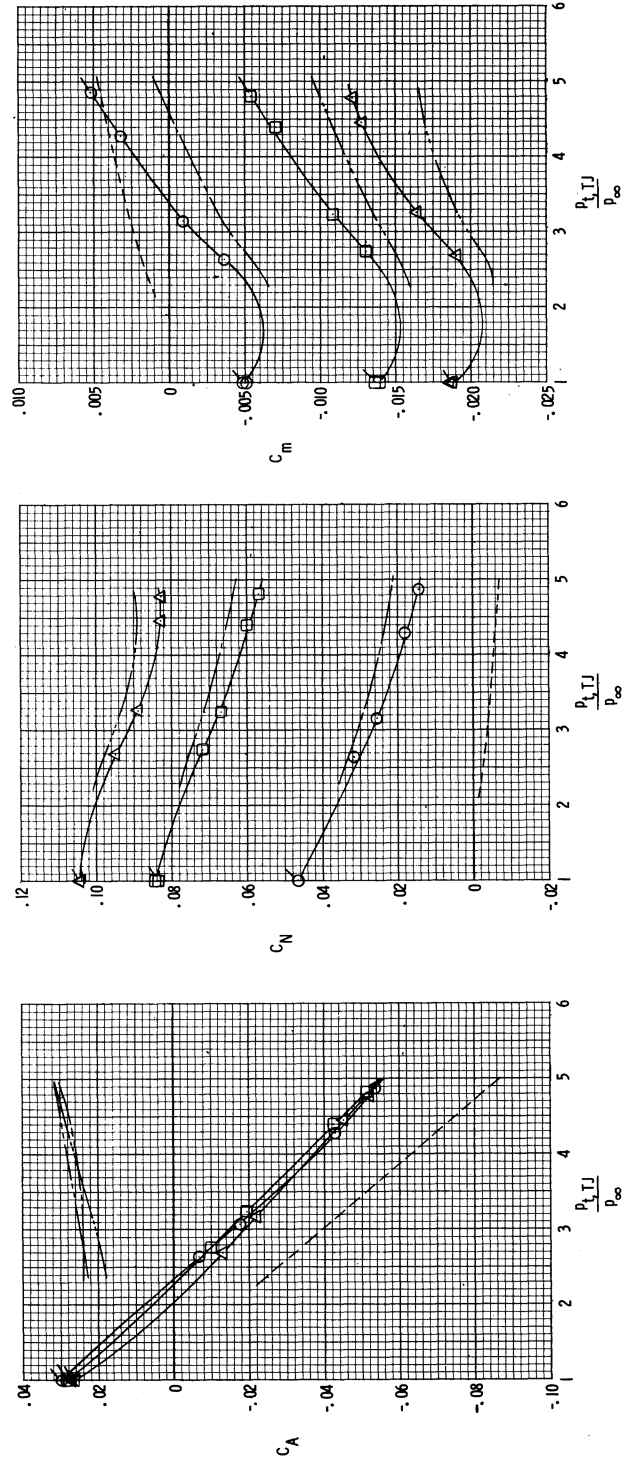


Figure 25.- Force and moment coefficient variation with turbojet pressure ratio.  
 $\epsilon = 10^\circ$  with flowthrough nacelle and flow fences.

$\alpha$ , deg	Data	Corrected data
0	○	—
2	□	—
3	△	—

-----  $C_{A,TJ}, C_{N,TJ}, \text{ or } C_{m,TJ}$

Flagged symbol indicates data at end of  $p_{t,TJ}$  sweep



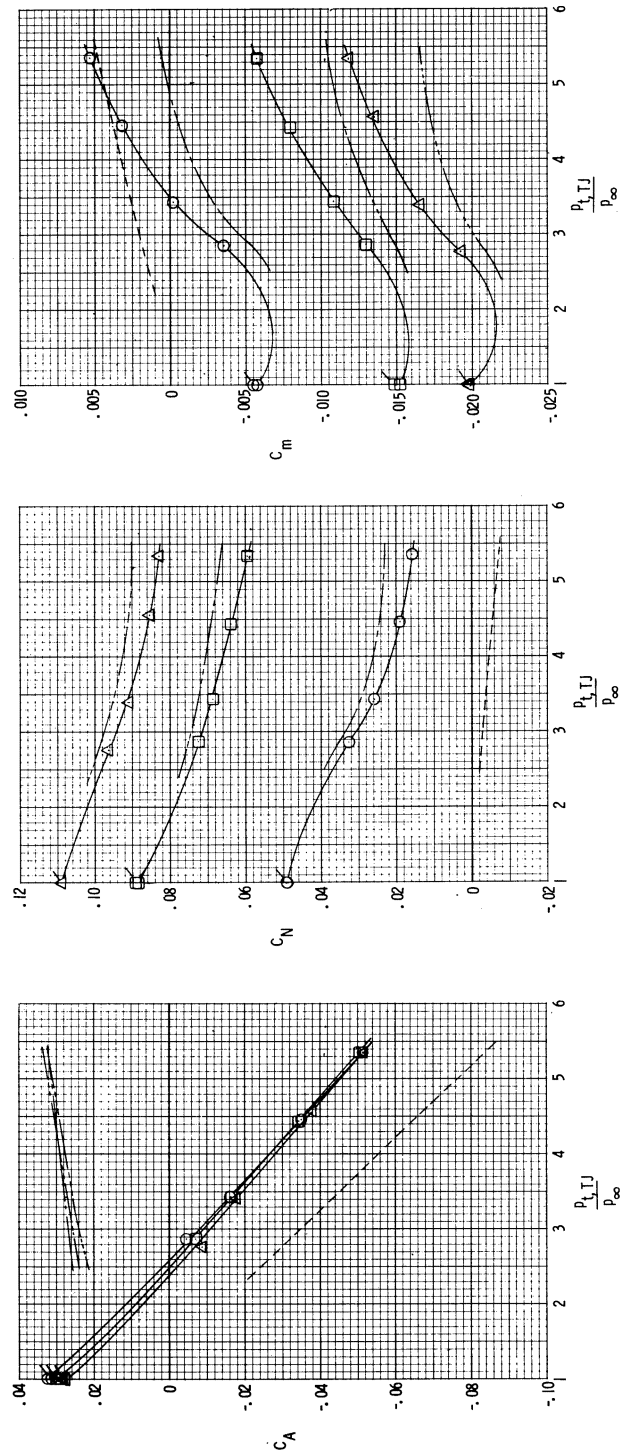
(b)  $M_\infty = 0.80$ .

Figure 25.- Continued.

$\alpha$ , deg	Data	Corrected data
0	O	-----
2	□	-----
3	△	-----

-----  $C_{A,TJ}$ ,  $C_{N,TJ}$ , or  $C_{m,TJ}$

Flagged symbol indicates data at end of  $p_{t,TJ}$  sweep



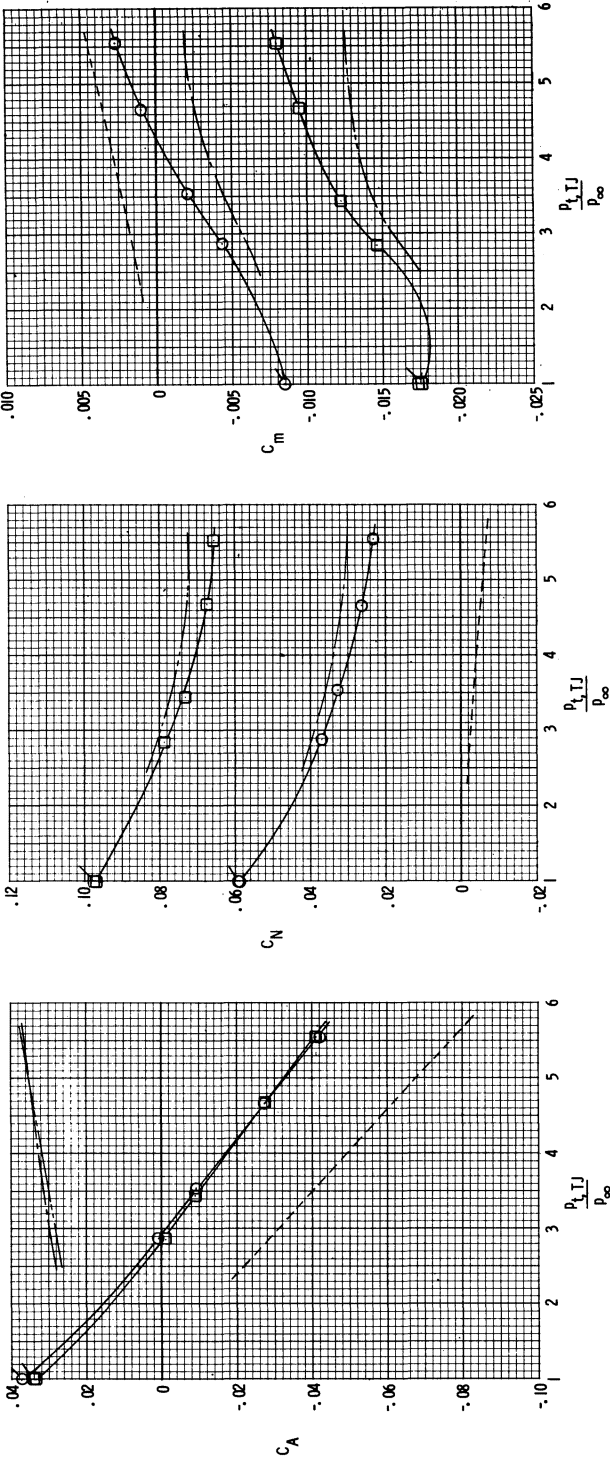
(c)  $M_{\infty} = 0.85$ .

Figure 25.- Continued.

$\alpha$ , deg	Data	Corrected data
0	○	—
2	□	—

-----  $C_A, T, C_N, T, C_m, T$

Flagged symbol indicates data at end of  $p_{t, T}$  sweep



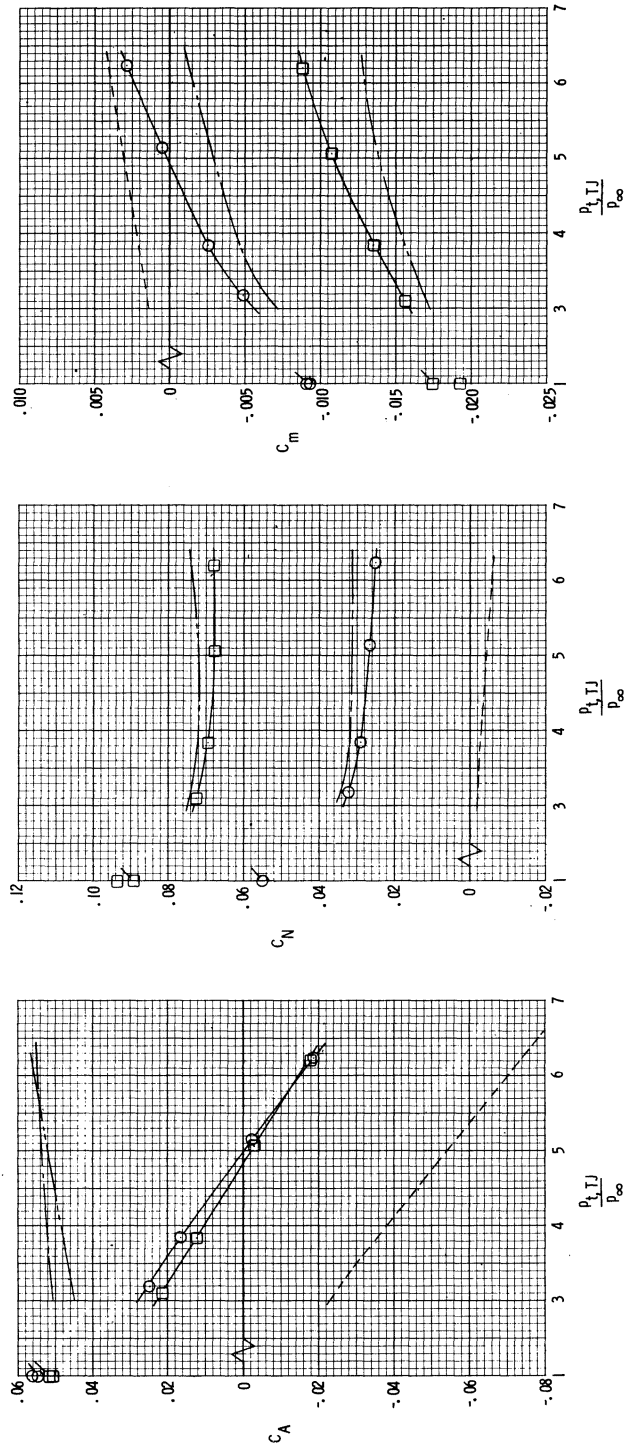
(d)  $M_\infty = 0.90$ .

Figure 25.- Continued.

$\alpha$ , deg	Data	Corrected data
0	○	—
2	□	---

-----  $C_{A,TJ}, C_{N,TJ}$ , or  $C_{m,TJ}$

Flagged symbol indicates data at end of  $p_{t,TJ}$  sweep



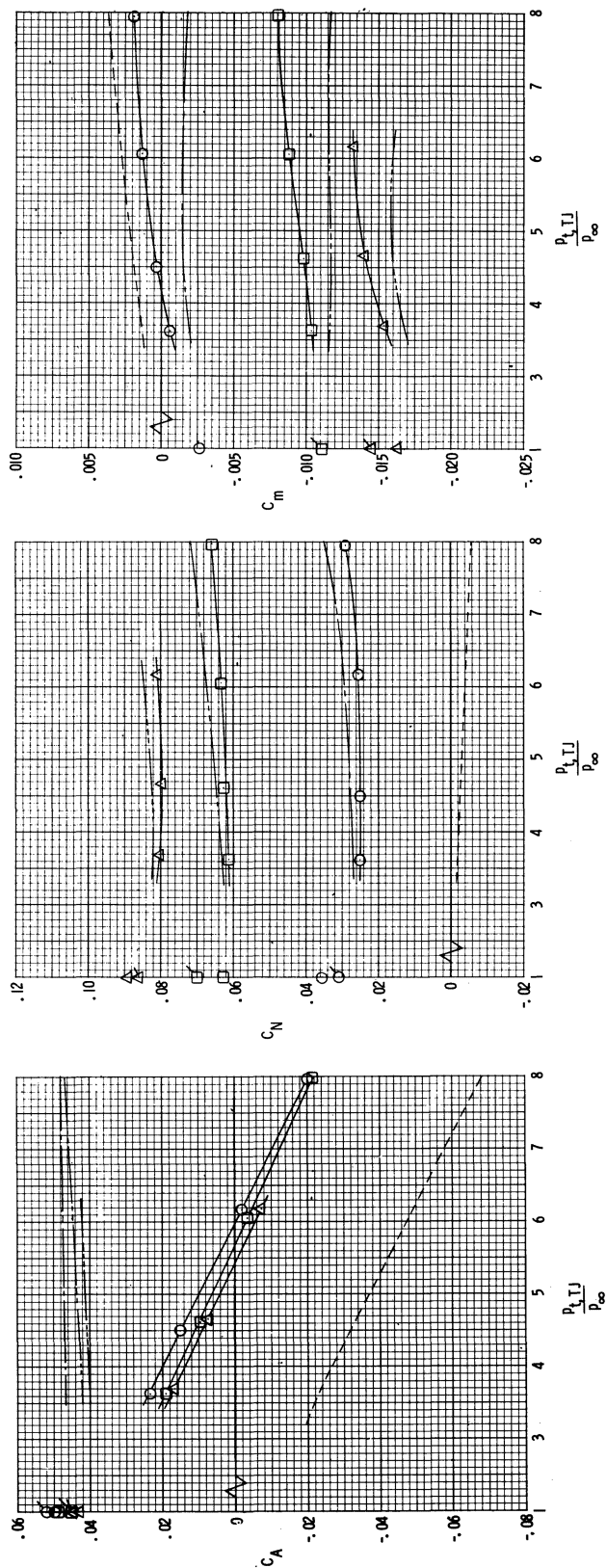
(e)  $M_{\infty} = 1.00$ .

Figure 25.- Continued.

$\alpha$ , deg	Data	Corrected data
0	○	—
2	□	—
3	△	—

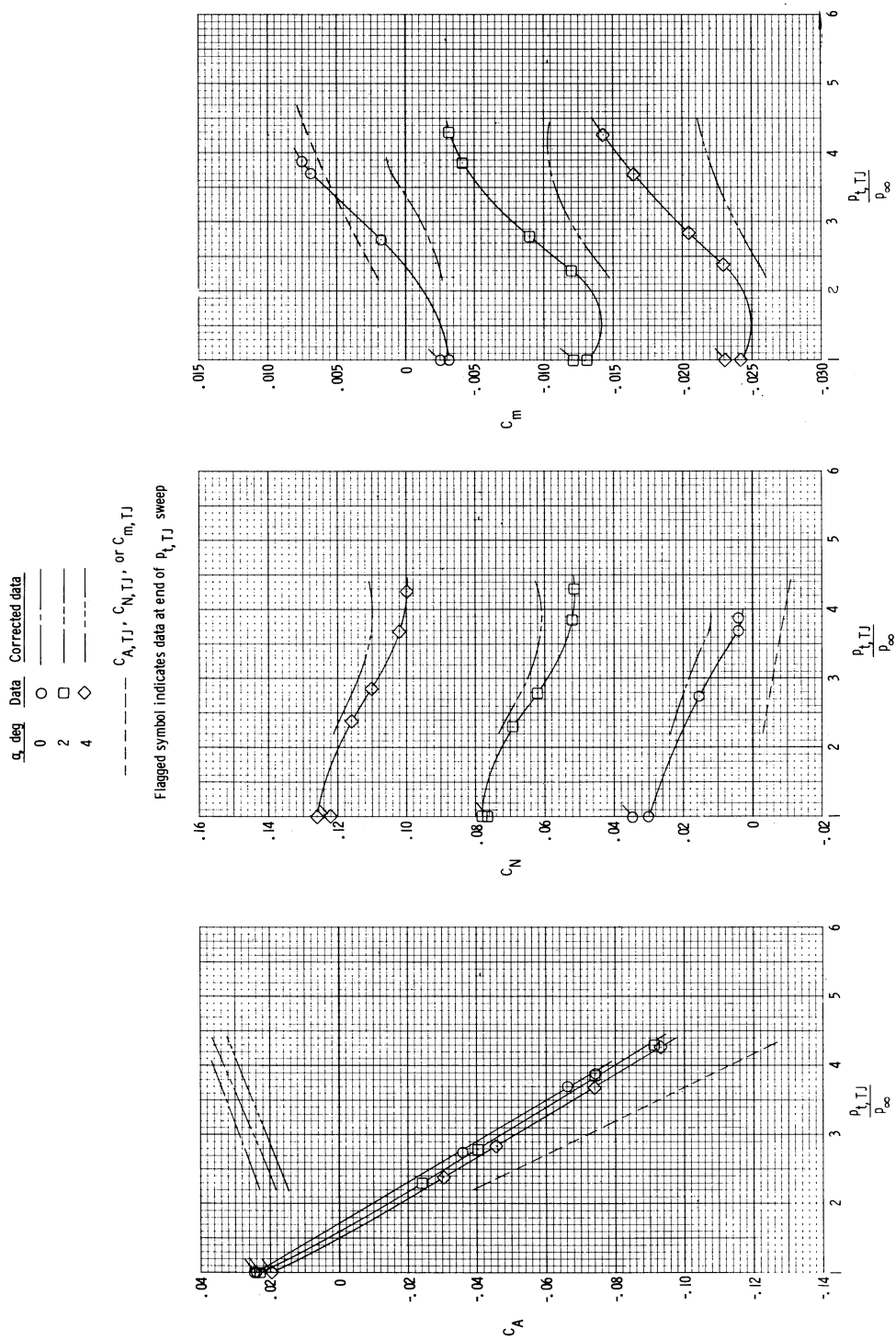
-----  $C_{A,TJ}$ ,  $C_{N,TJ}$ , or  $C_{m,TJ}$

Flagged symbol indicates data at end of  $p_{t,TJ}$  sweep



(f)  $M_{\infty} = 1.20$ .

Figure 25.- Concluded:



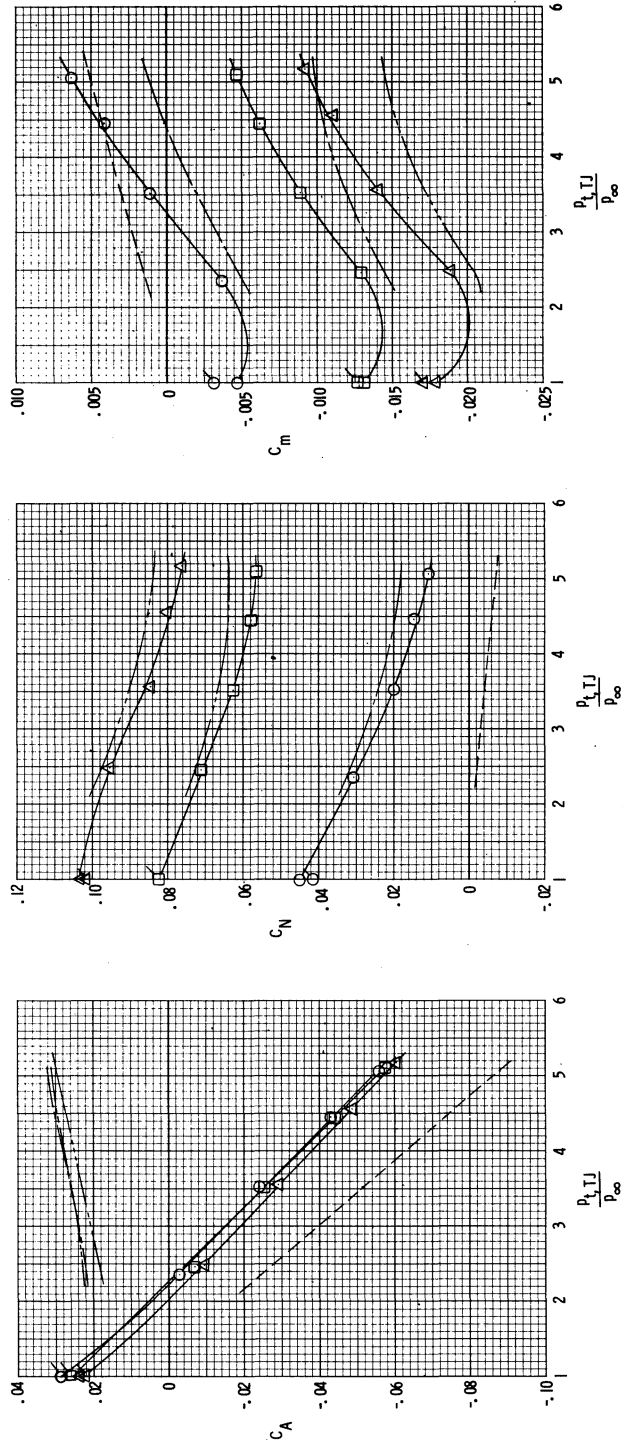
(a)  $M_\infty = 0.60$ .

Figure 26.- Force and moment coefficient variation with turbojet pressure ratio.  
 $\epsilon = 20^\circ$  with flowthrough nacelle and flow fences.

$\alpha$ , deg	Data	Corrected data
0	$\circ$	—
2	$\square$	—
3	$\triangle$	—

-----  $C_{A,TJ}$ ,  $C_{N,TJ}$ , or  $C_{m,TJ}$

Flagged symbol indicates data at end of  $p_{t,TJ}$  sweep



(b)  $M_{\infty} = 0.80$ .

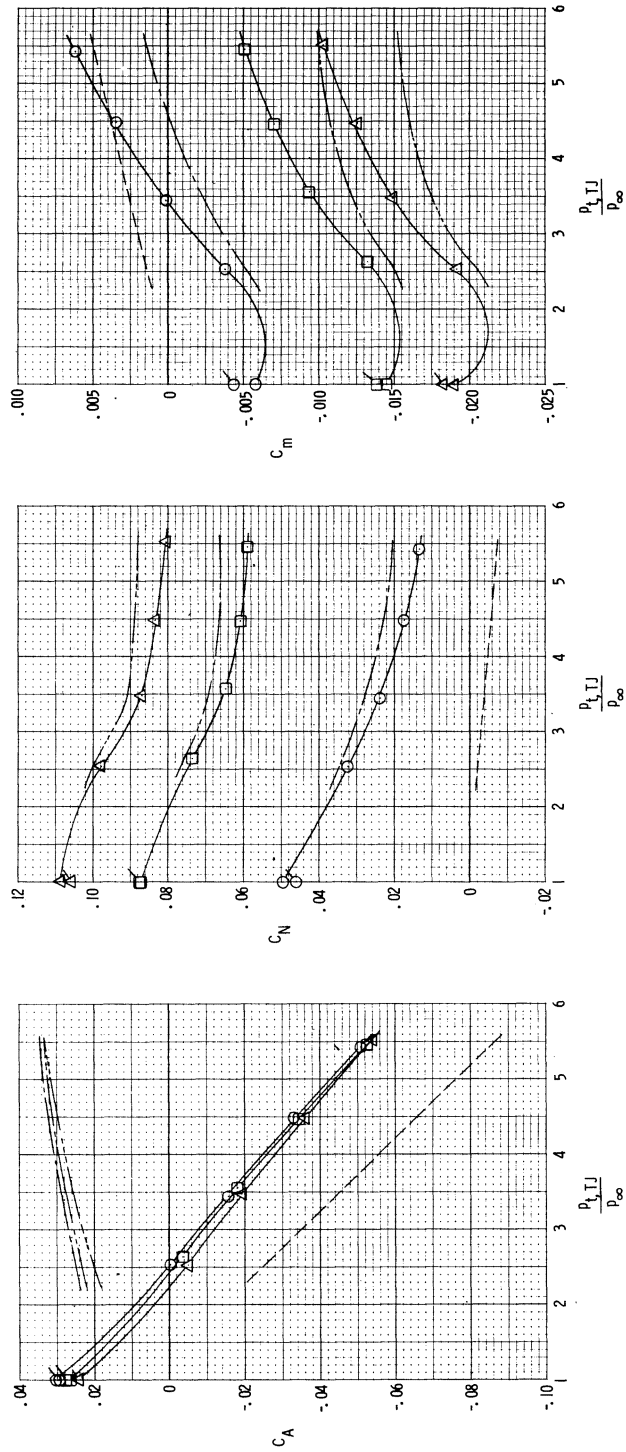
Figure 26.- Continued.



$\alpha$ , deg	Data	Corrected data
0	○	—
2	□	—
3	△	—

-----  $C_{A,TJ}$ ,  $C_{N,TJ}$ , or  $C_{m,TJ}$

Flagged symbol indicates data at end of  $p_{t,TJ}$  sweep



(c)  $M_{\infty} = 0.85$ .

Figure 26.- Concluded.

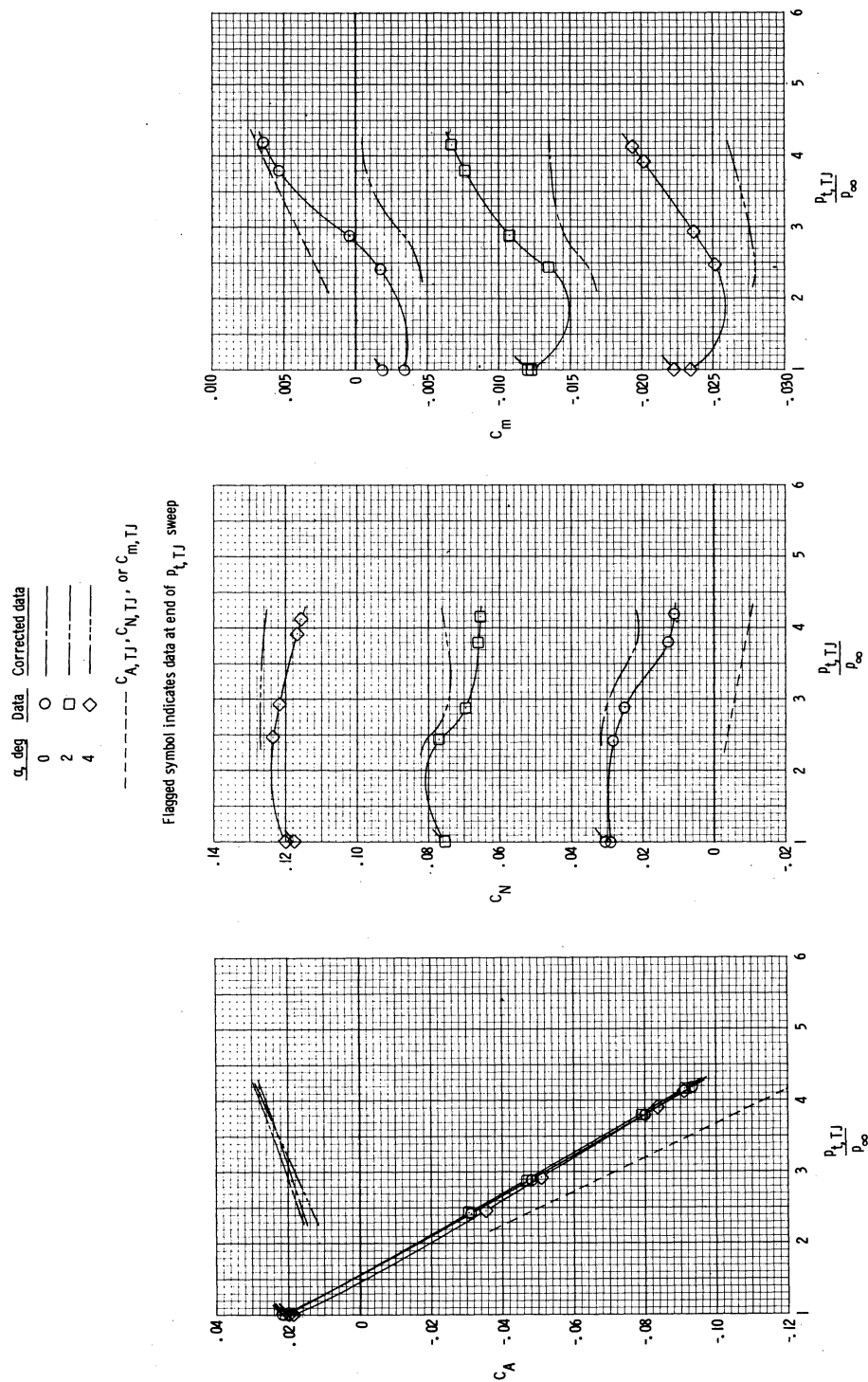
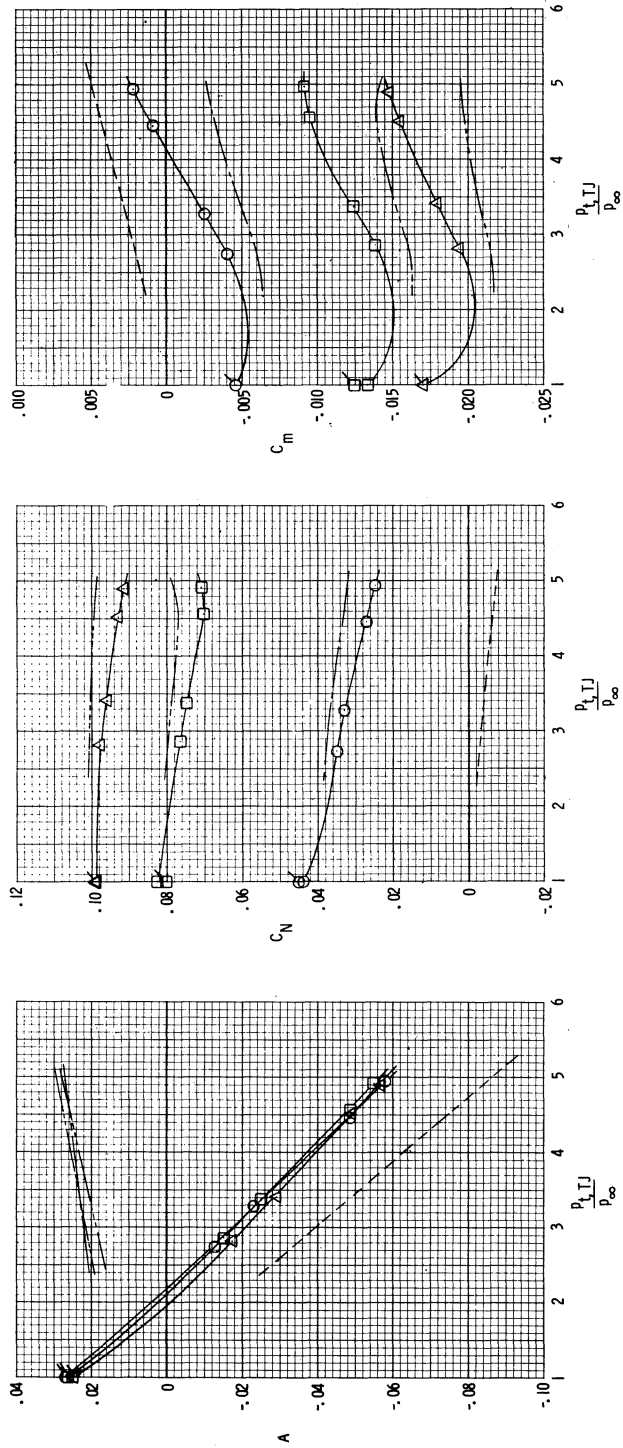


Figure 27.-- Force and moment coefficient variation with turbojet pressure ratio.  
No flow fences;  $\epsilon = 20^\circ$  with flowthrough nacelle.

$\alpha$ , deg	Data	Corrected data
0	○	—
2	□	—
3	△	—

-----  $C_{A,TJ}$ ,  $C_{N,TJ}$ , or  $C_{m,TJ}$

Flagged symbol indicates data at end of  $p_{t,TJ}$  sweep



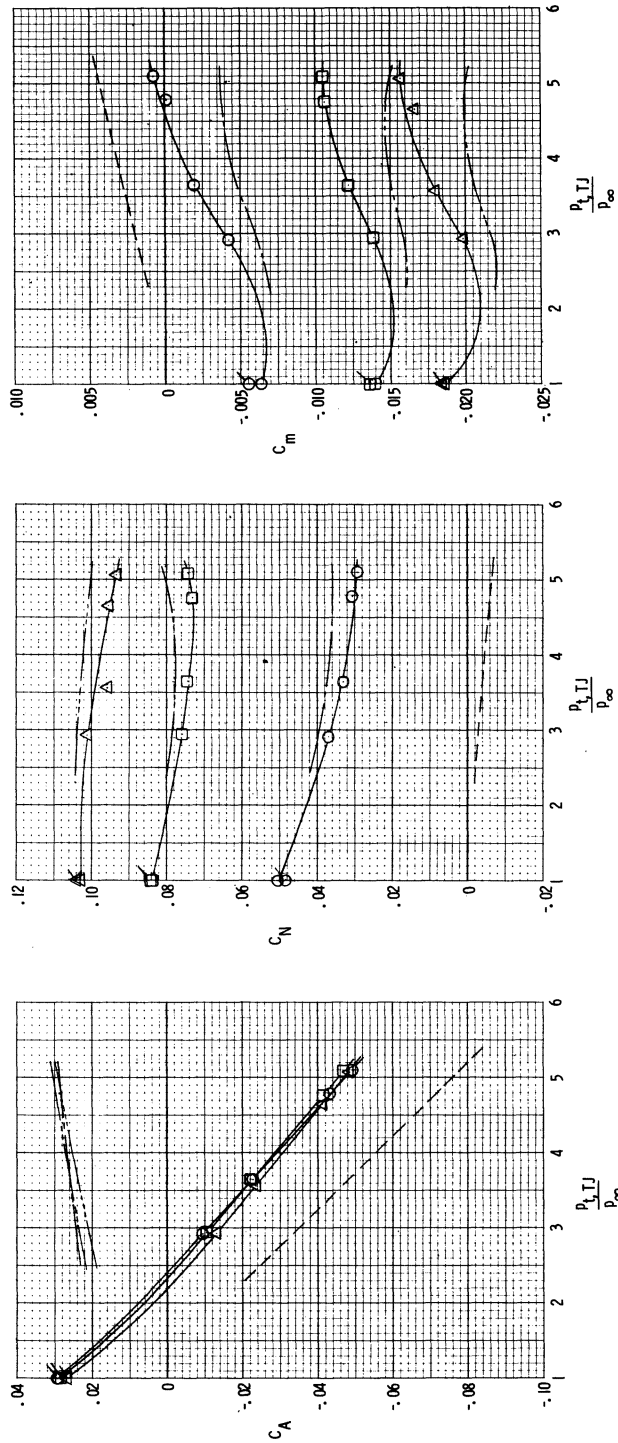
(b)  $M_{\infty} = 0.80$ .

Figure 27.- Continued.

$\alpha$ , deg	Data	Corrected data
0	○	—
2	□	—
3	△	—

-----  $C_{A,TJ}$ ,  $C_{N,TJ}$ , or  $C_{m,TJ}$

Flagged symbol indicates data at end of  $p_{t,TJ}$  sweep



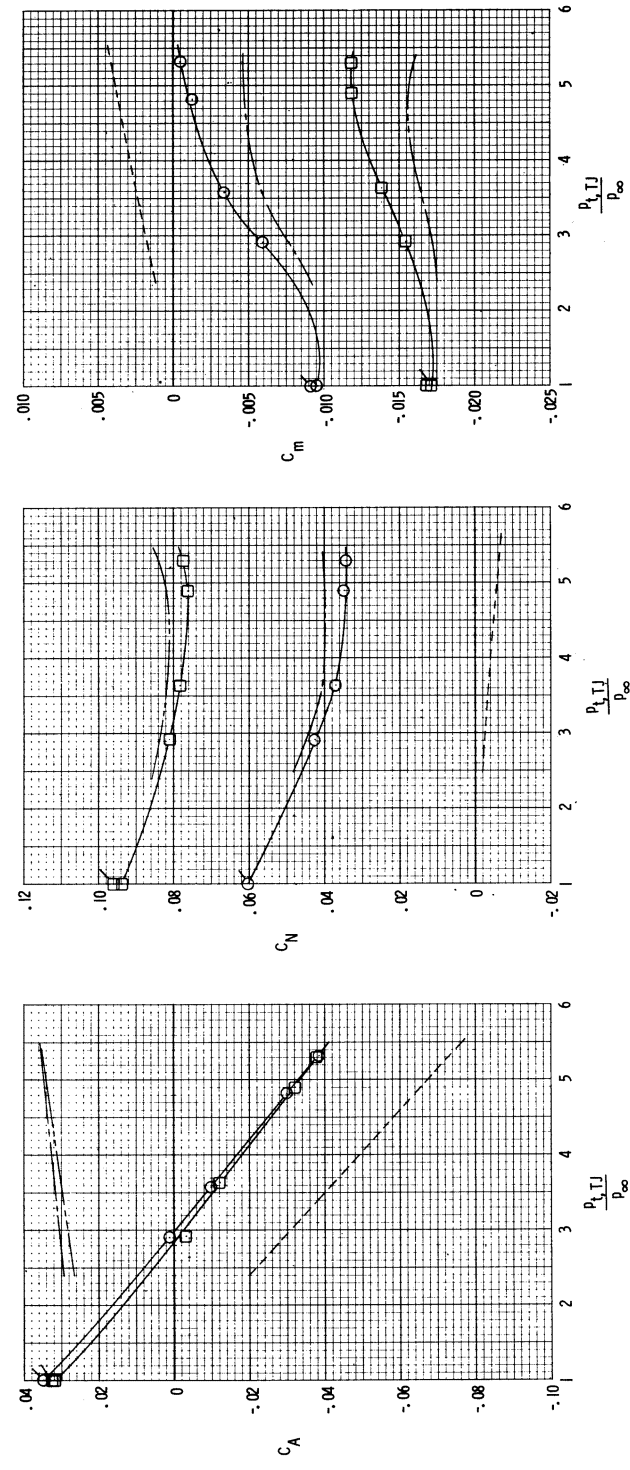
(c)  $M_\infty = 0.85$ .

Figure 27.- Continued.

$\alpha$ , deg	Data	Corrected data
0	○	—
2	□	---

-----  $C_{A,TJ}$ ,  $C_{N,TJ}$  or  $C_{m,TJ}$

Flagged symbol indicates data at end of  $p_{t,TJ}$  sweep



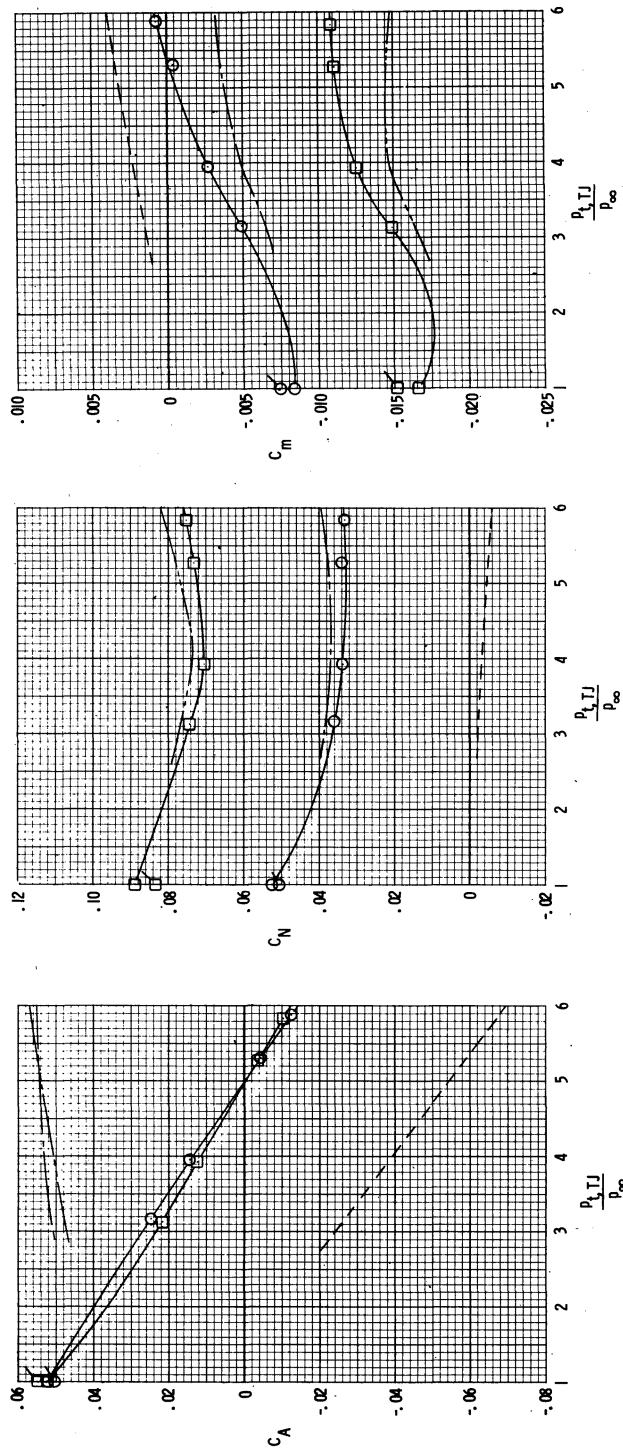
(d)  $M_{\infty} = 0.90$ .

Figure 27.- Continued.

$\alpha$ , deg	Data	Corrected data
0	○	—
2	□	---

-----  $C_{A,TJ}$ ,  $C_{N,TJ}$  or  $C_{m,TJ}$

Flagged symbol indicates data at end of  $p_{t,TJ}$  sweep



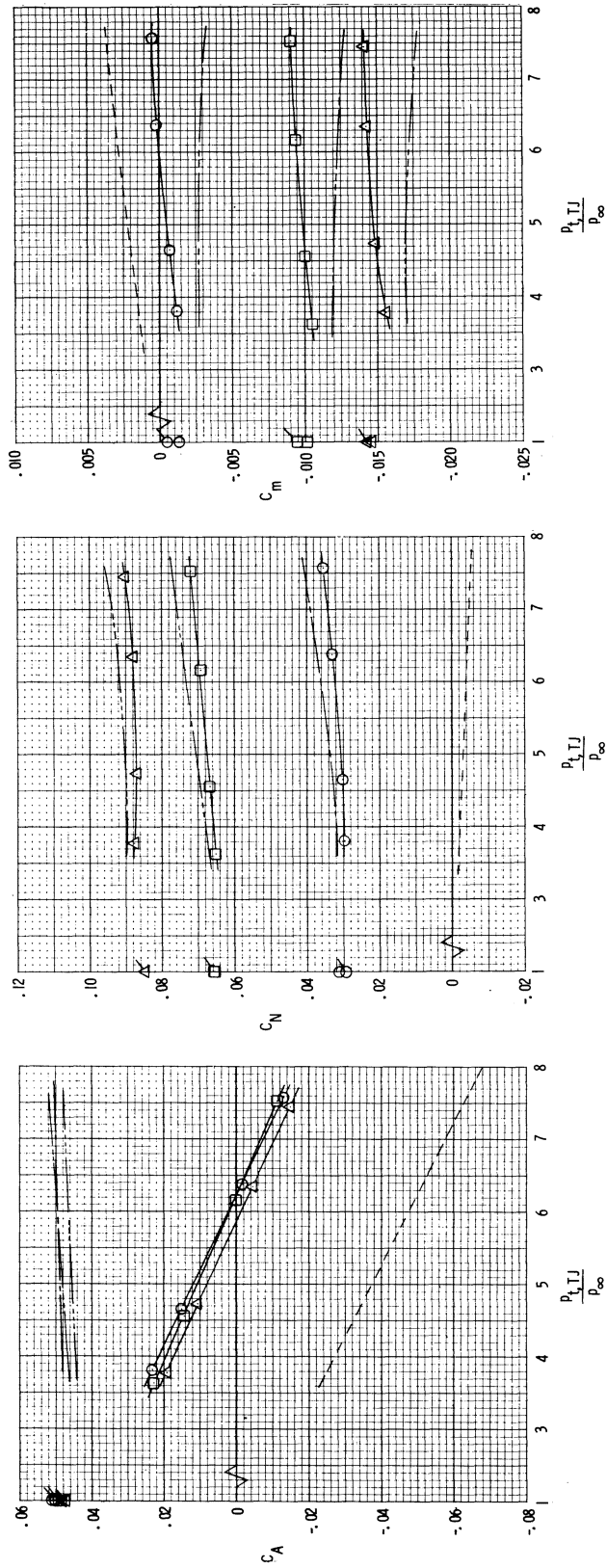
(e)  $M_{\infty} = 1.00$ .

Figure 27.- Continued..

$\alpha$ , deg	Data	Corrected data
0	○	—
2	□	—
3	△	—

-----  $C_{A,TJ}$ ,  $C_{N,TJ}$  or  $C_{m,TJ}$

Flagged symbol indicates data at end of  $P_{t,TJ}$  sweep



(f)  $M_{\infty} = 1.20$ .

Figure 27.- Concluded.

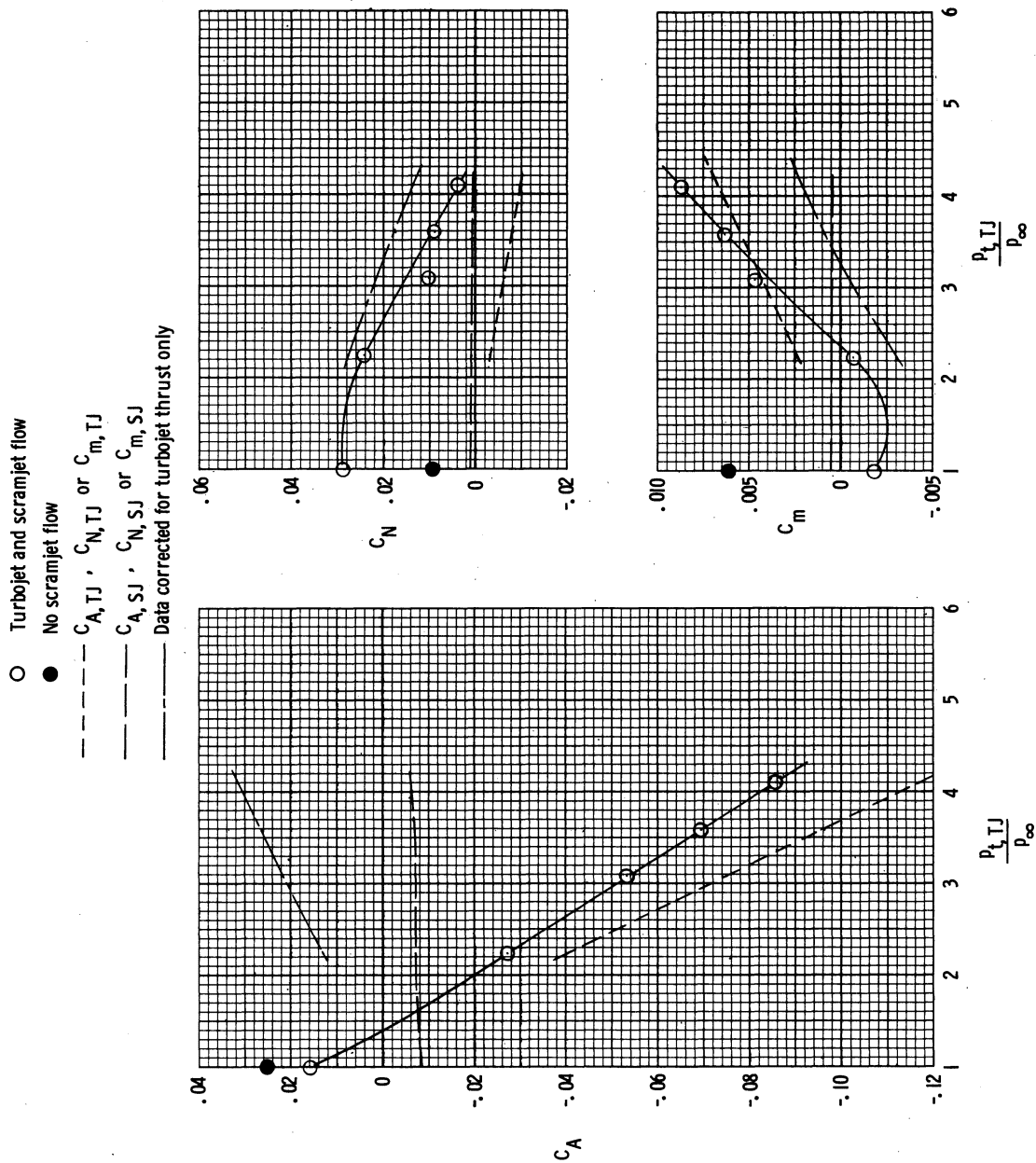
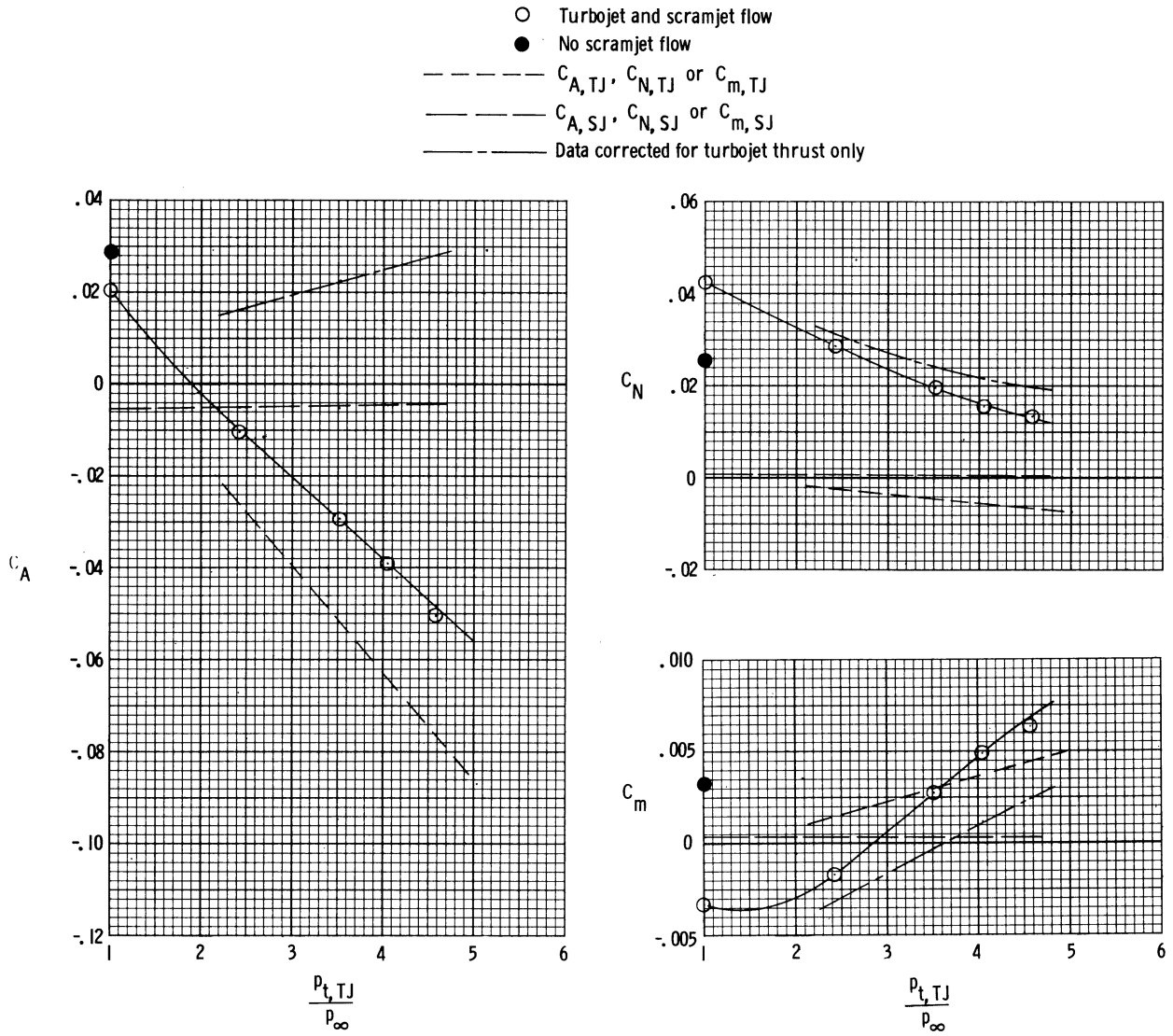


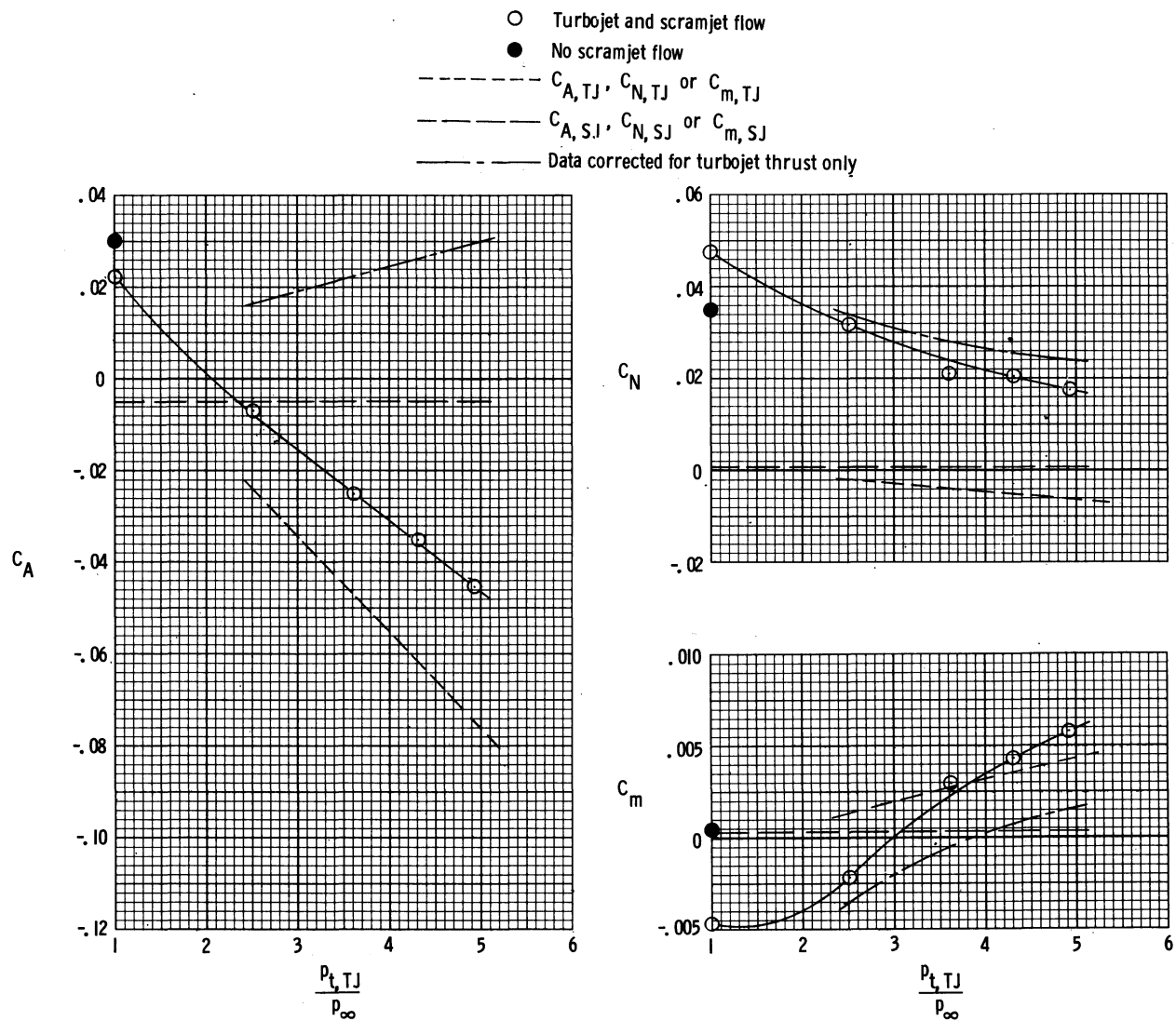
Figure 28.- Force and moment coefficient variation with turbojet pressure ratio for constant values of  $H_2O_2$  scramjet pressure ratio.  $\alpha = 0^\circ$ ;  $\epsilon = 20^\circ$ ; with flow fences.





(b)  $M_\infty = 0.80$ ;  $\bar{p}_{t,SJ}/p_\infty = 1.92$ .

Figure 28.- Continued.



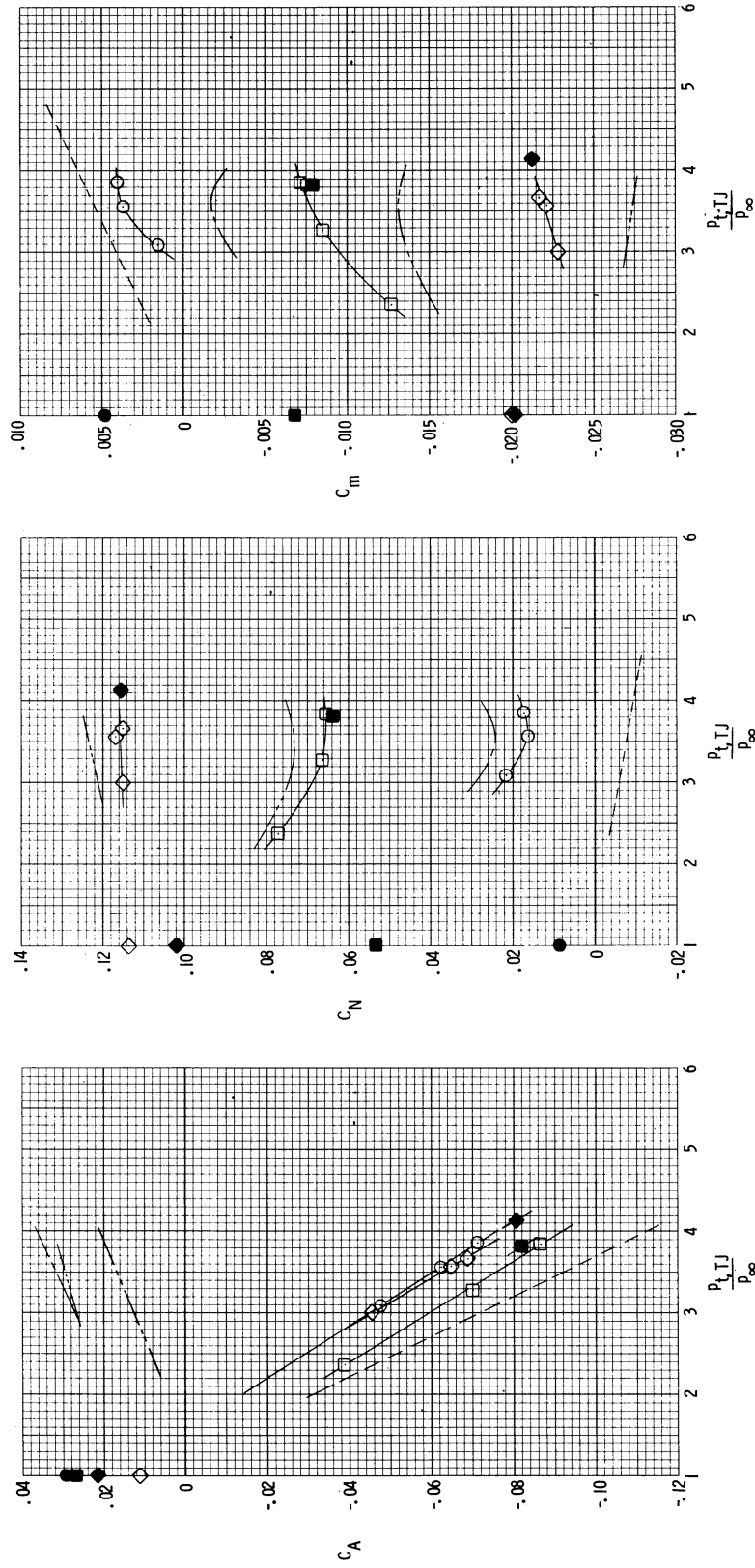
(c)  $M_\infty = 0.85$ ;  $\bar{p}_{t,SJ}/p_\infty = 1.97$ .

Figure 28.- Concluded.

$\alpha$ , deg	Data	Data corrected for TJ thrust only	$\frac{P_{t,TJ}}{P_{\infty}}$	$C_{A,SJ}$	$C_{N,SJ}$	$C_{m,SJ}$
0	○	—	1.67	-.0060	-.0006	.0004
2	□	—	1.84	-.0074	.0008	.0005
4	◇	—	1.63	-.0057	.0006	.0004

Solid symbol indicates no scramjet flow

-----  $C_{A,TJ}$ ,  $C_{N,TJ}$  or  $C_{m,TJ}$



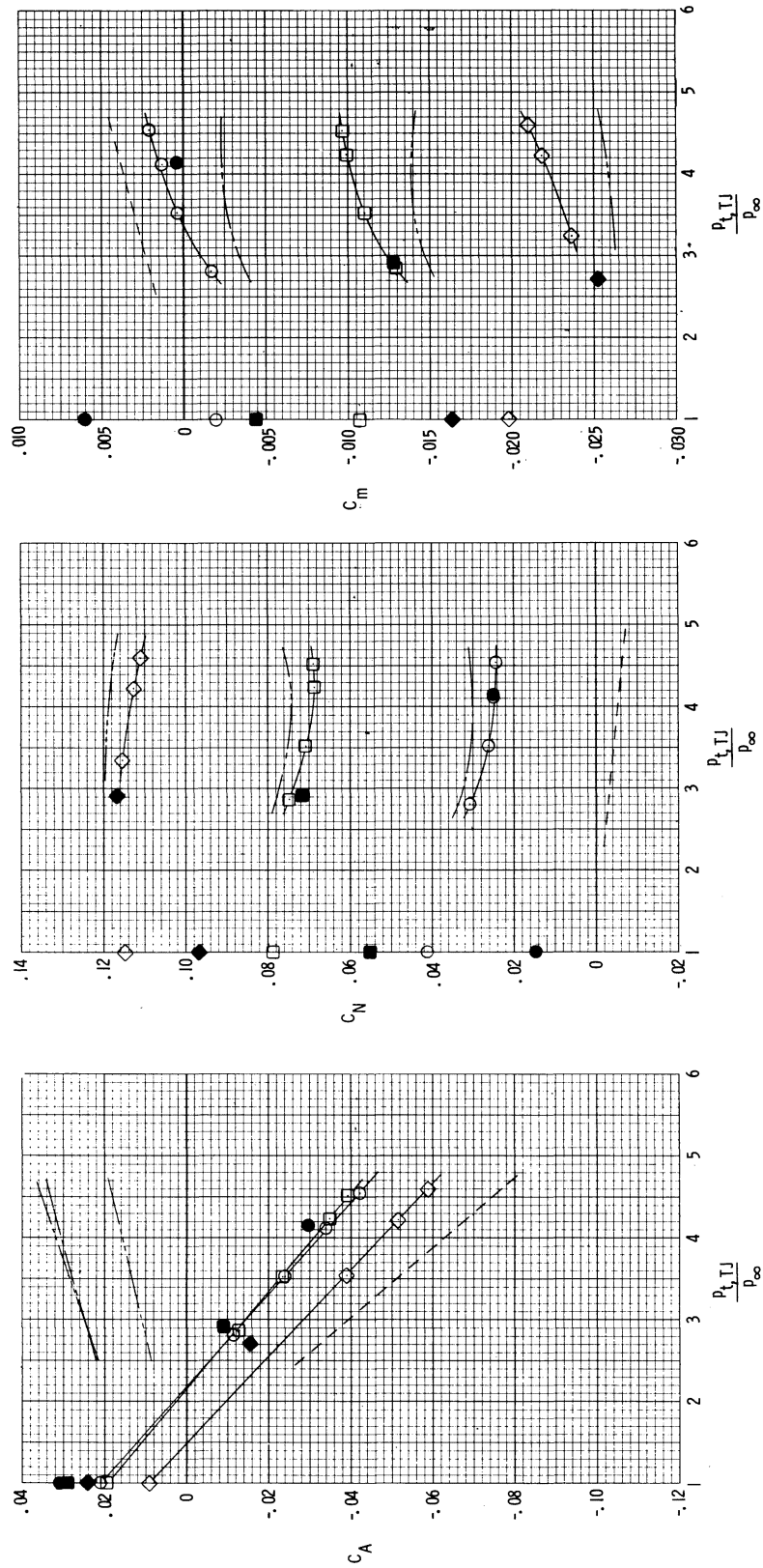
(a)  $M_{\infty} = 0.6$ .

Figure 29.- Force and moment coefficient variation with turbojet pressure ratio for constant values of  $H_2O_2$  scramjet pressure ratio.  $\epsilon = 20^\circ$ ; without flow fences.

$\alpha$ , deg	Data	Data corrected for TJ thrust only	$\frac{p_{t,SJ}}{p_{\infty}}$	$C_{A,SJ}$	$C_{N,SJ}$	$C_{m,SJ}$
0	○	—	1.78	-.0043	.0005	.0003
2	□	—	1.61	-.0036	.0004	.0002
4	◇	—	1.67	-.0039	.0004	.0003

-----  $C_{A,TJ}$ ,  $C_{N,TJ}$  or  $C_{m,TJ}$

Solid symbol indicates no scramjet flow.



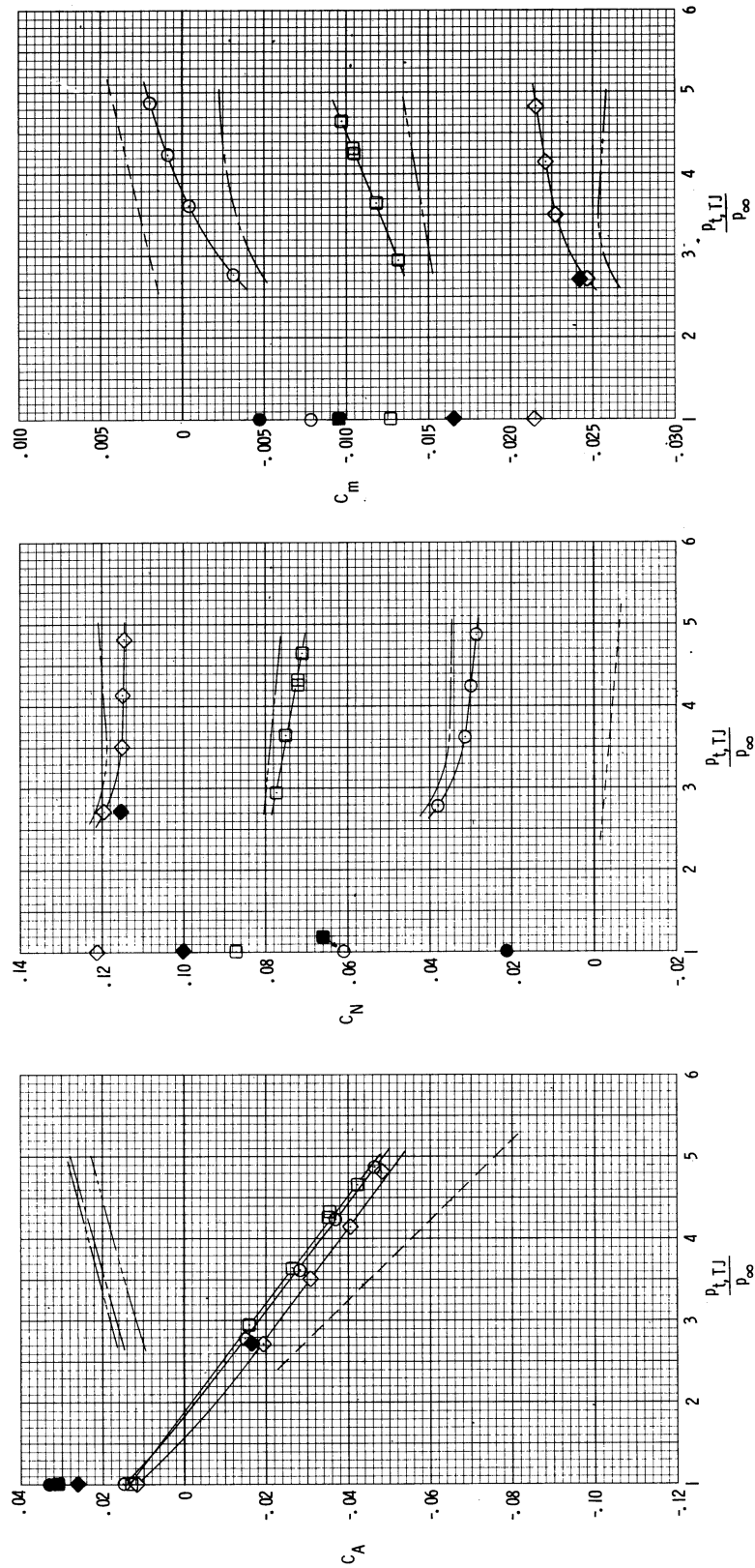
(b)  $M_{\infty} = 0.80$ .

Figure 29.- Continued.

$\alpha$ , deg	Data	Data corrected for TJ thrust only	$\frac{p_{t,SJ}}{p_\infty}$	$C_{A,SJ}$	$C_{N,SJ}$	$C_{m,SJ}$
0	○	—	1.74	-.0038	.0004	.0003
2	□	—	1.74	-.0038	.0004	.0003
4	◇	—	1.88	-.0043	.0005	.0003

-----  $C_{A,TJ}$ ,  $C_{N,TJ}$  or  $C_{m,TJ}$

Solid symbol indicates no scramjet flow



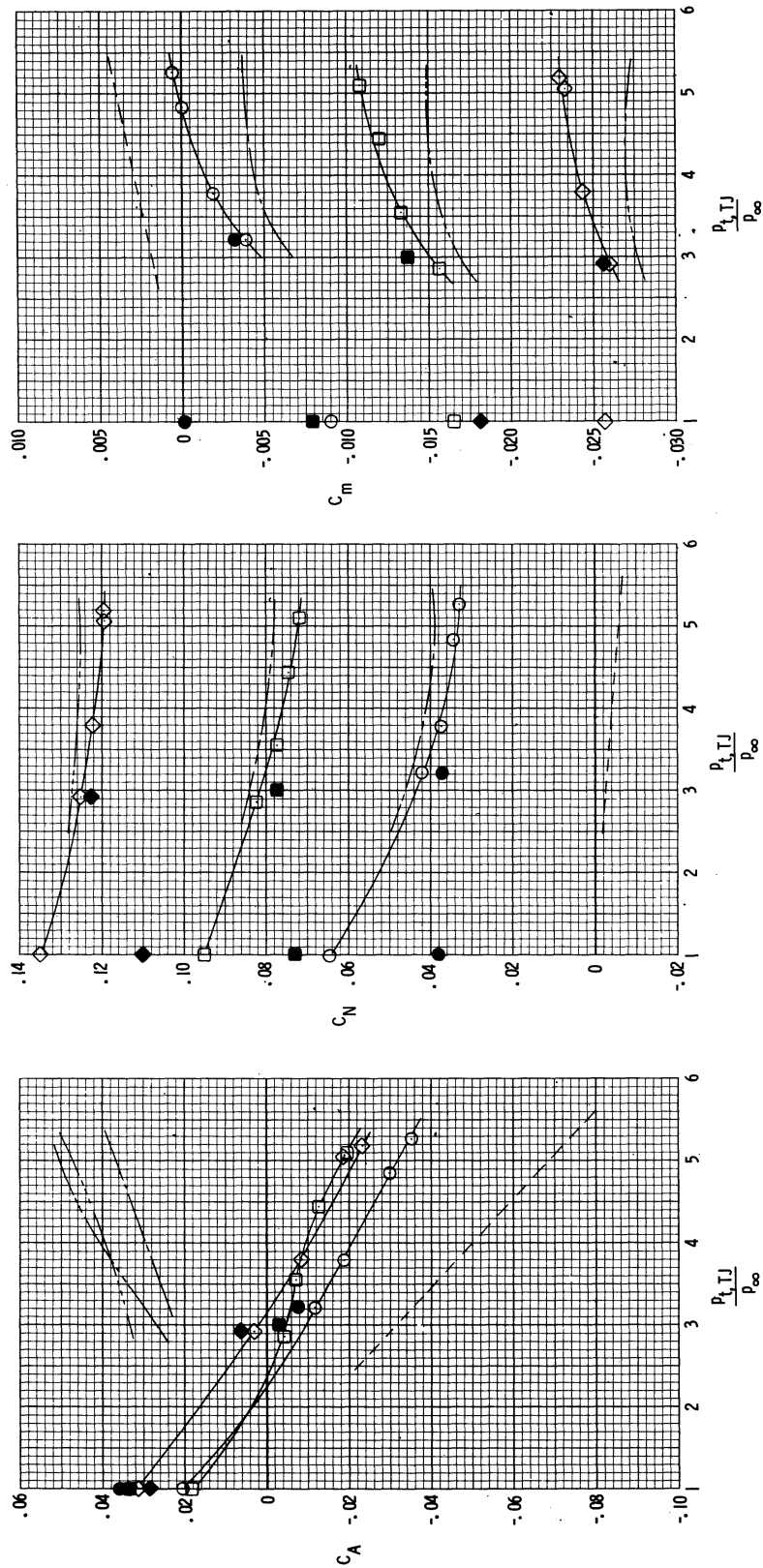
(c)  $M_\infty = 0.85$ .

Figure 29.- Continued.

$\alpha$ , deg	Data	Data corrected for TJ thrust only	$\frac{p_{t,TJ}}{p_\infty}$	$C_{A,SJ}$	$C_{N,SJ}$	$C_{m,SJ}$
0	○	—	2.05	-.0046	.0005	.0003
2	□	—	1.96	-.0043	.0004	.0003
4	◇	—	1.96	-.0043	.0004	.0003

-----  $C_{A,TJ}$ ,  $C_{N,TJ}$  or  $C_{m,TJ}$

Solid symbol indicates no scramjet flow



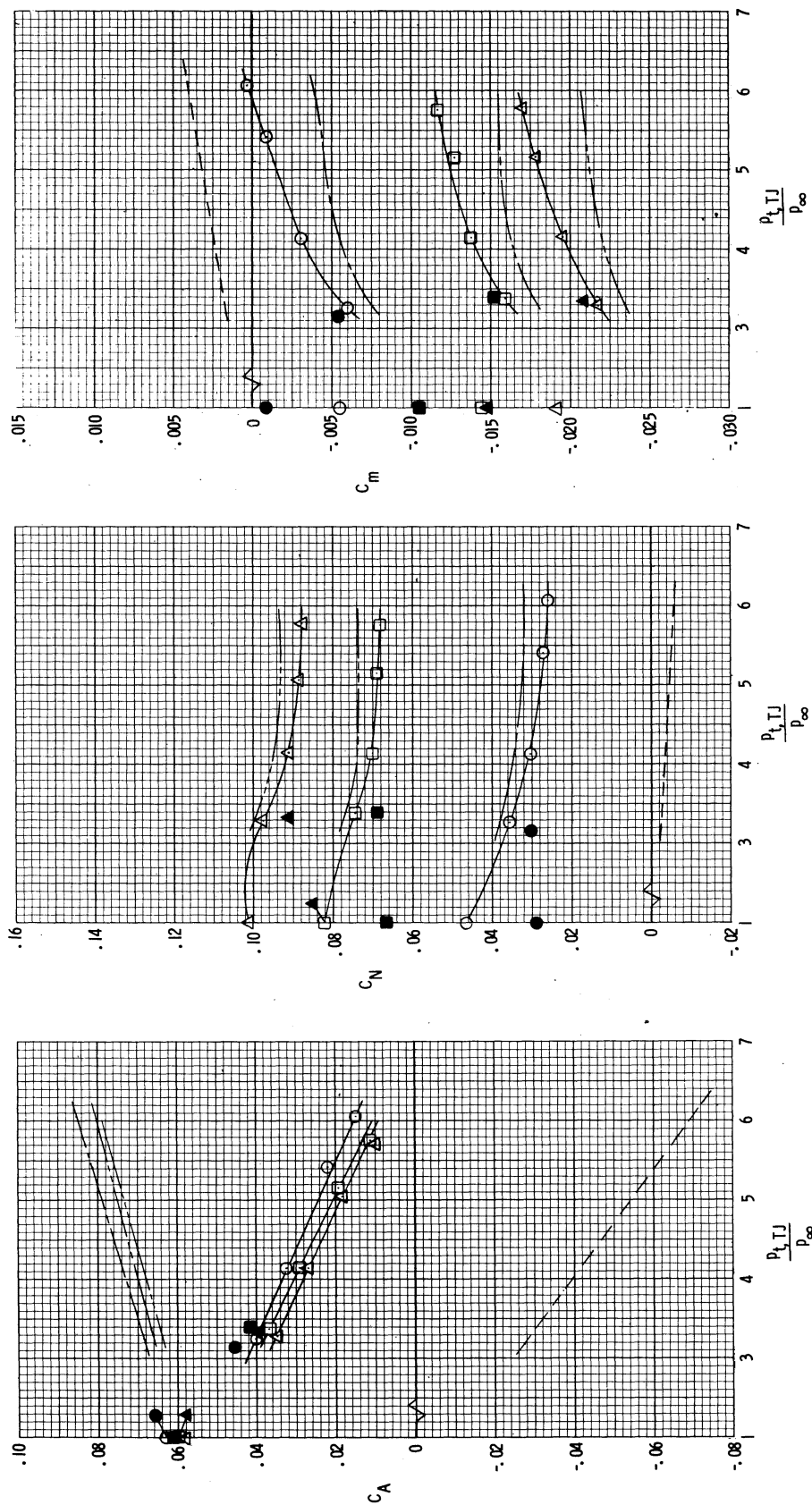
(d)  $M_\infty = 0.90$ .

Figure 29.- Continued.

$\alpha$ , deg	Data	Data corrected for TJ thrust only	$\frac{F_{t,TJ}}{p_{\infty}}$	$C_{A,SJ}$	$C_{N,SJ}$	$C_{m,SJ}$
0	○	—	2.04	-.0039	.0004	.0003
2	□	—	2.09	-.0041	.0004	.0003
3	△	—	2.20	-.0044	.0005	.0003

-----  $C_{A,TJ}$ ,  $C_{N,TJ}$  or  $C_{m,TJ}$

Solid symbol indicates no scramjet flow

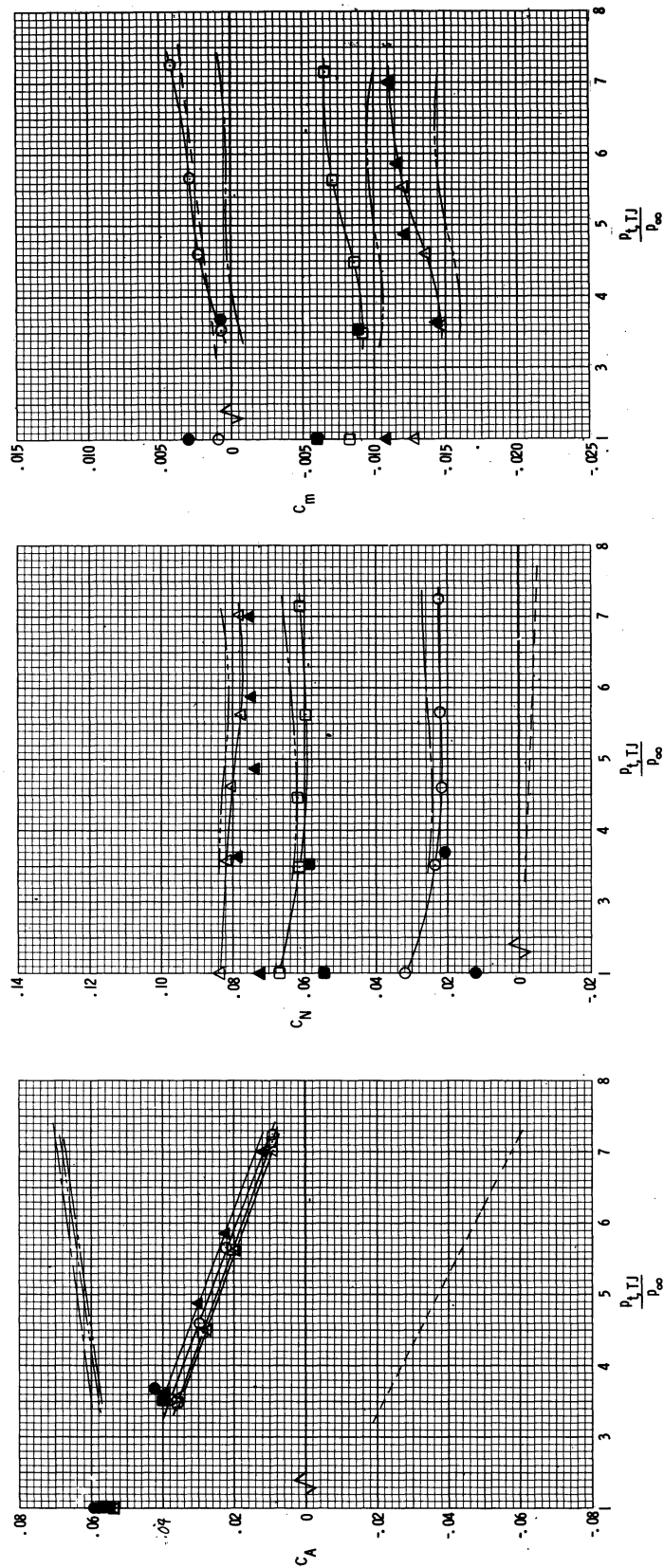


(e)  $M_{\infty} = 1.00$ .

Figure 29.- Continued.

$\alpha$ , deg	Data	$\bar{p}_{L,SJ}$ Data corrected for TJ thrust only	$C_{A,SJ}$	$C_{N,SJ}$	$C_{m,SJ}$
0	○	3.16	-.0053	.0006	.0004
2	□	2.39	-.0040	.0004	.0003
3	△	2.40	-.0040	.0004	.0003

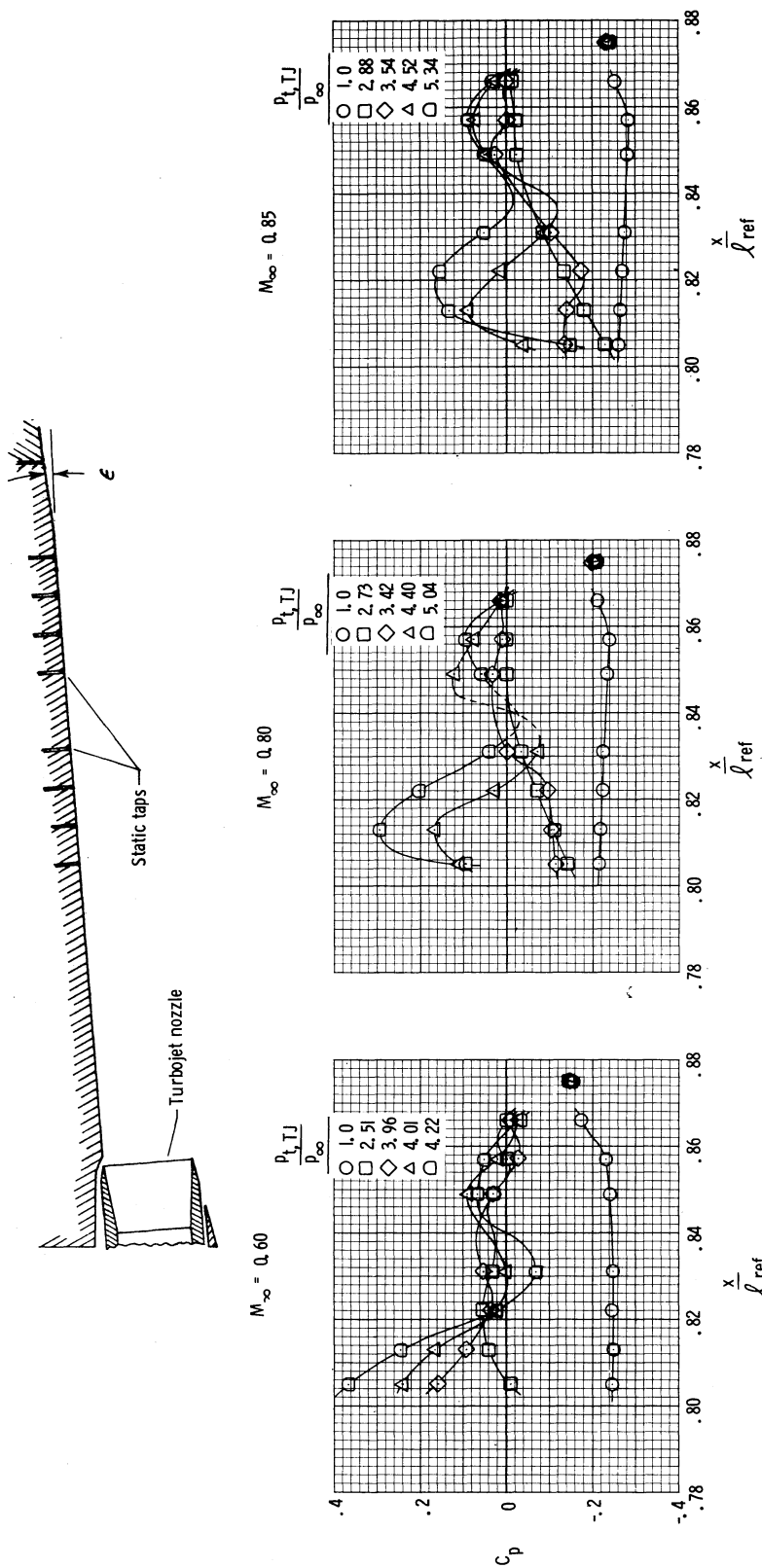
-----  $C_{A,TJ}$ ,  $C_{N,TJ}$  or  $C_{m,TJ}$   
 Solid symbol indicates no scramjet flow



(f)  $M_\infty = 1.20$ .

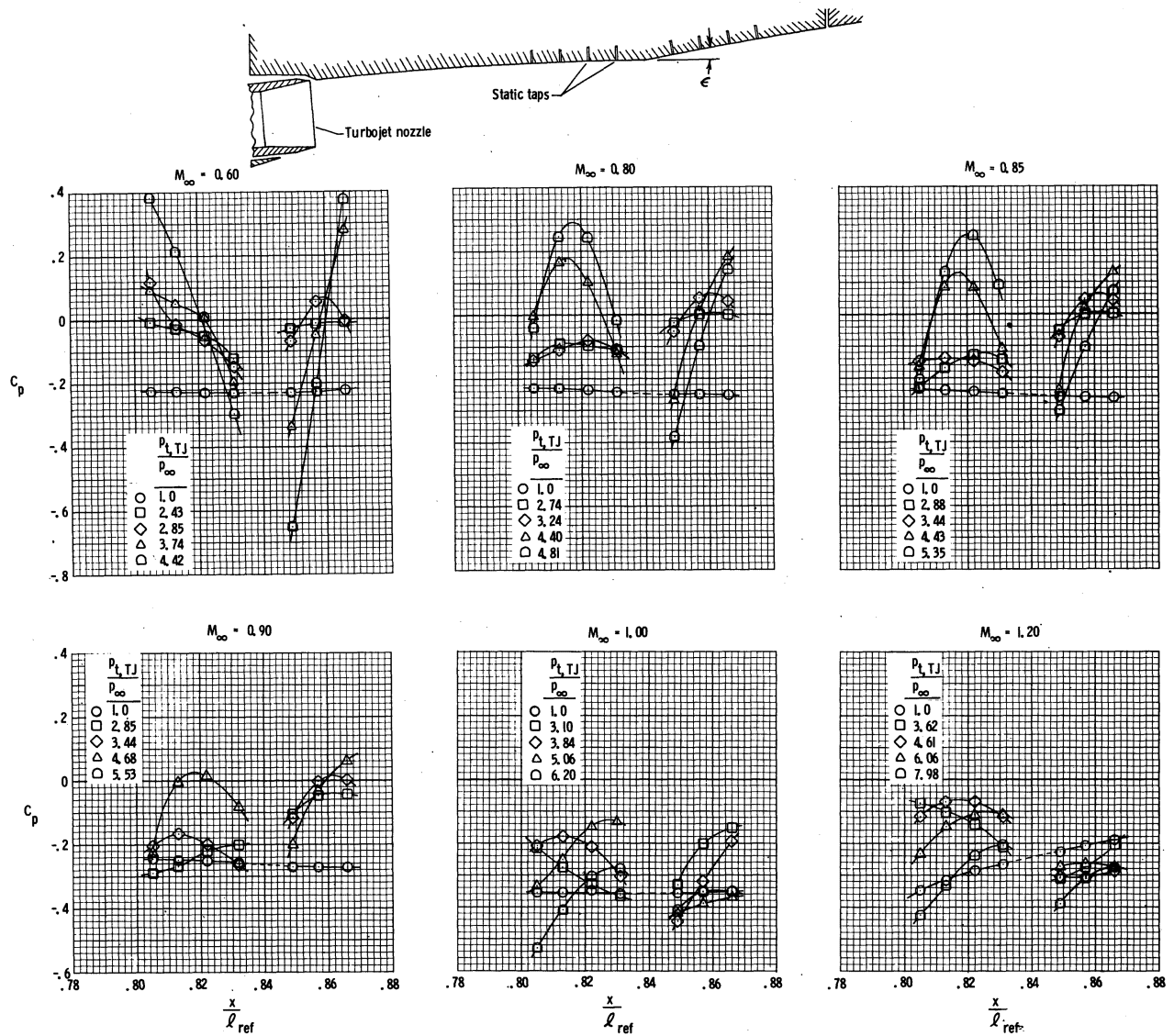
Figure 29.- Concluded.





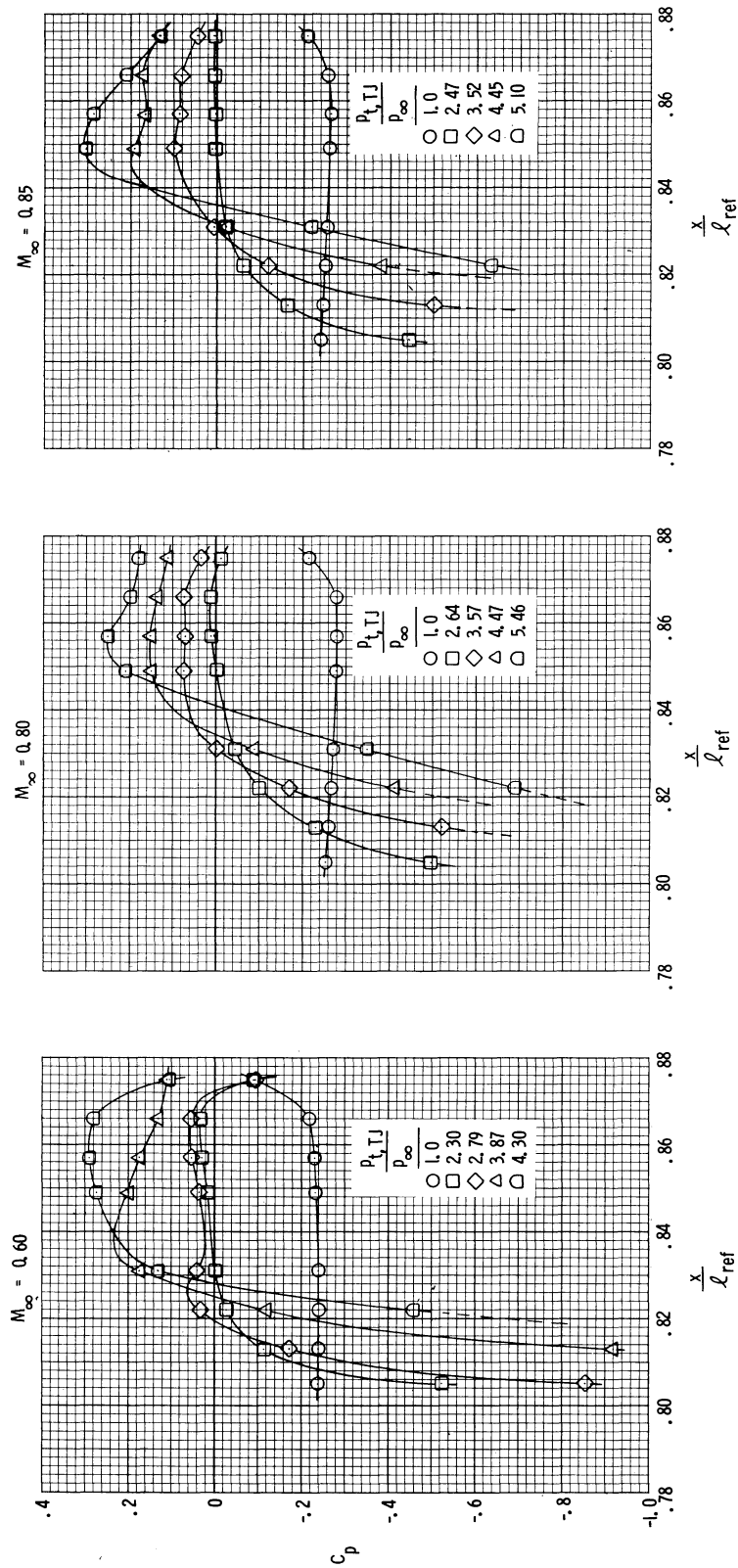
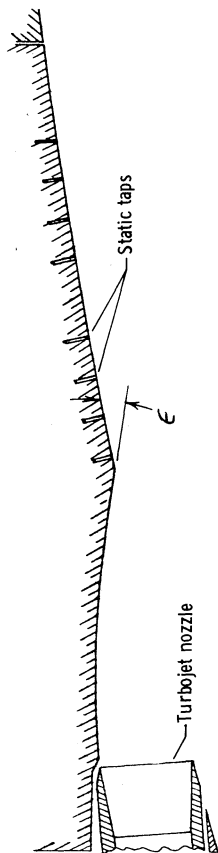
(a)  $\epsilon = 5^\circ$ .

Figure 30.- Pressure coefficient distributions along turbojet exhaust cutout in ramp.  
 $\alpha = 2^\circ$ ; with fences; flowthrough nacelle.



(b)  $\epsilon = 10^\circ$ .

Figure 30.- Continued.



(c)  $\epsilon = 20^\circ$ .

Figure 30.- Concluded.

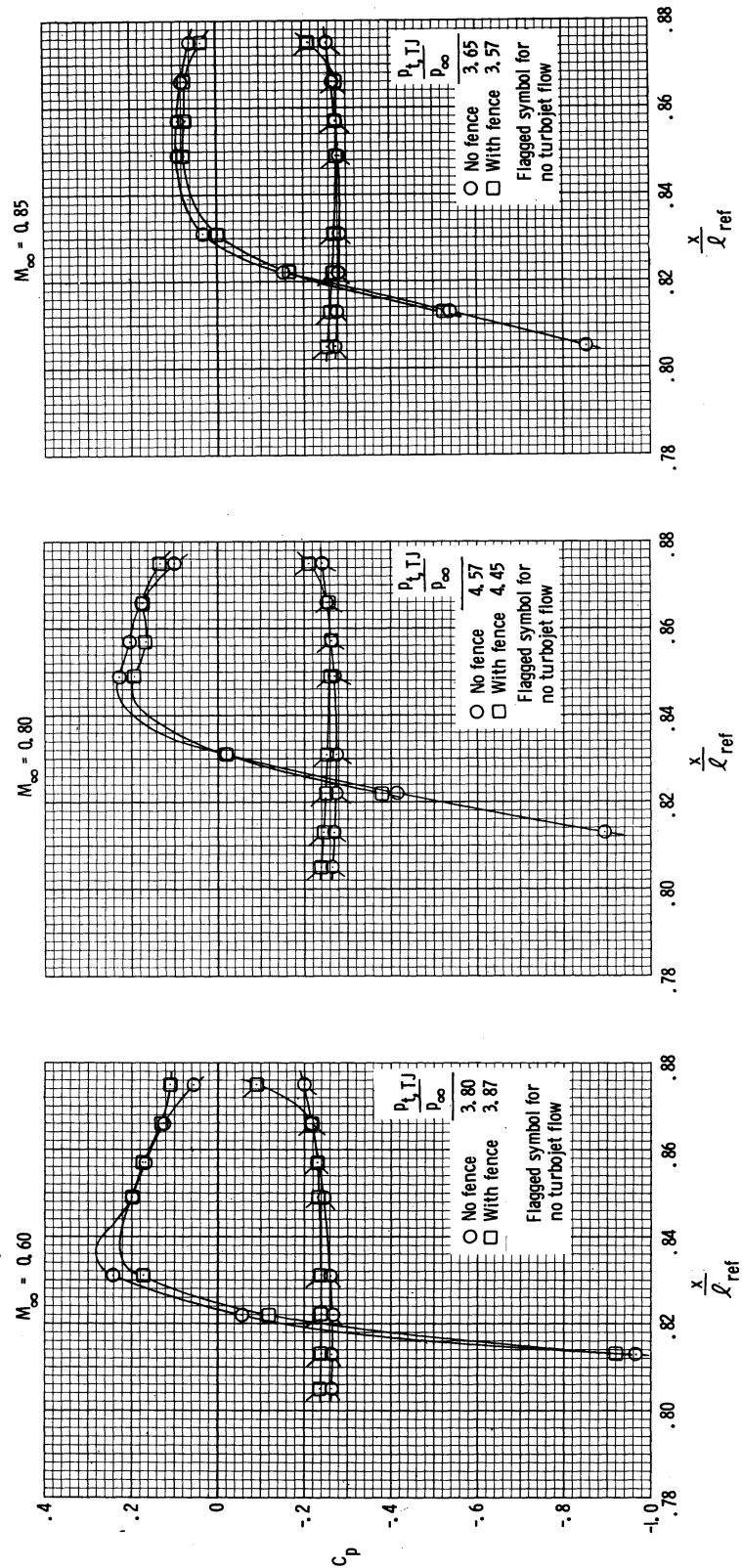
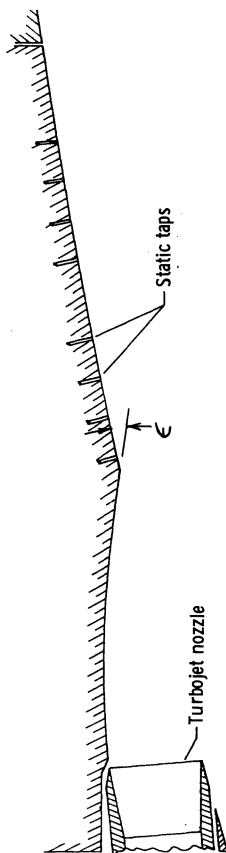


Figure 31.- Comparison of ramp pressure coefficient distributions with and without flow fences.  
 $\epsilon = 20^\circ$ ;  $\alpha = 2^\circ$ .